

University of Bath



**PHD**

**Boundary integral methods for acoustic scattering and radiation**

Pantazopoulou, Panagiota

*Award date:*  
2006

*Awarding institution:*  
University of Bath

[Link to publication](#)

**General rights**

Copyright and moral rights for the publications made accessible in the public portal are retained by the authors and/or other copyright owners and it is a condition of accessing publications that users recognise and abide by the legal requirements associated with these rights.

- Users may download and print one copy of any publication from the public portal for the purpose of private study or research.
- You may not further distribute the material or use it for any profit-making activity or commercial gain
- You may freely distribute the URL identifying the publication in the public portal ?

**Take down policy**

If you believe that this document breaches copyright please contact us providing details, and we will remove access to the work immediately and investigate your claim.

Download date: 13. May. 2019

# Boundary integral methods for acoustic scattering and radiation

Submitted by Panagiota Pantazopoulou  
for the degree of Ph.D.  
of the University of Bath  
2006


COPYRIGHT

*Mechanical Engineering*

**Attention is drawn to the fact that the copyright of this thesis rests with its author. This copy of the thesis has been supplied on condition that anyone who consults it is understood to recognise that the copyright rests with its author and that no quotation from the thesis and no information derived from it may be published without the prior written consent of the author.**

**This thesis may be made available for consultation within the University Library and may be photocopied or lent to other libraries for the purpose of consultation.**

Signed :



P PANTAZO

UMI Number: U220506

All rights reserved

INFORMATION TO ALL USERS

The quality of this reproduction is dependent upon the quality of the copy submitted.

In the unlikely event that the author did not send a complete manuscript and there are missing pages, these will be noted. Also, if material had to be removed, a note will indicate the deletion.



UMI U220506

Published by ProQuest LLC 2013. Copyright in the Dissertation held by the Author.  
Microform Edition © ProQuest LLC.

All rights reserved. This work is protected against  
unauthorized copying under Title 17, United States Code.



ProQuest LLC  
789 East Eisenhower Parkway  
P.O. Box 1346  
Ann Arbor, MI 48106-1346

UNIVERSITY OF BATH  
LIBRARY  
65 12 JUL 2007  
Ph.D. ....



# Abstract

A boundary integral equation based on a Morino approach is used to solve acoustic problems in two and three dimensions. This is a linearized equation which is valid for both compressible and incompressible potential flow. It includes the wake effect which appears in lifting bodies as an extra term in the integral formulation. The main concept of this work is the acoustic scattering in non-uniform potential flows. The approach used to simulate the unsteady character of the problem is to assume the velocity potential as the sum of a mean value and a small perturbation. Solving the integral equation once for the steady (aerodynamic) part and once for the unsteady (acoustic) part, and combining the resulting velocity potential and velocity in the Bernoulli equation, we can obtain the sound pressure. This procedure is actually a coupled aerodynamic/acoustic approach which has proven to be very promising and reliable for dealing with sound scattering and radiation problems in non uniform flows.

The test cases are an aerofoil and a wing with and without high lift devices in both compressible and incompressible flow with a unit acoustic source nearby. The results show the acoustic pressure contours around the lifting body for three different Mach numbers (low, medium and high) and for various frequencies. The aeroengine noise propagation problem is also investigated and a scarfing configuration is considered. A parallel implementation using the Message Passing Interface to speed-up the solution procedure allows us to apply the method to large scale problems and high frequencies.

The results showed that when placing the engines above the wing the shielding effect of the wing configuration is quite strong and noise reduces. Moreover, the flow has a noticeable role as it stretches the acoustic field towards its direction. The wake effect in both the two and three dimensional analysis showed a small effect on noise scattering at relatively high Mach numbers ( $M = 0.6$ ).

*To Barry ...*

# Acknowledgments

The current project was supported by a European Community Marie Curie Fellowship in the form of one year at Trinity College Dublin as part of the *European Doctorate in Sound and Vibration Studies* and by the *HPC-Europa* programme in the form of three months in CINECA, Bologna, Italy.

# Thanks to

- My supervisor, Michael Carley for being very helpful, honest and close to me throughout this journey.
- My supervisor in Trinity College Dublin, Prof. Henry Rice for his guidance and advice.
- Eleni for being on my side the past eight years especially in my hard times.
- Panagiotis for his patience and understanding.
- The “office”, Anna, Bernardo, Charbel, Dave, Eleni, Panagioti, Paul, Sam, and Zhijin Zhijin for their pleasant company inside and outside the office.
- Prof. Ismet Gursul for his help and support.
- My friends in Trinity College Dublin who showed me how to drink Guinness properly and how to be “grand” all the time.
- Eleni, Thanasi and Dimitri who apart from being my loving family they are the reason for whatever I have achieved.
- All those who are still standing me. . .

# Nomenclature

$A$	Amplitude coefficient
$A_{mn}$	Mode coefficient
$a$	Characteristic length
$B$	Number of blades
$B_m$	Amplitude coefficient
$b$	Wing span
$C$	Helmholtz equation coefficient
$C_p$	Pressure coefficient
$c$	Local speed of sound
$c_0$	Speed of sound at reference conditions
$e$	Thickness ratio of an elliptical section
$f$	Frequency
$G$	Green's function
$G_0$	Steady Green's function
$G_{2D}$	Two dimensional Green's function
$G_{3D}$	Three dimensional Green's function
$H(x)$	Heaviside step function
$H_i^{(m)}$	$i$ th order Hankel function of $m$ th kind
$h_n^{(m)}$	Spherical Hankel function of the $m$ th kind and $n$ th order
$i$	$\sqrt{-1}$
$J_m$	Bessel function of first kind of order $m$
$j_n$	Spherical Bessel function of the first kind, order $n$
$k$	$\omega/c$ , wave number
$L$	Shape function
$M$	Mach number
$m$	Mode number
$N$	Number of nodes
$n$	Normal vector
$n$	Harmonic number
$n_{elems}$	Number of elements of a square matrix, [A], in a linear system
$n_{rows}$	Number of rows of [A] allocated to each processor
$P$	Acoustic pressure amplitude, $p = Pe^{-i\omega t}$
$P_n$	Legendre polynomial of order $n$
$p$	Acoustic pressure from a rotor, number of processors used for parallelization

$p'$	Unsteady pressure
$q$	Acoustic source strength
$R$	Distance
$r$	Position on a duct radius
$r_{duct}$	Duct radius
$r_{rotor}$	Rotor radius
$S$	Surface
$S(p)$	Speed-up of a parallel program
$T_p$	The elapsed time for the program with $p$ processors
$t$	Time, non-dimensional duct radius
$U$	Velocity
$u$	Unsteady velocity
$\mathbf{u}$	Velocity
$\bar{v}$	Steady velocity normal to the wake
$V_B$	Velocity of any point on the surface
$\mathbf{v}'_n$	Unsteady velocity normal to the wake
$V_1$	Velocity on the upper point of the wake
$V_2$	Velocity on the lower point of the wake
$v$	Total velocity
$v'$	Unsteady total velocity
$\bar{v}$	Steady total velocity
$x$	$x$ coordinate in the Cartesian system
$\mathbf{x}$	Position vector
$y$	$y$ coordinate in the Cartesian system
$Y_m$	Bessel function of second kind of order $m$
$z$	$z$ coordinate in the Cartesian system
$\alpha$	Angle of attack
$\beta$	$\sqrt{1 - M^2}$
$\Gamma$	Two dimensional surface
$\Gamma_b$	Circulation around the body
$\gamma$	Ratio of specific heats
$\gamma_{TE}$	Vortex velocity at a trailing edge
$\delta$	Dirac delta function
$\epsilon$	Surface displacement, error
$\eta$	Nodal coordinate
$\eta(p)$	Efficiency of a parallel program
$\theta$	Time delay, $R/c$
$\lambda$	Wavelength
$\xi$	Nodal coordinate
$\rho$	Density
$\Sigma$	Non linear terms in the integral equation
$\sigma$	$\frac{M(x-x_1)+S}{\beta^2}$
$\tau$	Retarded time

$\phi$	Total velocity potential
$\phi_n$	Acoustic pressure phase
$\phi_w$	Velocity potential on the wake
$\phi'$	Unsteady velocity potential
$\bar{\phi}$	Steady velocity potential
$\Omega$	Angular velocity
$\omega$	Radian frequency

# Subscripts

<i>com</i>	Computational
<i>i</i>	Global element index
<i>j</i>	Local element index
<b>max</b>	Maximum
<i>n</i>	Radial mode number
<b>n</b>	Normal
<i>r</i>	Radial direction
<i>t</i>	Rotor tip
<i>thr</i>	Theoretical
<b>TE</b>	Trailing edge
<i>w</i>	Wake
<i>x</i>	Axial direction
<b>1</b>	Source position
<i>1x</i>	Upper point of the wake surface on the <i>x</i> direction
<i>1y</i>	Upper point of the wake surface on the <i>y</i> direction
<b>2D</b>	Two dimensional
<i>2x</i>	Lower point of the wake surface on the <i>x</i> direction
<i>2y</i>	Lower point of the wake surface on the <i>y</i> direction
<b>3D</b>	Three dimensional



# Superscripts

duct	Duct
<i>inc</i>	Incident
rotor	Rotor
<i>sct</i>	Scattered
<i>T</i>	Transpose
tot	Total

# Abbreviations

BIE	Boundary Integral Equation
CHIEF	Combined Helmholtz Integral Equation Formulation
FE	Finite Element
FEM	Finite Element Method
FD	Finite Difference
GTS	GNU Triangulated Surface library
HIE	Helmholtz Integral Equation
ICAO	International Civil Aviation Organization
MPI	Message Passing Interface

# Contents

<b>Contents</b>	<b>xii</b>
<b>List of Figures</b>	<b>xiv</b>
<b>List of Tables</b>	<b>xviii</b>
<b>1 Introduction</b>	<b>1</b>
1.1 Aircraft noise sources . . . . .	5
1.2 Present numerical approaches . . . . .	6
<b>2 Prediction of noise from aircraft</b>	<b>8</b>
2.1 Aeroacoustics as unsteady aerodynamics . . . . .	8
2.2 Potential aerodynamics . . . . .	9
2.3 Trailing edge conditions . . . . .	11
2.4 Numerical issues . . . . .	13
2.5 Duct acoustics . . . . .	15
2.6 Scattering and radiation . . . . .	16
<b>3 Boundary integral method</b>	<b>20</b>
3.1 Helmholtz equation for quiescent fluid . . . . .	20
3.2 Boundary integral method for unsteady flow . . . . .	23
3.3 Boundary integral method for two dimensional problems . . . . .	27
3.4 Wake boundary conditions . . . . .	29
3.5 Duct sound propagation theory . . . . .	32
3.6 Integral representation of the incident field . . . . .	35
<b>4 Numerical implementation</b>	<b>36</b>
4.1 Surface discretisation in three dimensions . . . . .	37
4.2 Boundary discretisation in two dimensions . . . . .	38
4.3 Integration . . . . .	39
4.4 Singularities . . . . .	40
4.5 Sharp edges . . . . .	40
4.6 Validation examples . . . . .	41
4.7 Aerodynamic validation . . . . .	46

<b>5</b>	<b>Parallelisation</b>	<b>56</b>
5.1	Performance analysis . . . . .	58
5.2	Parallel calculations . . . . .	59
<b>6</b>	<b>Results</b>	<b>62</b>
6.1	Sound field around a duct . . . . .	62
6.2	Radiation field around a wing . . . . .	65
6.3	Radiation field around an aerofoil . . . . .	70
<b>7</b>	<b>Conclusions</b>	<b>75</b>
	<b>Bibliography</b>	<b>77</b>
<b>A</b>	<b>Appendix</b>	<b>83</b>
A.1	Three dimensional results for wings . . . . .	83
A.2	Two dimensional results . . . . .	94

# List of Figures

1.1	Noise levels at take off for commercial jets. . . . .	3
1.2	Noise sources on an aircraft [1]. . . . .	3
1.3	Scarfed engine configuration. . . . .	4
1.4	Future aircraft configuration [1]. . . . .	4
2.1	Trailing edge configuration. . . . .	12
2.2	Midpoints of the trailing edge side elements. . . . .	12
2.3	Points on each side of the wake geometry . . . . .	13
3.1	Body in an infinite acoustic medium. . . . .	21
3.2	Body in mean flow with an acoustic source nearby. . . . .	24
3.3	Wing and wake geometry in mean flow. . . . .	25
3.4	Aerofoil and wake geometry in mean flow. . . . .	28
3.5	Sound reflection and transmission by a moving medium. . . . .	29
3.6	Points on each side of the wake geometry. . . . .	31
3.7	Difference in acoustic displacement across the wake, $ka = 1.6$ . . . . .	32
3.8	Geometry of a cylindrical duct. . . . .	34
4.1	Three dimensional discretisation of a wing. . . . .	37
4.2	A triangular element and the corresponding isoparametric element. . . . .	37
4.3	Boundary discretisation. . . . .	38
4.4	Quadratic element. . . . .	39
4.5	An element of the body grid. . . . .	39
4.6	The normal vectors at the trailing edge . . . . .	41
4.7	Double normal vectors at a sharp edge [2]. . . . .	41
4.8	Velocity potential around a sphere in flow with $M = 0.1$ , $a: ka = 1$ ; $b:$ $ka = 10$ . Solid line indicates analytical solution and dashed line indicates computed solution. . . . .	42
4.9	Error vs $ka$ for $N = 1080$ , $N = 2520$ and $N = 4560$ for $M = 0.6$ . . . . .	43
4.10	Plane wave on a sphere. . . . .	43
4.11	Scattered pressure field (real part), $ka = 10$ , $a: R/a = 2$ ; $b: R/a = 8$ . Solid line indicates analytical solution and dot line indicates computed solution. . .	44
4.12	Error in scattered pressure from a plane wave on a sphere for $N = 1080$ , $N = 2520$ and $N = 4560$ . . . . .	44

4.13 Pulsating sphere. . . . .	45
4.14 Velocity potential error ( $\epsilon$ ) vs $ka$ for a pulsating sphere for $N = 1080$ , $N = 2520$ and $N = 4560$ . $a$ : $M = 0.1$ ; $b$ : $M = 0.3$ . . . . .	45
4.15 Plan view of semispan wing indicating pressure tap stations in inches [3]. . . . .	46
4.16 Pressure coefficient at $M = 0.3$ and $\alpha = 0^\circ$ . Solid line indicates computed and star symbols experimental results respectively. . . . .	47
4.17 Pressure coefficient at $M = 0.3$ and $\alpha = 6^\circ$ . Solid line indicates computed and star symbols experimental results respectively. . . . .	48
4.18 Pressure coefficient at $M = 0.3$ and $\alpha = 10^\circ$ . Solid line indicates computed and star symbols experimental results respectively. . . . .	49
4.19 Pressure coefficient at $M = 0.3$ and $\alpha = 16^\circ$ . Solid line indicates computed and star symbols experimental results respectively. . . . .	50
4.20 Pressure coefficient at $M = 0.3$ and $\alpha = 0^\circ$ with flap extended. Solid line indicates computed and star symbols experimental results respectively. . . . .	51
4.21 Pressure coefficient at $M = 0.3$ and $\alpha = 8^\circ$ with flap extended. Solid line indicates computed and star symbols experimental results respectively. . . . .	52
4.22 Unsteady pressure around a circle with a unit acoustic source; computed values shown solid, analytical values dashed. . . . .	53
4.23 Error in unsteady pressure around a circle for $N = 200$ , $N = 300$ and $N = 400$ . . . . .	53
4.24 Geometrical characteristics of an elliptical section. . . . .	54
4.25 Error behaviour with Mach number for the maximum velocity over an elliptical section. . . . .	54
4.26 Thickness vs Mach number for a given error in the maximum velocity over an elliptical section; dashed line indicates error 0.01; dotted line, 0.1 and solid line, 0.05. . . . .	55
4.27 Error behaviour with Mach number for $N = 100$ , $N = 200$ , $N = 300$ and $N = 400$ . . . . .	55
5.1 Distributed memory model. . . . .	56
5.2 Shared memory model. . . . .	57
5.3 Balancing and overhead in a parallel program [4]. . . . .	58
5.4 Performance graphs for a sphere with an acoustic source of: $M = 0.1$ , $ka = 1$ , $N = 4560$ : $a$ : speed up; $b$ : efficiency. . . . .	60
5.5 Performance graphs for a duct with an acoustic source of $ka = 1$ , $N = 8200$ nearby, $a$ : speed up; $b$ : efficiency. . . . .	60
5.6 Performance graphs for a wing with an acoustic source of $M = 0.1$ , $ka = 1$ , $N = 11016$ nearby, $a$ : speed up; $b$ : efficiency. . . . .	60
6.1 Duct and scarfed duct geometry. . . . .	62
6.2 Elliptical section of the duct generator. . . . .	63
6.3 Color contour pressure plots around the duct, $a$ : scarfing angle = $0$ ; $b$ : scarfing angle = $\pi/18$ ; $c$ : scarfing angle = $\pi/12$ ; $d$ : scarfing angle = $\pi/6$ . . . . .	64
6.4 Ducted fan noise directivities, $M_t = 0.95$ , $a$ : scarfing angle = $0$ ; $b$ : scarfing angle = $\pi/18$ ; $c$ : scarfing angle = $\pi/12$ ; $d$ : scarfing angle = $\pi/9$ . . . . .	66

6.5	Ducted fan noise directivities, $M_t = 1.1$ , $a$ : scarfing angle = 0 ; $b$ : scarfing angle = $\pi/18$ ; $c$ : scarfing angle = $\pi/12$ ; $d$ : scarfing angle = $\pi/9$ . . . . .	67
6.6	Ducted fan noise directivities, $M_t = 0.9$ , $a$ : scarfing angle = 0 ; $b$ : scarfing angle = $\pi/18$ ; $c$ : scarfing angle = $\pi/12$ ; $d$ : scarfing angle = $\pi/9$ . . . . .	68
6.7	The wing and the positions of the result planes. . . . .	70
6.8	Total acoustic pressure (real part) around a wing with high lift devices and a unit acoustic source; contour levels $\pm 10^{-1}$ , $\pm 10^{-2}$ , $\pm 10^{-3}$ ; positive values shown solid, negative values dashed. . . . .	71
6.9	Total acoustic pressure (real part) around a NACA2412 and a unit acoustic source; contour levels $\pm 10^{-1}$ , $\pm 10^{-2}$ , $\pm 10^{-3}$ ; positive values shown solid, negative values dashed. . . . .	72
6.10	Aerofoil geometry with the high lift devices extended. . . . .	73
6.11	Total acoustic pressure (real part) around the aerofoil with high lift devices and a unit acoustic source; contour levels $\pm 10^{-1}$ , $\pm 10^{-2}$ , $\pm 10^{-3}$ ; positive values shown solid, negative values dashed. . . . .	74
A.1	Total acoustic pressure (real part) around a NACA 2412 wing; positive values shown solid, negative values dashed. $M = 0.3, 0.6$ ; $ka = 65$ ; $z/b = 0.1, 0.25, 0.5$ . . . . .	84
A.2	Total acoustic pressure (real part) around a NACA 2412 wing; positive values shown solid, negative values dashed. $M = 0.6$ ; $ka = 30, 65$ ; $z/b = 0.1, 0.25, 0.5$ ; $\alpha = 10^\circ$ . . . . .	85
A.3	Total acoustic pressure (real part) around a NACA 2412 wing; positive values shown solid, negative values dashed. $M = 0.3$ ; $ka = 30, 65$ ; $z/b = 0.1, 0.25, 0.5$ ; $\alpha = 10^\circ$ . . . . .	86
A.4	Total acoustic pressure (real part) around a NACA 2412 wing; positive values shown solid, negative values dashed. $M = 0.1$ ; $ka = 30, 65$ ; $z/b = 0.1, 0.25, 0.5$ ; $\alpha = 10^\circ$ . . . . .	87
A.5	Total acoustic pressure (real part) around a NACA 2412 wing; positive values shown solid, negative values dashed. $M = 0.6$ ; $ka = 30, 65$ ; $z/b = 0.1, 0.25, 0.5$ . . . . .	88
A.6	Total acoustic pressure (real part) around a NACA 2412 wing; positive values shown solid, negative values dashed. $M = 0.3$ ; $ka = 30, 65$ ; $z/b = 0.1, 0.25, 0.5$ . . . . .	89
A.7	Total acoustic pressure (real part) around a NACA 2412 wing; positive values shown solid, negative values dashed. $M = 0.1$ ; $ka = 30, 65$ ; $z/b = 0.1, 0.25, 0.5$ . . . . .	90
A.8	Total acoustic pressure (real part) around a NACA 2412 wing; positive values shown solid, negative values dashed. $M = 0.6$ ; $ka = 30, 65$ ; $z/b = 0.1, 0.25, 0.5$ ; $\alpha = 10^\circ$ . . . . .	91
A.9	Total acoustic pressure (real part) around a NACA 2412 wing; positive values shown solid, negative values dashed. $M = 0.3$ ; $ka = 30, 65$ ; $z/b = 0.1, 0.25, 0.5$ ; $\alpha = 10^\circ$ . . . . .	92

A.10 Total acoustic pressure (real part) around a NACA 2412 wing; positive values shown solid, negative values dashed.  $M = 0.1$ ;  $ka = 30, 65$ ;  $z/b = 0.1, 0.25, 0.5$ ;  $\alpha = 10^\circ$ . . . . . 93

A.11 Total acoustic pressure (real part) around the aerofoil; positive values shown solid, negative values dashed.  $M = 0.1, 0.3, 0.6$ ;  $ka = 1.6, 3.2$ . . . . . 95

A.12 Total acoustic pressure (real part) around the aerofoil with high lift devices; positive values shown solid, negative values dashed.  $M = 0.1, 0.3, 0.6$ ;  $ka = 1.6, 3.2$ . . . . . 96

A.13 Total acoustic pressure (real part) around the aerofoil with high lift devices; positive values shown solid, negative values dashed.  $M = 0.1, 0.3, 0.6$ ;  $ka = 60, 72$ . . . . . 97

A.14 Total acoustic pressure (real part) around the aerofoil with high lift devices; positive values shown solid, negative values dashed.  $M = 0.1, 0.3, 0.6$ ;  $ka = 60, 72$ ;  $\alpha = 10^\circ$ . . . . . 98



# List of Tables

1.1 Forecast noise exposure in thousands of people in the UK. . . . .	2
---	---

# Chapter 1

## Introduction

The problem of noise control in aviation, which arose in the middle of the twentieth century with the beginning of the intense operation of jet airliners, is becoming more and more bothersome for the people who live close to airports. In recent years, the growing need for air transport has set new standards for noise control. On the one hand, passenger aeroplanes designed in the last few years are less noisy than those designed in the early stages of passenger aviation. On the other hand, because of the increasing use of aviation, environmental conditions near airports cannot be noticeably improved, and may even become worse in the next ten years, if considerable progress is not made in the development of technologies for aviation noise control. Because of the importance and the seriousness of the situation, the problem of reducing the level of aviation noise is one of the main aviation-related environmental problems and is of primary concern to international environmental and aviation organisations.

Intense operation of jet airliners the past thirty years is giving rise to increasing community concern. Because of the increase in the overall amount of aircraft operations, environmental conditions near airports are becoming more and more uncomfortable for residents. The British government has forecast [5] that aviation is likely to grow over the next thirty years at an average rate of 4.25% per year. These forecasts are based on the fact that the airport capacity will meet all demand. To meet the maximum demand for flights, additional airport capacity would be required which means that more runways and airports are due to be built. Aircraft landing and taking off are the leading sources of aviation noise. In particular, landing noise is increasing in importance and has become the dominant reason for complaints near airports. At the same time, the take off phase is equally annoying to the airport neighbours as high frequency operating conditions of engines during take off produce distracting noise levels. Aircraft noise has already the potential to affect the quality of life of at least half a million people in the UK [5], with 80% of these living close to major airports in the southeast of England. Table 1.1 shows the extent of noise pollution around the five major airports in the UK under the Department for Transport's (DfT) growth forecasts.

Aircraft noise can affect concentration or sleep and can result in feelings of anger, frustration and irritation. People usually feel very annoyed when aircraft land or take off. Because the noise levels are quite high, they can interfere with everyday activities. People

Year	2000	2030
Heathrow	310	330
Manchester	40	80
Birmingham	30	180
Gatwick	8	30
Stansted	5	25

Table 1.1: Forecast noise exposure in thousands of people in the UK.

find it very irritating when they get distracted trying to do something that requires concentration or even when they have a conversation which is disrupted due to aircraft noise. Incidents like these can lead to people feeling stressed and angry. The situation is worse when noise affects sleep patterns. Sleep disturbance problems are often reported when people complain that they wake up early in the morning or they have difficulty falling asleep. Aircraft noise is a primary concern of environmental and aviation organisations and ICAO (International Civil Aviation Organisation) sets tighter certification standards known as Chapters for noise emissions from civil aircraft [6]. The standards for community noise are set depending on the maximum take off mass of an aeroplane and are specified for three fixed reference points near the runway. These points characterise the main stages of the flight: take off, climb and descent. In 2001, ICAO issued a new standard for aircraft noise, which came into effect on January 1, 2006 and imposes stricter requirements on community noise. According to this standard, the noise levels from a new aeroplane must be 10 dB lower than previously allowable noise levels. In addition, the decrease in noise level at any two points of measurement should be no less than 2 dB. The ICAO resolution can be summarised in four elements: reduction of noise at source, land use planning and management around airports, operating procedure and operating restrictions.

Over the past thirty years improvements in aircraft technology have resulted in substantial reductions in the noise of individual aircraft. Figure 1.1 illustrates aircraft noise levels over the past fifty years [7]. The first generation Boeing 707 created noise at take off similar to that of Concorde. An average reduction of 25 dB has been achieved over the past thirty years. Engine noise during take off and landing gear noise during landing are the most important sources of aircraft noise. Figure 1.2 shows the noise sources on an aircraft during operation. To manage the situation, airports impose restrictions on noisier aircraft and additionally they control night noise by not allowing take off at specific times during the night. Apart from the above operational procedures and limitations, much interest is shown in possible future aircraft configurations and airframe alterations. Engine noise is dominant during take off and is composed mainly of fan and jet noise. High frequency fan noise can be reduced by improving absorption inside the nacelle using appropriate structural materials and a honeycomb type layer. Moreover, lengthening the inlet of the engine and making it slightly scarfed can achieve lower noise levels. Figure 1.3 shows the scarfing configuration of an aeroengine.

Jet noise levels can be lowered by increasing the engine by-pass ratio and thus re-

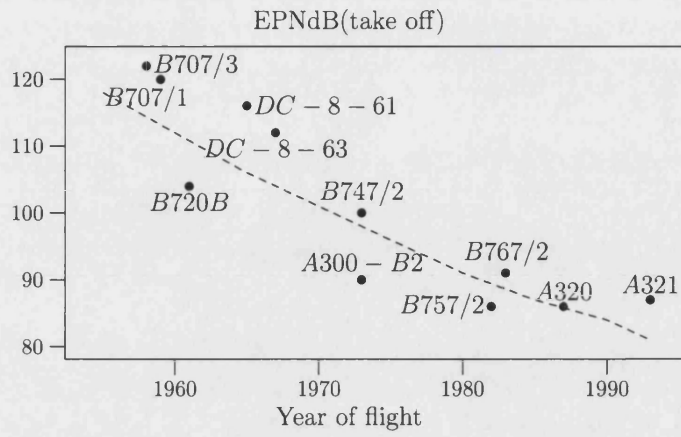


Figure 1.1: Noise levels at take off for commercial jets.

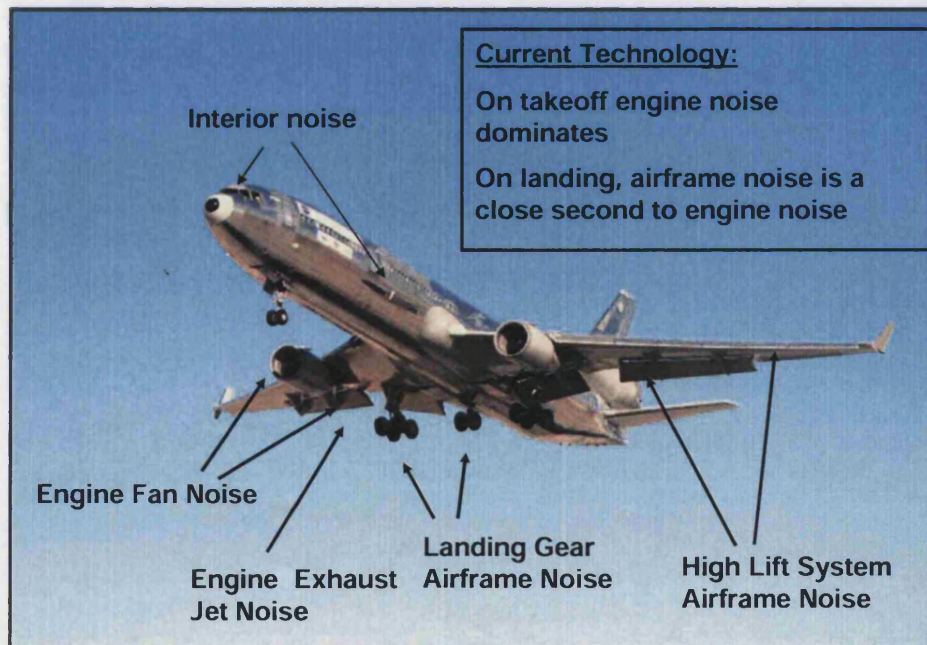


Figure 1.2: Noise sources on an aircraft [1].



Figure 1.3: Scarfed engine configuration.

ducing the jet velocity [8]. Additional noise is generated by extended landing gear, open cavities and wheel wells. Modern aircraft already cover their wheel wells while the gear is extended but further improvements should be made. The length of the main landing gear can be reduced by attaching it to the fuselage. Another source of noise is the take off and landing configuration of conventional aircraft. Minimising the number of high lift devices needed for the above two phases can result in noise reduction. The slots that appear at such a configuration produce noise and can be avoided if a different configuration is adopted where fewer gaps are present. A shielding effect can be achieved by placing the engines above the wing and further backwards. Such a configuration is shown on Figure 1.4.



Figure 1.4: Future aircraft configuration [1].

A lot of research is carried out on aircraft noise source prediction and reduction. This research is mainly focused on modelling and design and on the development of efficient methods of noise prediction. A combination of different aircraft configurations and modifications can lead to more environmentally friendly aircraft. This becomes essential if we think that aviation needs and aircraft operations are rising at a fast rate.

## 1.1 Aircraft noise sources

It becomes clear from the above facts that restrictions and regulations for aviation noise control are becoming stricter and stricter. Therefore, the solution of the complex scientific and engineering problems related to the improvement of the acoustic characteristics of passenger aeroplanes is the major task of today's aviation acoustics. This now has the potential to reshape design drivers for the next generation of aircraft. To this end the study of full body shielding and scattering effects induced by novel engine placement is a critical issue. The sources of aircraft noise most responsible for community and ground crew effects are high-velocity jet exhausts, fans, internal turbomachinery, propellers, rotors, and, for supersonic aircraft, sonic booms. The sources most responsible for passenger or flight crew effects are turbulent boundary layers, propellers, helicopter gear boxes, jet exhausts, internal combustion engine exhausts and structure borne vibration from unbalanced rotational forces. To effectively control noise, that is, to reduce those components that are most responsible for adverse human effects, it is necessary to thoroughly understand the physical characteristics of the sound and how each of those characteristics can affect human response.

It is worth referring to a few basic things for each of the above sources in order to obtain a general perception of how these contribute to noise generation. Therefore, the four dominant types of aircraft noise according to Hubbard [8] are: propeller and propfan noise, rotor noise, turbomachinery noise and jet noise.

Rotorcraft noise is generally characterised by loud, sharp, periodic sounds which are labelled impulsive noise. During a normal rotor-blade revolution in high-speed nonaxial flight, transonic flow on the rotor advancing blade can cause large drag, vibration and noise effects. The most important source of this type of noise is Blade-Vortex Interaction (BVI) noise which is produced when the blade cuts the vortex. To overcome these high-speed-flight limitations, new types of rotorcraft are being developed that have nearly the hovering efficiency of the helicopter. However, all the above difficulties have led to more practical solutions. In particular, the tips of most rotor blades are now thinned, tapered and swept. Thinning and tapering the tip of the rotor directly reduces thickness noise. Finally, sweeping the blade tip, as in wing sweep on supersonic aeroplanes, tends to lower the effective tip Mach number.

Jet noise is associated with the turbulence created by the jet mixing with the surrounding air. Unless the properties of the unsteady flow are known, the details of the source field cannot be determined. However, we have to mention that several problems arise when trying to model jet noise. The basic reasons that make things harder and more complicated are supersonic, subsonic flow and turbulent phenomena which are developed in the jet. The structure of a turbulent jet is described by an initial mixing (laminar-turbulent) region which is followed by a fully developed turbulent region. Certainly, transition from laminar to turbulent flow is a strong source of noise in a mixing region. Jet noise as a study in aerodynamic noise had its foundations in the work of Lighthill [9] on sound generated aerodynamically. Lighthill's theory of aerodynamic noise is based on the exact equations of fluid flow and we refer to it as *Lighthill's acoustic analogy*. Jet noise reduction can be achieved by shaping the nozzle exit with a relatively small loss in nozzle performance.

This led to the corrugated nozzle. Although the noise reduction obtained with the corrugated nozzle may be considered modest, it is nevertheless accepted as the one major practical device that has reduced jet noise for minimum performance loss. Generally, several attempts have been made to reduce jet noise without paying the penalty of loss of nozzle efficiency. However, the main feature of all noise reduction schemes is shown to be large changes in the jet flow structure.

Turbomachinery noise is associated with civil aviation and includes fans, compressors and turbines. The primary concern for turbomachinery noise is community exposure during take off and approach operations. The two operating points of interest for community noise, approach and take off, correspond to subsonic and supersonic tip Mach numbers. More specifically, as acoustic modes are generated because of the blade motion they propagate upstream and downstream in the engine ducts, they interact with other modes which both reflect and scatter the acoustic energy. Duct radiation in the far-field is another process which is quite important as its analysis gives the far-field directivity patterns which are related to ground noise pollution.

For the fan of a turbofan engine, noise reduction can be achieved by designing fan duct acoustic treatment to absorb the noise produced by the source. It should be mentioned that the amount of noise suppression achieved with duct acoustic treatment is predominantly a function of the fan design characteristics. In particular, the fan tip speed and blade numbers have an influence on the achievable suppression. Thus, one can design the fan acoustically to give the maximum possible noise suppression.

## 1.2 Present numerical approaches

The contribution of this thesis to noise source generation and control is focused on the development of a technique that predicts the noise field when sound sources are specified. The technique is valid for both external and internal problems and is based on Boundary Integral Methods. Acoustic scattering and radiation problems in the absence of flow have been studied in depth for many years. Boundary integral equation (BIE) methods based on the Helmholtz integral equation (HIE) method only require discretisation of the surface boundary which can reduce some aspects of the computational effort required to perform these calculations on problems of engineering scale, compared to finite difference (FD) or finite element (FE) methods.

Boundary integral methods based on the Helmholtz integral equation for the analysis of exterior acoustic radiation and scattering problems have been developed extensively over the past few decades.

The major drawback of most of the current existing computational methods is that they only apply to uniform mean flow of low Mach number and that even the analytical solutions become invalid at high Mach numbers where the flow is compressible. But the need to solve more difficult problems more efficiently led to other methods that couple aerodynamics and aeroacoustics. Gennaretti et al. [10] successfully introduced a unified boundary integral equation making it feasible to obtain the acoustic pressure using the same formulation for both steady and unsteady velocity potential. The important feature



in their work is that they take into consideration the wake when examining lifting bodies. The integral equation is modified so as to include the wake contribution as an additional linear term. In the present thesis this approach is followed to predict the acoustic pressure field. Specifically, a scattering problem is presented in both compressible and incompressible potential flow. The test cases are an aerofoil and an aerofoil with flaps and slats in non-uniform flow with an acoustic source nearby. Considering the sound as a small perturbation, each flow property (velocity potential, velocity and pressure) is the sum of a fluctuation and a mean value. Therefore, the total velocity potential is assumed to be the sum of an unsteady part which results from the acoustic source and a steady part which comes from the potential flow. The two terms of the total velocity potential are obtained by applying the boundary element method to both steady and unsteady cases. Once the velocity potential is evaluated, Bernoulli's theorem is used to derive the acoustic pressure.



# Chapter 2

## Prediction of noise from aircraft

The role of the present work in the investigation of the aircraft noise problem is focused on the prediction of the acoustic pressure radiated around moving or stationary solid boundaries in non-uniform flow velocity. The acoustic source pressure is specified and the next step is to investigate the scattering behaviour of the sound when interacting with solid boundaries. The work includes the mathematical development and the computational implementation of an integral equation primarily used for aerodynamic purposes.

### 2.1 Aeroacoustics as unsteady aerodynamics

The main interest of the present work is focused on how sound is radiated in a fluid flow and how it is scattered when it interacts with solid boundaries. Moreover aerodynamics is closely related to aeroacoustics as from a computational point of view we could say that aerodynamics is the input of the aeroacoustics code [11] as it provides us with all the necessary flow information. Gennaretti, Luceri and Morino established a relationship between aeroacoustics and aerodynamics [12]. They introduced a unified approach which combines aerodynamic and aeroacoustic principles applying a Boundary Integral Equation (BIE) for unsteady flow to evaluate the acoustic pressure. Maybe the most important feature of this formulation is the contribution of the wake which is considered in such a way that it actually changes or affects the velocity potential distribution on the lifting body as it is included in the BIE. It is actually an extension of Morino's original work on Boundary Integral Methods [12] in aerodynamics for steady and unsteady flows. The integral formulation is valid in both the frequency and time domains. The wake geometry can have a prescribed shape or it can follow a free wake analysis according to which it takes its form as time elapses. Additionally compressibility effects are also included and the flexibility of including rotational or relative motion between parts of the investigated body is considered. A similar investigation on scattering from bodies moving in arbitrary motion comes from Farrasat and Myers [13] where the Kirchhoff [14] formulation is applied to develop a BIE. Their work starts with the extension of Kirchhoff's formula to moving surfaces and then the application of this theoretical study to aeroacoustics problems [15]. They present the mathematical procedure for the application of Kirchhoff's

formula to moving bodies and derive a useful expression for the velocity potential on the surface and in the field. Finite elements are used in conjunction with the Galerkin method in order to solve the integral equation when the observer is placed on the moving body surface as in Morino's case. A very basic point that they are pointing out is that the integral equation is valid only when  $M_n \ll 1$ , where  $M_n$  is the normal Mach number on the surface. Otherwise this formulation does not represent the physical problem of acoustic scattering from that body [15]. This has its origin in the non-linear aerodynamic effects that must be taken into account along with acoustic perturbations. This states that there is a limitation on the thickness ratio of the moving body in the sense that the more slender it becomes the more accurate the technique. A similar point was made by Morino [16] for the non-linear phenomena that occur in the transonic region and should be taken into account during the unsteady calculations.

An effective but computationally more expensive method for acoustic radiation in non-uniform flows is that of Zhang et al. [17]. It is a boundary element based method in which the integral equation is the same as Morino's with the difference that it does not include the wake term. It is actually a coupled FEM/BEM valid for axisymmetric bodies. The uniform flow region is treated using BEM and the non-uniform with FEM. Because in scattering problems the domain is unbounded and also because we are mostly interested in the far field the FEM costs more computational time as the far field needs to be discretized in order to calculate the properties on even on point in the far field. The BEM is an extension of their previous work [18] for acoustic radiation in uniform subsonic flow.

There are analytical expressions for scattering problems in uniform flows for simple geometries. Taylor [19] first introduced a transformed differential equation for steady state acoustic propagation in uniform flow. The two conditions that he imposed were that there is no flow through the surface and that the flow tends to a uniform stream at infinity. The theoretical investigation was applied to the problem of acoustic generation by vibrating spheres. Analytical formulae for a juddering and a pulsating sphere in very low Mach number ( $M < 0.3$ ) were given. The transformed wave equation was then converted to a boundary integral equation, the well known Helmholtz equation, used by Astley and Bain [20]. The problem was then reduced to an equivalent no-flow scattering problem with modified boundary conditions. The results of this boundary integral technique were checked against the theoretical expressions. Wu and Lee [18] went a step further and instead of solving the problem in a transformed domain i.e. Helmholtz equation, they directly derived the BIE which gives the velocity potential explicitly.

## 2.2 Potential aerodynamics

The calculation of potential flow around bodies and especially lifting bodies has been the subject of research since 1925. Later studies focused on conformal mapping [21], on the distribution of potential singularities such as vortices/sinks and doublets within the surface [22] and on thin aerofoil theory [23], all of them implemented using panel methods. A very constructive work on panel methods came from Hess and Smith [22] for bodies

in arbitrary motion. Their method was a breakthrough as it guided many researchers in the later years. They presented a boundary integral representation of the potential field in terms of source a distribution over the surface. In this approach they assume that the velocity is the sum of a mean value and a perturbation and set Neumann boundary conditions, i.e. no penetration.

Hess [24] a few years later, reviewed the surface source distribution technique using higher order elements to achieve more accurate results. The important feature in this work is that the trailing edge configuration effect is examined and its mathematical nature is illustrated. Because the trailing edge is a point on a corner (one point has two normal vectors) it causes mathematical singularities which are hard to eliminate. It is also difficult to draw physical conclusions on what happens at the trailing edge and what conditions should be imposed in order to represent reality. The trailing edge condition that was applied in this work was that the values of the velocity at the control points (element midpoints in that case) of the two elements adjacent to the trailing edge should be equal. Lifting bodies and especially aerofoils were the main interest of the investigation and so most studies focused on them. Additionally, the trailing edge condition was a controversial subject as the numerical implementation was causing many singularities.

A very fundamental method to study flow over aerofoils is the conformal transformation [21] of a circle into an aerofoil. In this approach the flow around the aerofoil is transformed through a number of transformations into a flow around a circular cylinder for which the solution is known. The flow field is then obtained by transforming the properties found using the same transformation used before. Another technique to deal with aerofoils in uniform flow is thin aerofoil theory which is applicable to thin aerofoil sections [23]. For such a case, the aerofoil can be simulated by a vortex sheet placed along the camber line. The camber line is close to the chord line so the vortex sheet falls approximately on the chord line. The camber line is considered to be a streamline and consequently it contains the velocity flow information. This statement leads to the fundamental integral equation which gives the velocity on the boundary of an aerofoil.

A vortex distribution method was followed by Prandtl [23] for the calculation of the flow velocity over finite wings. Replacing the finite wing with a bound vortex and the sides of it with free trailing vortices, the superposition of a finite number of these vortices leads to vortex filaments chordwise of the wing and thus an integral equation for the total velocity. A different approach was introduced by Morino [25] who developed a Boundary Integral Equation (BIE) for three dimensional bodies with complex configuration in unsteady compressible potential flow in oscillating arbitrary motion. The method is based on Green's theorem for the Laplace equation in potential flow assuming that the oscillation of the body is relatively small in the air frame of reference. The integral equation is solved on the surface and leads to the velocity potential and consequently to the velocity not only on the surface of the body but also in the field. This last fact is of great importance as it implies that the aerodynamic properties can be defined in the flow field which is very interesting from an aeroacoustics point of view. Maskew's [26] approach is very similar to Morino's. The difference is that he is using source and doublet strengths and the frame of reference is a fixed observer in the free space. This work was mostly based on Hess and Smith's study [22]. Applying the Green's function theorem and changing

the boundary condition inside and outside the body surface allows the solution of more advanced problems such as surface displacements.

Apart from all the above computational techniques there are analytical expressions that give the velocity around two or three dimensional geometries. The velocity and the velocity potential for a sphere in uniform mean flow are known and the same applies to a circle under certain conditions [23]. The Janzen-Rayleigh series [27] gives the maximum velocity on a cylinder not only in incompressible but also in compressible flow. In an extended work Van Dyke [28] provides additional information for the velocity potential around a circle including compressibility effects. Moreover, Lighthill [29] has done a lot of theoretical investigation for flow past bodies where he gives the maximum velocity formula for elliptical sections. All the above analytical expressions that we described are of great interest because they can be used to validate computational results.

## 2.3 Trailing edge conditions

Steady state potential aerodynamics of lifting bodies is a field where there has been a lot of investigation. Unsteady phenomena are of more interest as they reflect realistic situations. Oscillatory motion of aerofoils or wings is a very important subject and requires more conditions to be satisfied. The flow is regarded as inviscid and in the region of the trailing edge remains sensible i.e. no infinities in either flow velocities or in the pressure should appear in the solution at the sharp trailing edge. In addition such phenomena at the trailing edge are not within the scope of this thesis. Having a brief look in the aerodynamics literature we can see the debate which is going on for the Kutta [30] condition and the various solutions that have been suggested during these years. The basic disagreements concern the mathematical representation of the Kutta condition and its implementation in numerical terms. There should not be a separation between the case of the steady and the unsteady type of flow. The ideal would be one set of boundary conditions that satisfies both cases and it is applicable in each case. There are many different approaches to expressing the trailing edge condition in the literature, all meaning the same thing, the well known Kutta condition [23]: ‘The flow leaves the sharp trailing edge of an airfoil smoothly and the velocity there is finite’.

A very interesting computational approach for the application of the Kutta condition was the additional element at the surface of the trailing edge [31]. Figure 2.1 shows the trailing edge ( $\Gamma$ ) configuration and the wake element ( $\Gamma_w$ ).

In this numerical solution the actual trailing edge point is not a stagnation point. The velocity which is calculated at the midpoints of the side trailing edge elements has infinite value. Figure 2.2 shows the midpoints of the trailing edge elements. This technique actually meets the conditions that Maskell suggested which was that the flow must leave the trailing edge parallel to the upper or lower surface depending on the rotation direction of the vorticity. In summary the boundary conditions can be described in the following two sentences:

- The total normal velocity at the exterior midpoint of the trailing edge element is zero;



Figure 2.1: Trailing edge configuration.

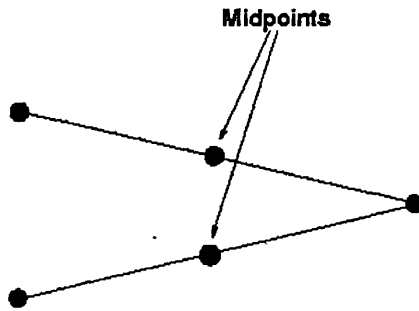


Figure 2.2: Midpoints of the trailing edge side elements.

- The pressures are equal at the midpoints of the side trailing edge elements.

Since the trailing edge angle is finite the normal component of the velocity from both sides of the aerofoil must vanish. Therefore, it is useful to assume that the pressure difference there is also zero:

$$\Delta p_{TE} = 0. \tag{2.1}$$

If the circulation is modelled by a vortex distribution ( $\gamma$ ), then this can be expressed as:

$$\gamma_{TE} = 0, V_1 = V_2. \tag{2.2}$$

These are the total velocities on the upper and on the lower trailing edge point as shown in Figure 2.3.

Recalling Kelvin’s theorem [31] which states that the time rate of change of circulation around a closed curve consisting of the same fluid elements is zero, the above

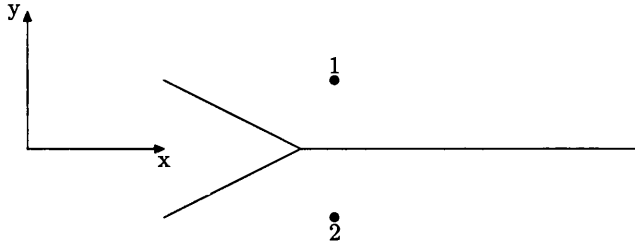


Figure 2.3: Points on each side of the wake geometry

statement summaries the following expression:

$$\begin{aligned}
 \frac{D\Gamma}{Dt} &= 0, \\
 \Gamma_w + \Gamma_b &= 0, \\
 \Gamma_w &= -\Gamma_b, \\
 \phi_w &= \phi_2 - \phi_1, \\
 \phi_w &= \Delta\phi.
 \end{aligned}
 \tag{2.3}$$

Thus the circulation around the lifting body ( $\Gamma_b$ ) is equal and opposite to the circulation around the starting vortex ( $\Gamma_w$ ). Morino and Kuo also investigated steady and unsteady potential aerodynamics. They introduced a boundary integral equation using the Green's function method which is applicable to complex configurations [25]. The equation is valid for both steady and oscillatory motion if the appropriate Green's function is used. It is implemented using panels and it was applied to two and three dimensional bodies. The value of  $\Delta\phi$  is continuous at the trailing edge and the vorticity is shed from the trailing edge and goes into the field. The  $\Delta\phi$  remains constant along the wake line and has the same value it had at the trailing edge. This means that the starting vortex which originates at the trailing edge does not grow in strength but rolls up allowing a steady circulation around the lifting body. Concluding, we could say that in potential inviscid irrotational flows there is vorticity generated at the trailing edge which is transported to the field by the wake but this vorticity remains constant.

## 2.4 Numerical issues

In aeroacoustics there are some parameters that should be carefully checked before any calculation. Because of the nature of the problem (aeroengines), we are more interested in high frequencies (short wavelength) than in low ones. Considering the fact that we are investigating non-uniform flow we have to think of the characteristic length of the mean flow disturbance. Usually, this characteristic length is the geometrical length of the investigated body. Recalling the equation for the speed of sound we could write:

$$c = f\lambda,
 \tag{2.4}$$

where  $f$  is the frequency and  $\lambda$  is the wavelength. When referring to sound we have to define the frequency or the  $ka$  where  $k = 2\pi/\lambda$  the wavenumber, and  $a$  the characteristic length of the body. So with this way one is able to understand the relation from a physical point of view between the two wavelengths (source generated wavelength and characteristic length) or even better to make the problem dimensionless. Moreover, another major problem that arises in aeroacoustics is that the discretisation of the boundary surface should be finer for higher frequencies. This is well explained by Morino and Piva [32] where they suggest that 6 to 8 nodes would be enough within a wavelength. Increasing the number of elements in a grid ensures more accurate results. We can see from equation 2.4 that the higher the frequency, the smaller the wavelength, that is the smaller the minimum distance between the nodes. This last statement reveals another problem in the present field. A finer grid requires more elements and consequently more memory and disk space. Additionally, sound pressure contains real and imaginary part which means that the size of the original problem is doubled. The promising thing with boundary element methods is though that there is no need for storage for the field operations and values. As has already been mentioned the surrounding field does not need discretisation and values which need to be stored. Assuming that the number of nodes on the investigated body is  $n$  then the resulting (assembly) matrix for the velocity potential or pressure depending what BIE one uses, is size  $2n \times 2n$ . This matrix is a square matrix and belongs to the final linear system which needs to be solved in order to get the velocity potential or the pressure distribution on the surface. It is quite obvious that for large geometries and at high frequencies the problem becomes even worse.

There have been developed many techniques to overcome this problem. A very effective and relatively new technique is parallel programming. Up to some years ago we used to make use of only one processor to do all the calculations and so, we had to wait more. The idea of parallel programming is to use more than one processor at the same time each of which undertakes the same task. This, of course, is subject to the nature of the problem and the flexibility of the computer program to be parallelised and the availability of computer resources. There are various studies for parallel processing BEM in literature that show how to parallelise a BEM code [33] and how efficient it becomes after parallelisation. Moreover, the linear system matrices are fully populated (dense) which make the solution procedure even more time expensive. A way to deal with this problem is to use iterative solvers which are less computationally expensive in terms of memory requirements and relatively faster. Continuing on the same topic, fast multipole method [34, 35] and its combination with other techniques [36] is very efficient in speeding up the work of iterative solvers as it converges with a satisfactory number of iterations. Von Estorff [37] in a very detailed review paper addresses computational acoustics problems and lists a number of available methods other than BEM. He also points out some very useful tips for BEM to reduce computation time, such as the simplification of the body geometry. Structurally complicated parts of the geometry can be neglected if they are small compared to the wavelength.

## 2.5 Duct acoustics

Duct acoustics is of special importance as aeroengine noise generation is one of the most popular subjects in aeroacoustics. An aeroengine can be modelled as a duct with a rotor inside. It is very important to examine how sound propagates in a duct and furthermore how and when it is radiated in the atmosphere. We will briefly present some basic theoretical aspects of sound propagation in a circular duct. The rotor in a duct is considered a source of sound which, depending on the angular speed of the blades of the rotor, propagates or decays. We could describe sound pressure as a sequence of harmonics or spinning modes which fluctuate as a function of a distance from the rotor.

The pressure is associated with the rotor angular velocity  $\Omega = 2\pi f$ , where  $f$  is the angular frequency. Since it is a periodic function, it can be written as Fourier series [38]:

$$p(\theta, t) = \sum_{n=0}^{\infty} A_n \cos(nB(\theta - \Omega t) + \phi_n), \quad (2.5)$$

where  $B$  is the number of blades,  $n$  the number of the harmonic,  $\theta$  the angle between the radius of a specific point on the blade and the origin line of the cylindrical system and  $A_n$  and  $\phi_n$  are amplitude and phase variables respectively. In order for the sound to be radiated in the field, the acoustic pressure should be “strong” enough to propagate through a cylindrical duct and then be released in the atmosphere. The term “strong” enough means that the driving frequency of the current harmonic is above a critical value or the cut off frequency as it is called. In case it is, the sound wave will be transmitted through the duct. The cut off frequency is different for each harmonic as the wavelength is different. If the current harmonic frequency is less than the cut off frequency then the sound attenuates and does not radiate. So, it becomes apparent that there are harmonics that are of great interest as they generate a radiation field around the duct.

Sound radiation from an unflanged cylindrical duct was calculated by the Wiener-Hopf technique some years ago by Levine and Schwinger [39]. They obtained an explicit solution for the sound radiation of an unflanged circular pipe assuming that only plane waves can propagate in the pipe. Because of the complexity of the Wiener-Hopf method, simpler approximate methods were found. Tyler and Sofrin [38] in their study of duct propagation and radiation, proposed a formula for calculation of the acoustic radiation field due to propagating modes from a semi-infinite flanged duct with no flow. They used the Kirchhoff approximation, in which an estimated acoustic source strength at the duct face is inserted in the radiation integral. This work still remains the classical and detailed work on compressor noise. Among the researchers who have studied ducted fan noise, are Dunn et al. [40–42]. They combined the linearised equations of acoustics and the Helmholtz integral equation, and developed computer codes for the prediction of the sound field around aeroengines. The method is valid for a wide range of inflow Mach numbers and for engines with liners fitted. The fan is modelled as a superposition of monopoles or dipoles placed at the corresponding blade locations.

Hamdi and Ville [43, 44] introduced a new variational formulation by integral equations in order to solve Helmholtz’s equation. The method was valid for finite length ducts



with arbitrary shapes and was checked against experimental data. Hwang [45] introduced a rather different computational method for computing the Helmholtz integral equation for acoustic radiation and scattering problems. Unlike previous studies, this method allowed the surface integral to be integrated directly and globally. He noted that the accuracy of the numerical integration was increased by using high-order Gaussian quadrature formula. To date, there are many studies of sound radiation from ducts, pipes or similar shape bodies but most of them do not include flow effects. To complete the overview on duct acoustics we should mention that there have been developed methods applicable to axisymmetric bodies [2, 46–49] such as ducts that simplify the implementation of the integral formulation.

Apart from the BEM there are also analytical expressions for the prediction of sound. A related study in this field has been done by Chapman [50]. His paper determines the ray structure of a spinning acoustic mode propagating inside a semi-infinite circular cylindrical duct, and thereby determines the field radiated from the end of the duct. Hocter [51] continued Chapman's work and presented three formulae for the calculation of the sound radiated from a cylindrical duct and compared the directivity patterns. In 1994, Peake [52] investigated the radiation properties of an asymmetric cylinder. The results of his analysis suggested that scarfing can be used to modify the radiation directivity. The noise levels below the horizontal had been reduced at the expense of increasing the noise above the horizontal.

In recent years Keith and Peake extended their work to high-wavenumber acoustic radiation from a thin-walled axisymmetric cylinder [53] and from a thin-walled scarfed cylinder [54]. Both studies are based on the Geometrical Theory of Diffraction and on uniform asymptotic. As far as scarfing is concerned, the first indications show that scarfing decreases the sound radiation directed above the asymmetry line and increases below. The scarfed cylinder has real application on aeroengines where the the intake is diverted a little upward to try to direct noise radiation away from the ground.

## 2.6 Scattering and radiation

Boundary element methods (BEM) have extensively been used over the past 50 years to solve acoustic scattering and radiation problems. The BEM is sometimes referred to as the boundary integral equation method. The classical Helmholtz [55] integral equation is given by:

$$CP = \int_S G \frac{\partial P}{\partial n} - P \frac{\partial G}{\partial n} dS, \quad (2.6)$$

where  $C$  is a coefficient which takes different values on and off the boundary,  $G$  is the Green's function and  $P$  is the pressure. The BEM solves the Helmholtz integral equation in either a bounded interior domain or in an unbounded exterior domain and can be used to evaluate pressure in the field. In exterior scattering problems the objective is to solve the Helmholtz equation in an unbounded fluid domain due to the acoustic radiation of a structure due to an incident sound wave which interacts with the structure. In such a case, the total radiated pressure would be the sum of the incident pressure generated by a

sound source in the absence of the obstacle and the scattered pressure in the presence of the obstacle. For scattering problems the pressure or the velocity potential must satisfy the Sommerfeld radiation condition [56] at infinity:

$$\lim_{R \rightarrow \infty} \left[ R \left( \frac{\partial \phi}{\partial R} + ik\phi \right) \right] = 0, \quad (2.7)$$

where  $R$  is the distance between the source and a field point and  $k$  the wavenumber. The radiation condition ensures that there are no additional contributions from a surface integral at infinity. The velocity potential should decrease with increasing  $R$ , a statement which is true for acoustic sources.

Helmholtz equation in solving radiation problems is usually associated with the non-uniqueness problem. This originates from the fact that if we apply the Helmholtz equation to an exterior and to an interior problem of the same body, then there should be a unique solution on the boundary. What happens though is that at some specific frequencies there is no unique solution. When the BIE is applied to exterior acoustics problems singularities occur in the resulting algebraic equations at these characteristic frequencies. It should be pointed out that these characteristic frequencies have no physical meaning for the exterior boundary value problem under consideration, which has a unique solution for all frequencies. The non-uniqueness problem is a purely mathematical problem arising from the boundary integral formulation rather than from the nature of the physical problem. There have been done many investigations to overcome the non-uniqueness problem. By far, the combined Helmholtz integral equation formulation proposed by Schenk [57] in 1968 and the composite Helmholtz integral equation presented by Burton and Miller [58] in 1971 are the most popular approaches. Schenk combined the surface Helmholtz integral equation with the interior Helmholtz integral equation to form an overdetermined system of equations, which was then solved using the least squares procedure and could give a unique solution at all frequencies. However, the method fails if the interior points are located on a node of the interior domain. Schenk's formulation was improved by Wu and Seybert [59]. In their paper an effective and simple BEM technique was presented which forces the constraint of each Combined Helmholtz Integral Equation Formulation (CHIEF) to be satisfied in a weighted residual sense over a small interior region. This improved formulation uses a CHIEF block which is simply a four-noded tetrahedron, rather than CHIEF points in the numerical implementation so that it can alleviate the nodal surface difficulty.

Burton and Miller's approach consists of a linear combination of the Helmholtz integral equation and its normal derivative. It has been proven that the linear combination of these two equations will yield a unique solution for all frequencies if the multiplicative constant of the normal derivative equation is appropriately chosen. However, the major difficulty in this formulation is that the normal derivative of the Helmholtz integral equation involves a hypersingular integral. Burton and Miller used a double surface integral to regularise this strong singularity. Even if both the Helmholtz integral equation and its normal derivative suffer from the non-uniqueness problem, it has been proven that the combination of the two integral equations leads to a unique solution. Although this

method appears to be robust for numerical implementation, it suffers from the main drawback of hypersingular integrals and it is computationally expensive to evaluate a double surface integral.

Segalman and Lobitz [60] adopted the work of Burton and Miller, extending the CHIEF. Their approach is considered an extension to the CHIEF method in that higher derivatives in addition to the function itself, are constrained to be zero at selected points in the interior domain. In 1989 Martinez [61] addressed the practical limitations of boundary integral methods and applied a modal boundary integral technique especially tailored to thin geometries of revolution. The problems chosen for its demonstration are cases of acoustic diffraction by an open-ended cylindrical duct containing a sound source, where the scattering wall's outer and inner surfaces are an infinitesimal distance apart, and are respectively rigid and either rigid or compliant.

It is essential to refer to the very modern techniques for solving the hypersingular BIE in three dimensional acoustics using a regularisation relationship which was introduced by Yan et al. [62]. In this technique the regularisation of the hypersingular integral in the CHIEF method is investigated through the double surface integral method. As is known, it is computationally expensive to evaluate a double surface integral. With this method though, the computational cost for calculating CHIEF is comparable to that of solving the conventional Helmholtz integral equation as the number of frequencies to be computed increases.

Acoustic wave scattering from axisymmetric bodies subject to a non-axisymmetric incident wave was presented by Kim et al. [63] by means of the Helmholtz integral equation method. By employing Fourier expansions of dependent variables in the circumferential angle, they obtained decoupled integral equations for each of the Fourier expansion terms. Therefore, they needed to discretise only the generator rather than the surface, which offered significant advantages in computational effort compared to the surface discretisation method. Although the number of Fourier expansion terms needed to achieve convergence increased as the frequency became higher, it was still smaller than or at least comparable to the number of nodal points along the generator, which indicated that their method was very efficient in the case of axisymmetric bodies. They noted that the present formulation could easily be extended to the radiation problem of axisymmetric bodies. Wu [64] dealt with acoustic radiation and scattering in a perfect waveguide. He applied a BEM where the Green's function and its derivatives were interpolated by a set of shape functions. This interpolation technique was used to speed up the matrix formation procedure and resulted in two to three times less time in comparison with conventional BEM.

Wang et al. [65] developed a unique boundary integral method to analyse the exterior acoustic radiation problem of axisymmetric bodies with arbitrary boundary conditions. The new formulation derived from Burton and Miller's method, used isoparametric elements. More specifically, they demonstrated that the use of tangential operators regularising the hypersingular kernel in the normal gradient equation, contributed to compute all integrals in the equation without much extra effort compared with the surface Helmholtz integral equation, since the resulting equation had the same order of singularity as the surface Helmholtz integral equation. The velocity and pressure functions were then expressed in Fourier series with respect to the angle of revolution, such that the surface in-

tegrals were reduced to line integrals along the generator of the body. Furthermore, they presented a new formula to precisely evaluate all the singular integrals of the Green's function and its derivatives over the circumferential angle in terms of complete elliptic integrals.

This historical review on the sound scattering and radiation problems that was presented in this chapter gives an overview of the state of the art in this particular field of aeroacoustics. The technical issues and the mathematical difficulties were addressed and potential solutions were briefly discussed. The literature survey was mostly focussed on the boundary element techniques and the achievements that have been obtained up to now. The need to solve aeroacoustics problems using coupling methods is increasing and more specifically when talking about scattering problems in non-uniform flows is out of great interest. Applications on lifting bodies where the wake occurs is a subject which needs further investigation in order to examine its effect on the sound propagation. The present work is going to present a boundary integral method for sound scattering applicable to non-uniform compressible and incompressible flows taking into consideration the wake effect.

# Chapter 3

## Boundary integral method

A boundary integral formulation for dealing with noise scattering and radiation problems is presented in this chapter. The study does not involve any transonic speeds because at these Mach numbers a more advanced investigation is required and the problem is not a linear problem any more, due to the non-linear phenomena that occur. In this chapter an analysis for compressible and incompressible velocities in potential flow is presented. The wave equation with and without flow is solved and is transformed to the Helmholtz integral equation. Taking the Helmholtz equation as a reference point we present an integral formulation which includes more terms than the Helmholtz and can cover more advanced radiation problems with complex geometries. This equation is valid for lifting bodies considering the wake effect which in the present case is prescribed depending on the body geometry. It is applied to both two and three dimensional bodies.

### 3.1 Helmholtz equation for quiescent fluid

In the absence of uniform flow and dissipation, the compression of fluid elements takes place adiabatically. The acoustic amplitude is small relative to the undisturbed mean pressure, and a first approximation to the wave equation governing propagation may be derived by linearising the equations of motion. This approximation tends to be better at lower frequencies because viscous dissipation and heat transfer by thermal conduction are weaker when the acoustic wavelengths (which increase with the decreasing frequency) are longer. From a mathematical and a physical point of view, sound is a wave that propagates through a fluid. Therefore, we should expect that in order to get an actual perception of how the sound is radiated from a body, we have to use the three dimensional wave equation.

Consider a body  $B$  of boundary surface  $S$  in an infinite acoustic medium  $B'$  of mean density  $\rho_0$  and speed of sound  $c$ . The body  $B$  can be either a vibrating structure (in a radiation problem) or a passive obstacle (in a scattering problem). Now consider the sound radiated into the unbounded stationary fluid from a time-harmonic volume source  $q(\mathbf{x}_1, t) = \phi(\mathbf{x}_1, \omega) \exp(-i\omega t)$  of radian frequency  $\omega$ . Applying the linearised continuity

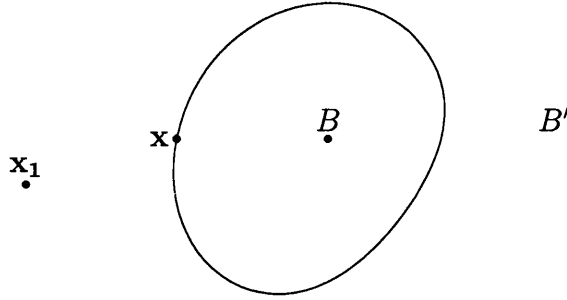


Figure 3.1: Body in an infinite acoustic medium.

equation [66]:

$$\frac{1}{\rho_0} \frac{\partial \rho}{\partial t} + \text{div} \mathbf{v} = q, \quad (3.1)$$

where  $\rho$  is the density of the medium and  $\mathbf{v}$  the acoustic particle velocity. Assuming small amplitude waves in a stationary ideal fluid with no body forces, the Bernoulli's equation is:

$$p = \rho_0 \frac{\partial \phi}{\partial t}, \quad (3.2)$$

where  $p$  is the acoustic pressure. For arbitrary and small adiabatic changes  $p$  is related to  $\rho$  with the following equation [66]:

$$\rho = -\frac{p}{c^2} \quad (3.3)$$

where  $c$  is the speed of sound. Substituting  $\mathbf{v} = \nabla \phi$  and equations 3.2 and 3.3 in equation 3.1 we end up with the following expression:

$$\left( \frac{\partial^2}{c^2 \partial t^2} - \nabla^2 \right) \phi = -q. \quad (3.4)$$

The velocity potential of the unsteady motion is governed by equation 3.4 and evidently oscillates at the same frequency as the source. The substitution  $\phi(\mathbf{x}_1, t) = \phi(\mathbf{x}_1, \omega) e^{-i\omega t}$  transforms equation (3.4) into the inhomogeneous Helmholtz equation:

$$\nabla^2 \phi + k^2 \phi = q, \quad (3.5)$$

where  $\phi$  is the velocity potential and  $k = \omega/c$  is the acoustic wave number. This equation must be satisfied in the acoustic domain  $B'$ . The sound pressure can be evaluated by,  $p = -i\rho_0 \omega \phi$ . The case of a unit point source  $q(\mathbf{x}, \omega) = \delta(\mathbf{x} - \mathbf{x}_1)$  where  $\delta$  denotes the Dirac delta function, defines the frequency domain Green's function which satisfies:

$$\nabla^2 G + k^2 G = \delta(\mathbf{x} - \mathbf{x}_1). \quad (3.6)$$

The above equation can be solved by the method of Fourier transforms but this analysis is outside the scope of the present study. After applying the Fourier transform [66] we

obtain the Green's function in the frequency domain:

$$G(\mathbf{x}_1, k) = -\frac{e^{ik|\mathbf{x}-\mathbf{x}_1|}}{4\pi|\mathbf{x}-\mathbf{x}_1|}. \quad (3.7)$$

Including the exponential time factor, equation 3.7 represents a continuous wave propagating radially outward at speed  $c$  from a source at  $\mathbf{x}_1$ . The amplitude decreases with distance  $|\mathbf{x}-\mathbf{x}_1|$ . In the corresponding time domain situation, the formulation would be:

$$\left(\frac{\partial^2}{c^2\partial t^2} - \nabla^2\right)\phi = \delta(\mathbf{x}-\mathbf{x}_1)\delta(t-\tau). \quad (3.8)$$

The right-hand side of the equation represents an impulsive point source that vanishes, except at  $t = \tau$ . After the Fourier transform we get:

$$G(\mathbf{x}, \mathbf{x}_1, t-\tau) = \frac{\delta(t-\tau-|\mathbf{x}-\mathbf{x}_1|/c)}{4\pi|\mathbf{x}-\mathbf{x}_1|}. \quad (3.9)$$

Using the direct formulation via Green's second identity, equation 3.5 is reformulated into a boundary integral equation defined on the boundary surface  $S$  as follows:

$$C(\mathbf{x}_1)\phi = \int_S \left(G\frac{\partial\phi}{\partial\mathbf{n}} - \frac{\partial G}{\partial\mathbf{n}}\phi\right) dS, \quad (3.10)$$

where  $G$  is the free-space Green's function due to a time-harmonic point source at  $\mathbf{x}_1$  and  $\mathbf{x}$  is a point which is located on the surface.  $C(\mathbf{x}_1)$  is a coefficient that depends on the location of  $\mathbf{x}_1$ . Equation 3.10 is the Helmholtz integral equation [14]. The explicit expression for the free-space Green's function is equation 3.7 written in the following form:

$$G = \frac{e^{ikR}}{4\pi R}, \quad (3.11)$$

where  $R = |\mathbf{x}-\mathbf{x}_1|$ . The leading coefficient  $C(\mathbf{x}_1)$  in equation 3.10 can take the following values:

$$C(\mathbf{x}_1) = \begin{cases} 1 & \mathbf{x}_1 \text{ in } B' \\ 1 - \int_S \partial G_0 / \partial \mathbf{n} dS & \mathbf{x}_1 \text{ on } S \\ 0 & \mathbf{x}_1 \text{ in } B \end{cases}$$

where  $G_0$  is the Green's function at  $k = 0$ . To solve the Helmholtz integral equation we have to say a few words on each term of this equation. So, the Green's function gradient normal to the surface is:

$$\frac{\partial G}{\partial \mathbf{n}} = G \frac{(ikR-1)}{R} \frac{\partial R}{\partial \mathbf{n}}. \quad (3.12)$$

For scattering problems, the velocity potential  $\phi$  is decomposed into two parts:

$$\phi = \phi^{inc} + \phi^{sct}, \quad (3.13)$$

where  $\phi^{inc}$  is the incident field,  $\phi^{sct}$  is the scattered and  $\phi$  the total. The incident field is specified assuming an acoustic source somewhere in the field. When point  $\mathbf{x}$  is located

on the surface  $S$  then we talk about surface velocity potential and according to equation 3.1 the Helmholtz integral equation takes the form of equation 3.10.

So the surface potential is obtained if we solve equation 3.10 for  $\phi(\mathbf{x}_1)$ . Knowing the surface pressure, and having as input the the incident field on the surface we are led to the calculation of the scattered field.

To calculate the scattered field, equation 3.10 must be solved subject to the appropriate boundary condition and can then be used to calculate the radiated field. The boundary condition for a rigid surface is that the surface normal velocity be zero or in terms of the incident and the scattered fields  $\phi^{inc}$  and  $\phi^{sct}$ ,

$$\frac{\partial \phi^{inc}}{\partial n} = -\frac{\partial \phi^{sct}}{\partial n}. \quad (3.14)$$

The incident field generated by a point source has the form:

$$\phi^{inc} = \frac{e^{ikR}}{4\pi R}. \quad (3.15)$$

## 3.2 Boundary integral method for unsteady flow

As we have already mentioned Boundary Integral Methods (BIM) for aerodynamics have been studied for many years. The novelty takes place when BIM are used for aeroacoustic purposes where a combination of acoustics and aerodynamics is needed. To define the problem, we can say that we are trying to find the sound in a moving medium where the flow is non-uniform. Starting from the velocity potential we are able to estimate the total acoustic pressure. To do so, we need to make clear all the assumptions and the considerations we have made. We decompose the velocity potential into two parts. One part is the steady part and the other is the unsteady. The unsteady part denotes the acoustic perturbation which we assume small and not strong enough to affect the steady one. Consequently, in all the mathematical operations we neglect the second order terms claiming that they are small compared to the first order ones. Linking all the above and adding some facts about the wake configuration, we explain that we solve a linear problem. In a complete analysis there should occur two non-linearities. In the present work we do not deal with them. In the case of a free-wake analysis the wake geometry depends on the solution procedure, while using a prescribed wake as in the present case the non-linearities disappear as the wake geometry is predefined.

Let us extend now the study of section 3.1 to the case where non-uniform flow is included. Before displaying the mathematical procedure related to the present problem, it would be wise to refer to the assumptions that have been made which are displayed and explained at the beginning of this chapter.

Shifting to the aeroacoustic problem now we can write the corresponding differential equation for the same problem but with an acoustic source  $q(\mathbf{x}, t) = q(\mathbf{x}_1, \omega)e^{-i\omega t}$  of radian frequency  $\omega$ , in the field in the frequency domain [17]:

$$\nabla^2 \phi + k^2 \phi - 2ikM \frac{\partial \phi}{\partial x} - M^2 \frac{\partial^2 \phi}{\partial x^2} = \delta(\mathbf{x} - \mathbf{x}_1). \quad (3.16)$$



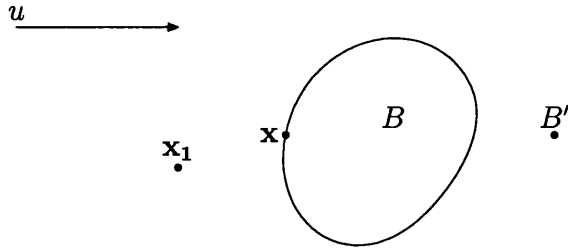


Figure 3.2: Body in mean flow with an acoustic source nearby.

Let the undisturbed mean flow be specified by a velocity potential  $\bar{\phi}(\mathbf{x})$ , with mean velocity  $u$  in the  $x$  direction. Consider an irrotational sound disturbance  $\phi'(\mathbf{x}, t)$ , and set:

$$\phi(\mathbf{x}, t) = \bar{\phi}(\mathbf{x}) + \phi'(\mathbf{x}, t). \quad (3.17)$$

Both terms of the equation are treated the same way and the only difference is that the second contains the unsteady exponential term  $\exp(-i\omega t)$ . The total velocity can be expressed in terms of the velocity potential as:

$$\mathbf{v}(\mathbf{x}, t) = \nabla\phi(\mathbf{x}, t). \quad (3.18)$$

So the velocity is similarly the sum of a steady and an unsteady part as follows:

$$\mathbf{v}(\mathbf{x}, t) = \bar{\mathbf{v}}(\mathbf{x}) + \mathbf{v}'(\mathbf{x}, t). \quad (3.19)$$

To make things clearer let us start from the aerodynamic analysis of the problem. According to Morino [16] the differential equation in the time domain that gives the velocity potential for a body in potential compressible flow is:

$$\nabla^2\phi - \frac{1}{c^2}\frac{\partial^2\phi}{\partial t^2} = \Sigma, \quad (3.20)$$

where  $\Sigma$  is the term that represents the non-linear terms that occur in the transonic region. Assuming the problem is linear:

$$\nabla^2\phi - \frac{1}{c^2}\frac{\partial^2\phi}{\partial t^2} = 0. \quad (3.21)$$

Converting differential equation 3.16 to an integral equation, Morino introduced a formulation for both compressible and incompressible potential flows. Additionally, the formulation is valid for bodies which produce lift and have wake following the trailing edge as shown in Figure 3.3.

The boundary integral formulation is given by [10]:

$$\begin{aligned} \phi(\mathbf{x}, t) = & \int_{\Gamma} \left[ \frac{\partial\phi}{\partial\hat{\mathbf{n}}} G - \phi \frac{\partial G}{\partial\hat{\mathbf{n}}} + G \frac{\partial\phi}{\partial t} \left( \frac{\partial\theta}{\partial\hat{\mathbf{n}}} + 2\frac{\mathbf{u}\cdot\mathbf{n}}{c^2} \right) \right]^{\theta} d\Gamma \\ & - \frac{1}{c^2} \int_{\Gamma} \left[ G \phi \frac{\partial}{\partial t} [\mathbf{u}\cdot\mathbf{n}(\mathbf{u}\cdot\nabla\theta - 1)] \right]^{\theta} d\Gamma - \int_{\Gamma_w} \Delta\phi \frac{\partial G}{\partial\mathbf{n}} d\Gamma_w, \end{aligned} \quad (3.22)$$

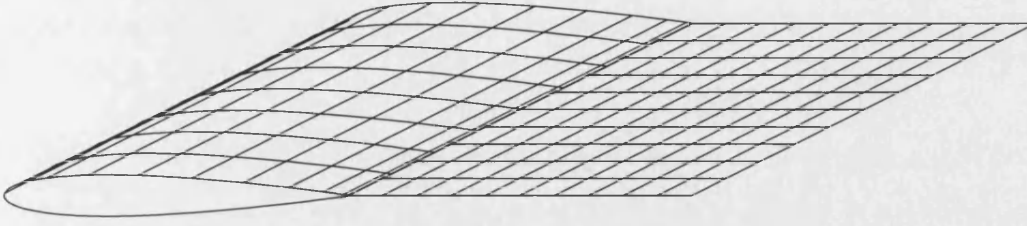


Figure 3.3: Wing and wake geometry in mean flow.

where

$$\frac{\partial}{\partial \hat{n}} = \frac{\partial}{\partial n} - \frac{1}{c^2} \mathbf{u} \cdot \mathbf{n} \cdot \mathbf{u} \cdot \nabla \quad (3.23)$$

where  $[\dots]^\theta$  denotes evaluation at time  $\tau = t - \theta$ , and  $\theta$  is the time for the sound to travel from the source to the observer when  $\mathbf{x}$  is a point in the field while  $\phi(\mathbf{x}, t)$  is the value of the velocity potential at that point.  $\Delta\phi$  is the wake strength and it will be discussed in detail in section 3.4. The above equation is the full boundary integral equation in potential compressible flow for lifting bodies. It contains information that is important at higher Mach numbers and cannot be neglected as in the incompressible case. In the present case this equation becomes simpler as the second integral term can be eliminated because the velocity of the body is constant and does not involve any relative motion with respect to the free motion of the body. The reduced equation takes the form:

$$\phi(\mathbf{x}, t) = \int_{\Gamma} \left[ \frac{\partial \phi}{\partial \hat{n}} G - \phi \frac{\partial G}{\partial \hat{n}} + G \frac{\partial \phi}{\partial t} \left( \frac{\partial \theta}{\partial \hat{n}} + 2 \frac{\mathbf{u} \cdot \mathbf{n}}{c^2} \right) \right]^\theta d\Gamma - \int_{\Gamma_w} \left[ \Delta \phi \frac{\partial G}{\partial n} \right]^\theta d\Gamma_w. \quad (3.24)$$

In order to work out the total velocity potential we need to use the integral equation for both the steady part and the unsteady. When the observer is located on the boundary  $\Gamma$ , then the above integral equation can be used to evaluate the velocity potential,  $\phi$  on  $\Gamma$ .

The Green's function  $G$  represents the potential field associated with a uniformly moving acoustic source. In compressible potential flow in the positive  $x$  direction the Green's function is [67]:

$$G_{3D} = -\frac{e^{ik\sigma}}{4\pi S} \quad (3.25)$$

where

$$\begin{aligned} S &= \sqrt{(x - x_1)^2 + \beta^2 [(y - y_1)^2 + (z - z_1)^2]}, \\ \beta &= \sqrt{1 - M^2}, \\ \sigma &= \frac{M(x - x_1) + S}{\beta^2}, \\ M &= \frac{u}{c}. \end{aligned} \quad (3.26)$$

is the Mach number of the flow. For the steady aerodynamic problem the Green's function is given by setting the wave number in equation 3.25 to zero:

$$G_{3D} = -\frac{1}{4\pi S}. \tag{3.27}$$

Once  $\phi$  is obtained, the same equation is used to get the velocity potential,  $\phi(\mathbf{x}, t)$  anywhere in the field in terms of the values of  $\phi$  and  $\partial\phi/\partial n$  on the surface of the body and  $\Delta\phi$  on the wake. Once  $\phi$  is known on the surface, the velocity and pressure can be calculated anywhere in the field. Similarly, the velocity is obtained using equation 3.18:

$$\mathbf{v}(x) = \int_{\Gamma} \left[ \frac{\partial\phi}{\partial\hat{n}} \nabla G - \phi \frac{\partial\nabla G}{\partial\hat{n}} + \nabla G \frac{\partial\phi}{\partial t} \left( \frac{\partial\theta}{\partial\hat{n}} + 2\frac{\mathbf{u}\cdot\mathbf{n}}{c_0^2} \right) + G \frac{\partial\phi}{\partial t} \left( \frac{\partial\nabla\theta}{\partial\hat{n}} \right) \right] d\Gamma - \int_{\Gamma_w} \left[ \Delta\phi \frac{\partial\nabla G}{\partial\mathbf{n}} \right]^\theta d\Gamma_w. \tag{3.28}$$

We now continue with the simpler case of incompressible flow for which the boundary integral equation [16] is:

$$\phi(\mathbf{x}, t) = \int_{\Gamma} \left[ \frac{\partial\phi}{\partial\hat{n}} G - \phi \frac{\partial G}{\partial\hat{n}} \right] d\Gamma - \int_{\Gamma_w} \Delta\phi \frac{\partial G}{\partial\mathbf{n}} d\Gamma_w.$$

As we can observe some terms are eliminated from the corresponding equation for compressible flow. This is explained if we note that in compressible flow we have density variations which lead to the occurrence of the Prandtl-Glauert factor  $\beta = \sqrt{1 - M^2}$ . In incompressible flow i.e. at low Mach number we can approximate  $M^2 = 0$ , so  $\beta = 1$ . Following these approximations, the Green's function for the incompressible case is [16]:

$$G_{3D} = -\frac{e^{ikR}}{4\pi R}, \tag{3.29}$$

where  $R = \sqrt{(x - x_1)^2 + (y - y_1)^2 + (z - z_1)^2}$ .

For the steady part, the Green's function is given by:

$$G_{3D} = -\frac{1}{4\pi R}. \tag{3.30}$$

As far as the wake term is concerned, a more extended analysis is required to obtain the wake strength,  $\Delta\phi$ . The wake is an aerodynamic phenomenon which occurs in the case of lifting bodies in flow. It is a zero thickness vortex layer where a discontinuity in the velocity potential  $\phi$ , and consequently in the tangential velocity component, appears. The question that arises at this point is the value of the velocity potential at the trailing edge. From a physical point of view, the velocity potential cannot change its magnitude abruptly: there should be a smooth transfer from the trailing edge to the wake. The answer to this question is given by the Kutta condition which eventually leads to the wake strength. In one of the following sections we present an extended analysis of the wake

boundary conditions where we give the velocity potential jump across the trailing edge, which is then transferred to the wake. The wake is assumed to spring from the trailing edge and its surface coincides with that swept by the trailing edge during its motion [68]. We could say that the wake is springing from the trailing edge and is extending to infinity.

We first apply the integral equation for the steady aerodynamic part where we set the appropriate boundary conditions. The boundary,  $\Gamma$ , of the body is assumed to be impermeable. If  $\mathbf{v}_B$  is the velocity of any point on  $\Gamma$ , then  $(\mathbf{v} - \mathbf{v}_B) \cdot \mathbf{n} = 0$ . Hence, the boundary condition on  $\Gamma$  is:

$$\frac{\partial \bar{\phi}}{\partial \mathbf{n}} = \mathbf{u} \cdot \mathbf{n}, \quad (3.31)$$

where  $\mathbf{u}$  is the velocity of the point on the surface of the body. The boundary condition at infinity is:

$$\bar{\phi} = 0. \quad (3.32)$$

In the case of the unsteady part, the same integral equation is used and exactly the same procedure is followed. The only difference is that the wake strength is given by a different expression. To complete the integral formulation for the acoustic section we have to set the boundary conditions,  $\partial \phi' / \partial \mathbf{n}$ . We consider Neumann boundary conditions, so:

$$\frac{\partial \phi'}{\partial \mathbf{n}} = 0. \quad (3.33)$$

Once the velocity is known, there is only one step before we reach the final unknown which is pressure. Bernoulli's equation is the desired equation which combines all the previous information about velocity potential and velocity and leads to pressure. As we mentioned in the beginning of this work, we examine both of the above flow cases. The pressure at infinity is constant but in our assumptions is taken as zero. For potential compressible flows, Bernoulli's equation has the form:

$$\frac{\partial \phi}{\partial t} + \frac{1}{2} \mathbf{v}^2 + \frac{1}{\gamma - 1} c^2 = \frac{1}{\gamma - 1} c_0^2, \quad (3.34)$$

where  $\gamma$  denotes the ratio of specific heats and  $c = c(\mathbf{x}, t)$  is the speed of sound evaluated using the local values of pressure and density. Assuming that the pressure at infinity is zero, equation 3.34 is reduced to the material derivative which measures the rate of change following the motion of a fluid particle:

$$-\frac{p'}{\rho} = \frac{\partial \phi'}{\partial t} + \bar{\mathbf{v}} \cdot \nabla \phi'. \quad (3.35)$$

### 3.3 Boundary integral method for two dimensional problems

Integrating the Green's function over the  $z$  axis in three dimensions results in the corresponding formulation for the two dimensions one. Similarly to the three dimensional analysis, let us start with the case without flow. Consider a two dimensional body in the

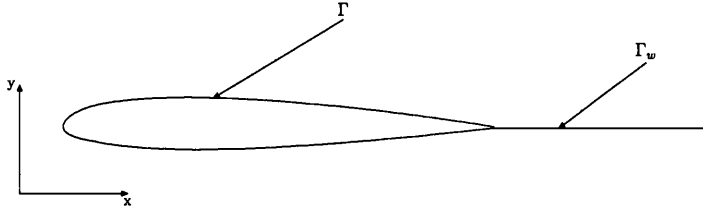


Figure 3.4: Aerofoil and wake geometry in mean flow.

acoustic medium where the mean flow velocity is zero as shown in Figure 3.4. In order to solve the scattering problem under these conditions we need the appropriate Green's function as the formulation remains the same as in the three dimensional analysis. In the time domain the two dimensional Green's function is given by [66]:

$$G_{2D}(\mathbf{x}, \mathbf{x}_1, t - \tau) = \frac{H(t - \tau - |\mathbf{x} - \mathbf{x}_1|/c)}{2\pi\sqrt{(t - \tau)^2 - (\mathbf{x} - \mathbf{x}_1)^2/c^2}}, \quad (3.36)$$

where  $H(x)$  is the Heaviside unit function defined by  $H(x) = 0$  for  $x < 0$ ,  $H(x) = 1$  for  $x > 0$ . In the frequency domain the technique that we follow to find this is to integrate the three dimensional Green's function with respect to the  $z$  direction. So the two dimensional Green's function is [55]:

$$\begin{aligned} G_{2D} &= -\frac{i}{4}H_0^{(2)}(kR), \\ R &= |\mathbf{x} - \mathbf{x}_1|, \end{aligned} \quad (3.37)$$

where  $H_0^{(2)}$  is the zero order Hankel function of the second kind. Since the normal derivative of the Green's function will be used in the integral equation, the explicit expression for the normal derivative is given here:

$$\frac{\partial G}{\partial n} = \frac{ik}{4}H_1^{(2)}(kR)\frac{\partial R}{\partial n}, \quad (3.38)$$

where  $H_1^{(2)}$  is the Hankel function of the second kind of order one [69]

$$\begin{aligned} H_0^{(1)}(x) &= J_0(x) + iY_0(x), \\ H_0^{(2)}(x) &= J_0(x) - iY_0(x), \end{aligned} \quad (3.39)$$

where  $J_0$  and  $Y_0$  are Bessel functions of the first and second kinds, respectively, of order zero. The procedure continues with case of compressible flow. Integrating equation 3.25 with respect to  $z$  from  $-\infty$  to  $\infty$  we find:

$$G_{2D} = -\frac{i}{4}\frac{e^{ikM(x-x_1)/\beta^2}}{\beta}H_0^{(2)}\left(\frac{kS}{\beta^2}\right). \quad (3.40)$$

If we set  $k = 0$  then we shift to the steady aerodynamic case where for two-dimensional bodies the Green's function is given by:

$$G_{2D} = -\frac{\log S/\beta}{2\pi\beta}. \tag{3.41}$$

Finally for the incompressible flow problem the Green's function for the unsteady case is:

$$G_{2D} = -\frac{i}{4}e^{ikM(x-x_1)}H_0^{(2)}(kR). \tag{3.42}$$

For the the steady aerodynamic case:

$$G_{2D} = -\frac{\log S}{2\pi}. \tag{3.43}$$

### 3.4 Wake boundary conditions

The wake is the region of flow left behind the trailing edge during the aerofoil motion. Its geometry can be approximated with a straight line which has zero thickness and extends to infinity. In the wake region the flow properties cannot be specified applying the principles of unsteady potential flow as in the rest of the fluid. This is the reason a more detailed analysis needs to be done in order to investigate this region. In order to thoroughly investigate the wake boundary conditions, we have to take into account the reflection and the refraction phenomena. Let us consider the shear layer of Figure 3.5.

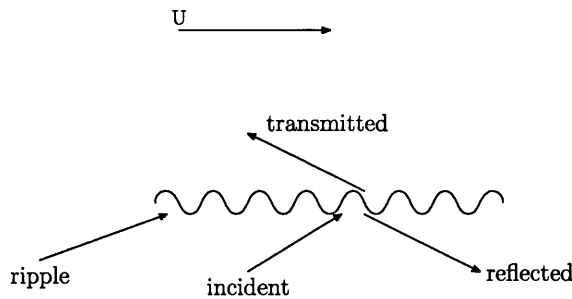


Figure 3.5: Sound reflection and transmission by a moving medium.

We can see a moving sound ripple with velocity  $U$  in the horizontal direction. Assume now an incident acoustic wave hitting the wake line. The result will be a reflected wave and a transmitted wave on the opposite side of the wake. The boundary conditions on the wake according to [70] are:

- the acoustic pressure must be continuous across the shear layer:  $\Delta p' = 0$ ,
- the streamline slopes must be equal on both sides,

$$\frac{U_{1y}}{U_{1x}} = \frac{U_{2y}}{U_{2x}}, \quad (3.44)$$

where  $U_{1y}$  and  $U_{2y}$  are the total velocities normal to the wake on each side,  $U_{1x}$  and  $U_{2x}$  are the total velocities parallel to the wake and  $U_{2y}$  is the sum of the velocities reflected and the incident waves while  $U_{1y}$  is the velocity of the transmitted wave. But the second boundary condition can be reduced to:

$$U_{1y} = U_{2y}, \quad (3.45)$$

which states that the component of the resulting velocity (flow plus acoustic) locally normal to the rippling interface is the same on both sides. The transformation from equation 3.44 to equation 3.45 is done assuming  $U_{1y}$  and  $U_{2y}$  very small. This is a reasonable assumption when considering a plane interface as in our case and consequently, we can ignore a component of the stream velocity that comes in due to sinusoidal surface inclination. This conclusion agrees with the form of boundary conditions given by Nark et al. [71] who show that the boundary conditions on the shear layer are:

- trailing edge acoustic pressure must be continuous across the shear layer:  $\Delta p' = 0$ ;
- trailing edge acoustic particle displacement must be continuous across the shear layer:  $\Delta y = 0$ ;

The first boundary condition was also used by Morino [12] when describing the boundary conditions on the wake. The second boundary condition is equivalent to equation 3.44. If we expand this boundary condition we end up with the same equation that Ribner [70] uses to describe the second boundary condition. The acoustic displacement [72] is defined as:

$$\begin{aligned} y_1 &= y_2, \\ \frac{\partial y_1}{\partial t} &= \frac{\partial y_2}{\partial t}, \\ U_{1y} &= U_{2y}. \end{aligned} \quad (3.46)$$

which is equation 3.45 and proves the equality of these two different expressions.

From the first boundary condition we deal with the acoustic pressure which is given by:

$$p' = \frac{D\phi'}{Dt} = \frac{\partial\phi'}{\partial t} + \mathbf{u} \cdot \nabla\phi' \quad (3.47)$$

where,  $\mathbf{u}$  is the mean flow velocity. The pressure following the linearised formulation rules comes from the unsteady small perturbation theory. Figure 3.6 shows the wake geometry and two points very close to the wake. Examining the pressure at each point and applying the first boundary condition we get:

$$p'_1 = \frac{D\phi'_1}{Dt} = \frac{\partial\phi'_1}{\partial t} + \mathbf{u}_1 \cdot \nabla\phi'_1 \quad (3.48)$$

$$p'_2 = \frac{D\phi'_2}{Dt} = \frac{\partial\phi'_2}{\partial t} + \mathbf{u}_2 \cdot \nabla\phi'_2 \quad (3.49)$$

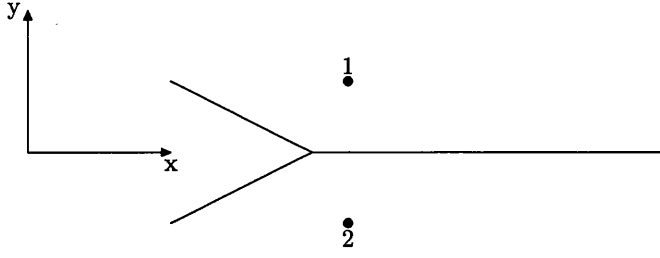


Figure 3.6: Points on each side of the wake geometry.

Then  $\Delta p' = p'_1 - p'_2 = 0$  gives [12]:

$$\begin{aligned} \frac{\partial \phi'_1}{\partial t} + \mathbf{u}_1 \cdot \nabla \phi'_1 - \frac{\partial \phi'_2}{\partial t} - \mathbf{u}_2 \cdot \nabla \phi'_2 &= 0, \\ \frac{\partial \Delta \phi'}{\partial t} + \mathbf{u}_W \cdot (\nabla \phi'_1 - \nabla \phi'_2) &= 0, \\ \frac{\partial \Delta \phi'}{\partial t} + \mathbf{u}_W \cdot \left( \frac{\partial \phi'_1}{\partial x_1} - \frac{\partial \phi'_2}{\partial x_2} + \frac{\partial \phi'_1}{\partial y_1} - \frac{\partial \phi'_2}{\partial y_2} \right) &= 0, \end{aligned} \quad (3.50)$$

where

$$\mathbf{u}_W = \frac{(\mathbf{u}_1 \cdot \nabla \phi'_1 - \mathbf{u}_2 \cdot \nabla \phi'_2)}{\nabla \phi'_1 - \nabla \phi'_2}. \quad (3.51)$$

Recalling the second boundary condition which simply states that  $y_1 = y_2$  we can rewrite the above equation as follows:

$$\frac{\partial \Delta \phi'}{\partial t} + \mathbf{u}_W \cdot \left( \frac{\partial \phi'_1}{\partial x_1} - \frac{\partial \phi'_2}{\partial x_2} + \frac{\partial \Delta \phi'}{\partial y} \right) = 0. \quad (3.52)$$

Moreover, knowing that the unsteady velocity,  $v_x = \partial \phi' / \partial x$ , we can write:

$$\begin{aligned} \frac{\partial \Delta \phi'}{\partial t} + \mathbf{u}_W \cdot (v_{1x} - v_{2x}) &= 0, \\ \mathbf{u}_W \cdot \nabla \Delta \phi' + \frac{\partial \Delta \phi'}{\partial t} &= 0, \\ \frac{D \Delta \phi'}{Dt} &= 0. \end{aligned} \quad (3.53)$$

Integrating the above equation we conclude:

$$\Delta \phi'(\mathbf{x}, t) = \Delta \phi'(\mathbf{x}_{TE}, t - \tau). \quad (3.54)$$

where,  $\mathbf{x}_{TE}$  is the trailing edge position. The above equation states that the wake strength remains constant following a wake point  $\mathbf{x}_W$  travelling on the wake. Where,  $\tau = (\mathbf{x}_W - \mathbf{x}_{TE}) / \mathbf{u}_W$  is the time for a wake point to travel from the trailing edge to a position on the



wake line at time  $t$ . To make things clearer,  $\Delta\phi$  is the initial value of the wake strength which comes from the Kutta condition and in the steady state case remains constant.

Applying the boundary integral equation at each point we derive a formulation valid on the wake. The boundary integral equation is given by equation 3.24. Removing the last (wake) term of this equation we can prove why it exists there.

To validate our implementation of the boundary conditions on the wake we check our calculations against the boundary conditions suggested by [71]. The proposed analytical expression for the acoustic displacement across the wake is:

$$\left[ \frac{-\mathbf{v}'_n}{i\omega + (\mathbf{n} \cdot (\mathbf{n} \cdot \nabla \bar{\mathbf{v}}))} \right]_1 = \left[ \frac{-\mathbf{v}'_n}{i\omega + (\mathbf{n} \cdot (\mathbf{n} \cdot \nabla \bar{\mathbf{v}}))} \right]_2 \quad (3.55)$$

where  $\mathbf{v}'_n$  is the unsteady velocity normal to the wake surface. The check to be done is to secure the equality of displacement across the wake, and consequently to satisfy the analytical formula proposed by the above reference. This analytical formula is a function of steady and unsteady velocities which are calculated with numerical methods, a fact which makes the approach to the wake more difficult. In order to achieve better approach to the wake surface, we used Richardson's extrapolation method [73]. Figure 3.7 shows the difference between the upper and lower displacement across the wake for approximately three chords length. Starting from a distance of  $10^{-3}$  m from the wake and applying the extrapolation method, we achieve very good agreement between the two sides of the wake. From Figure 3.7 it can be seen that the boundary conditions on the

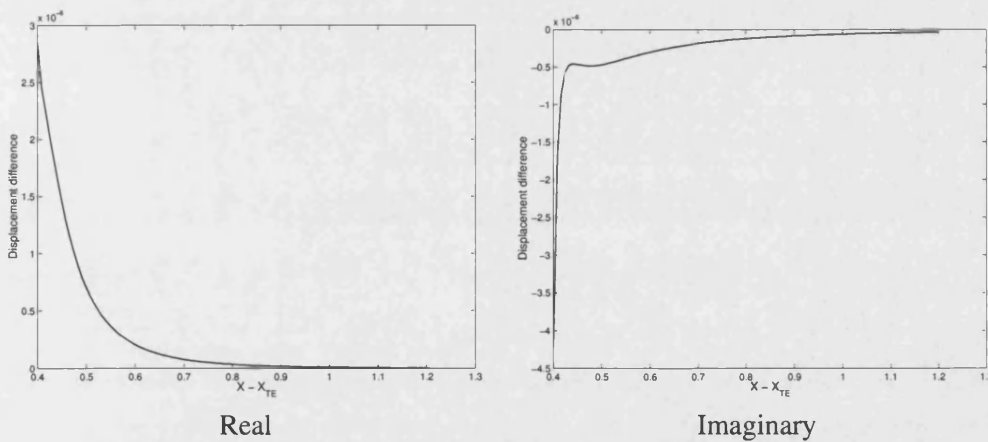


Figure 3.7: Difference in acoustic displacement across the wake,  $ka = 1.6$ .

wake are satisfied with good accuracy.

### 3.5 Duct sound propagation theory

Apart from the lifting bodies (wing, aerofoil) test cases we applied the boundary integral method to a duct. In this section we briefly present the theoretical background of the

sound scattered by a duct with a spinning rotor inside. The sound field radiated from a duct inlet can be decomposed into a set of acoustic modes. Each of these modes has a specific directivity pattern which varies with frequency. The investigation of the important modes which eventually propagate and radiate in the field is out of great interest and study for noise generation mechanisms. The pressure fluctuation in terms of position and time is represented by [38]:

$$p(\theta, t) = \sum_{n=1}^{\infty} p_n(\theta) \cos[n\omega t + \phi_n(\theta)]. \quad (3.56)$$

This equation states that the pressure fluctuation at any position  $\theta$ , is a sum of harmonics. Expanding the cosine term:

$$p(\theta, t) = \sum_{n=1}^{\infty} [p_n(\theta) \cos \phi_n(\theta)] \cos n\omega t - \sum_{n=1}^{\infty} [p_n(\theta) \sin \phi_n(\theta)] \sin n\omega t. \quad (3.57)$$

Since the quantities in brackets are functions of position only, they may be expanded in Fourier series of the form:

$$\sum_{m=0}^{\infty} (A_m \cos m\theta + B_m \sin m\theta). \quad (3.58)$$

Substituting equation 3.58 in equation 3.57 we obtain the total pressure in terms of modes:

$$p(\theta, t) = \sum_{n=1}^{\infty} \sum_{m=-\infty}^{\infty} p_{mn}, \quad (3.59)$$

where  $p_{mn}$  is:

$$p_{mn} = A_{mn} \cos(m\theta - n\omega t + \phi_{mn}). \quad (3.60)$$

Equation 3.59 can be written as a sinusoidal azimuthal variation and a Bessel function radial variation. Thus, the total pressure is made up of modes of the form:

$$p_{mn}(r, \theta) = \sum_m \sum_n A_{mn} J_m(k_{mn}r) e^{im\theta}, \quad (3.61)$$

where  $m$  is the circumferential mode and  $A_{mn}$  is the amplitude or the mode coefficient and can be found by applying the Hankel Transform [74]. The mathematical expression of the series is:

$$F(k_{mn}) = \sum_{n=1}^{\infty} A_{mn} J_m(k_{mn}r), \quad (3.62)$$

where  $k_{m1}r, k_{m2}r, k_{m3}r, \dots$  are the positive zeros of:

$$J'_m(k_{mn}r), \quad (3.63)$$

where  $J'_m$  is the first derivative of the Bessel function of order  $m$  and  $r$  is a position on the duct radius. Equation 3.62 is called a Dini series of Bessel functions and the coefficients  $A_{mn}$  are given by the formula:

$$A_{mn} = \frac{2k_{mn}^2 \int_0^1 t f(t) J_m(k_{mn}t) dt}{(k_{mn}^2 - m^2) J_m^2(k_{mn})}. \quad (3.64)$$

In our case the function  $f(t)$  is the total acoustic pressure and  $t$  is the non-dimensional radius of the duct. Therefore, equation (3.64) is modified to:

$$A_{mn} = \frac{2k_{mn}^2 \int_0^1 \frac{r}{r_{duct}} \phi^{tot} J_m(k_{mn}r) d\frac{r}{r_{duct}}}{(k_{mn}^2 - m^2) J_m^2(k_{mn})}, \quad (3.65)$$

where  $r_{duct}$  is the duct radius. The integral in the above equation is calculated using the trapezoidal rule. Inside the duct, the eigenvalues  $k_{mn}$  vary and modes can be cut-off (decay exponentially).

Now consider the cylindrical duct shown in Figure 3.8. The tip Mach number of the spinning rotor inside the duct, is  $M_t = ka/m$ . Consider an acoustic mode denoted by

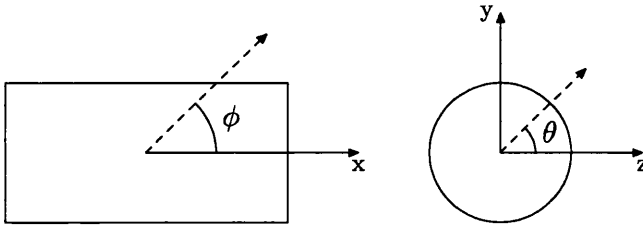


Figure 3.8: Geometry of a cylindrical duct.

$A_{mn}$  of the form:

$$p = p_0 e^{i(-\omega t + m\theta + k_x x)} J_m(k_r r). \quad (3.66)$$

A system of cylindrical coordinates  $(r, \theta, x)$  is shown in Figure 3.8 to describe the mode. In equation 3.66  $p$  represents the pressure,  $t$  the time and the modal parameters are  $\omega$  the frequency,  $m$  the azimuthal order,  $k_x$  the axial wavenumber and  $k_r$  the radial wavenumber. The duct wall is assumed to be hard so from the boundary condition  $\partial p / \partial x = 0$  we get  $J'(k_r r_{duct}) = 0$ . The axial wavenumber is given by:

$$k_x^2 = k^2 - k_r^2, \quad (3.67)$$

where  $k = \omega/c$  is the free space wavenumber. This equation is very important as it determines which modes propagate and which modes attenuate for a given frequency. When  $k < k_r$ ,  $k_x$  is imaginary and the frequency that this corresponds to, is called 'cut off'. On an opposite case it is called 'cut on'. These 'cut on' and 'cut off' frequencies are better explained when expressed in dimensionless velocity. Assume the noise source in the duct is a rotor of radius  $r_{rotor}$  which is spinning with angular velocity  $\Omega$  and the

tip Mach number is,  $M_t = \Omega r_{rotor}/c$ . The Mach number that the azimuthally varying pressure can propagate inside the duct is,  $M = \omega r_{duct}/c$ . Bearing in mind that,  $\omega = m\Omega$ , we can easily understand that for a specific mode of order  $m$  to propagate (i.e to be 'cut on'), the condition  $M_t > M$  needs to be satisfied.

### 3.6 Integral representation of the incident field

To calculate the radiated field from a spinning rotor in a duct we simulate the noise pressure from the rotating rotor with a disk source and follow the Boundary Integral formulation presented in Section 3.1. The incident field assuming a disk source, is given by:

$$\phi = \int_0^{2\pi} \frac{e^{i(kR + m\theta)}}{4\pi R} d\theta, \quad (3.68)$$

and the gradient is:

$$\frac{\partial \phi}{\partial n} = \int_0^{2\pi} \frac{e^{i(kR + m\theta)}}{4\pi R} \frac{(ikR - 1)}{R} \frac{\partial R}{\partial n} d\theta, \quad (3.69)$$

where  $m$  is the azimuthal order,  $\theta$  is the angle on the disk source and  $R$  is given by:

$$R = [r_{rotor}^2 + r_1^2 - 2r_{rotor}r_1 \cos \theta + (z_{rotor} - z_1)^2]^{1/2}, \quad (3.70)$$

where  $r_{rotor}$  is the rotor radius, while subscript 1 denotes the source position.

# Chapter 4

## Numerical implementation

In this chapter we present the numerical procedure that was followed in order to implement the BIE on the two and three dimensional example geometries. Several numerical difficulties arose due to some special geometrical characteristics and due to mathematical weaknesses of the method. To overcome these problems we applied some techniques that allowed us to avoid more complicated and time expensive solutions.

To numerically solve the problem, the geometry is sub-divided into a series of smaller regions in which the integral equation is solved. Each region is referred to as an element and the process of subdividing a domain into a finite number of elements is referred to as discretisation. Elements are connected at specific points, called nodes, and the solution must be continuous along common boundaries of adjacent elements. In general, three dimensional geometries are more difficult to handle because of the bigger number of elements and the more complicated discretisation. A very well structured way to manipulate such problems is to use the GTS library [75] which is an open source free software and stands for the GNU Triangulated Surface library. This is a library which provides a set of useful functions to deal with three dimensional surfaces meshed with triangles. It is written in the C programming language with an object-oriented approach which is well structured, improves the performance, and is user friendly. The main features include the capacity to extract information about the topological properties of elements and a wide variety of available operations to handle the surface. A list of options concerning grid refinement, complicated surface operations (union, intersection), metrics and graphs are also available.

Once the elements have been defined, we have to determine how the variation of the field variable across the element is to be approximated or represented. In most cases a polynomial interpolation function is used. The number of nodes assigned to an element dictates the order of the interpolation function which can be used. Interpolation functions are also referred to as shape functions or approximating functions.

The collocation method allows us to calculate the unknown boundary data. An approach is to establish a system of equations with as many unknowns as equations. The principle of collocation is to locate the control point sequentially at all nodes of the discretisation. Because linear and higher order polynomial shape functions lead to nodes which belong to more than one element, it is essential to introduce a global node num-

bering system which does not depend on the element. The collocation procedure leads to a linear system of equations. This part of the solution is time consuming and can be accelerated by parallel programming methods (Chapter 5).

## 4.1 Surface discretisation in three dimensions

In order to apply the boundary element method, the boundary is discretized into smaller regions called elements and the solution is determined in terms of discrete values of some primary boundary variables at the nodes. In the present case these elements are triangles and consequently consist of three nodes. Figure 4.1 presents a three dimensional discretisation of a wing and a closer view of it.

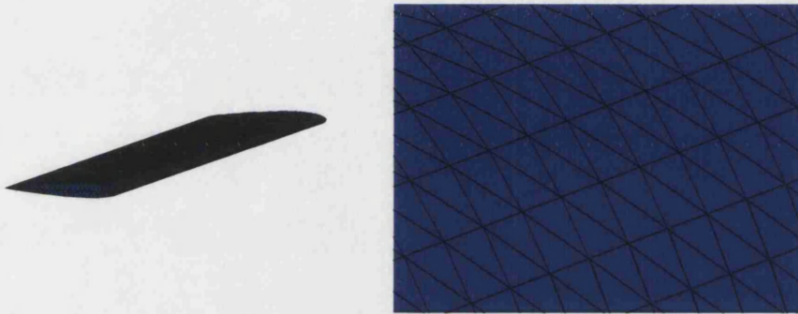


Figure 4.1: Three dimensional discretisation of a wing.

At the element level, the solution to the governing equation is replaced by a continuous function approximating the distribution of a property,  $f$ , over the element domain expressed in terms of the unknown nodal values  $f_1, f_2, f_3$  of the solution  $f$  as shown in Figure 4.2. A system of equations in terms of  $f_1, f_2$  and  $f_3$  can then be formulated for the element. Using isoparametric elements as in this case, the local (nodal) coordinates are expressed as  $(\xi, \eta, 1 - \xi - \eta)$ .

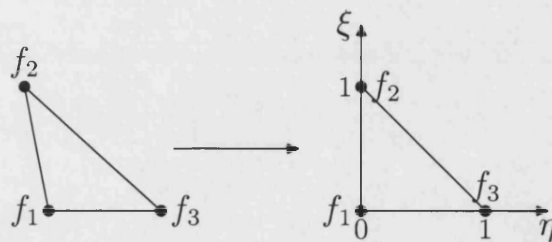


Figure 4.2: A triangular element and the corresponding isoparametric element.

A mapping function  $\mathbf{x} = g(\xi, \eta)$  is used to relate global and local coordinates. This function is called shape function and has different value for each node. Thus the coordi-

nates of the global points are expressed in:

$$\mathbf{x}(\xi, \eta) = \sum_{i=1}^3 L_i(\xi, \eta) \mathbf{x}_i, \quad (4.1)$$

where  $L_i(\xi, \eta)$  is the shape function. For each element the shape functions are:

$$L_1 = \xi, \quad L_2 = \eta, \quad L_3 = 1 - \xi - \eta. \quad (4.2)$$

The acoustic variable is calculated at the nodal points and so on each element it is approximated by a linear function.

## 4.2 Boundary discretisation in two dimensions

In two dimensions, the discretisation process requires the division of the boundary into a finite number of isoparametric elements as shown in Figure 4.3. These elements consist

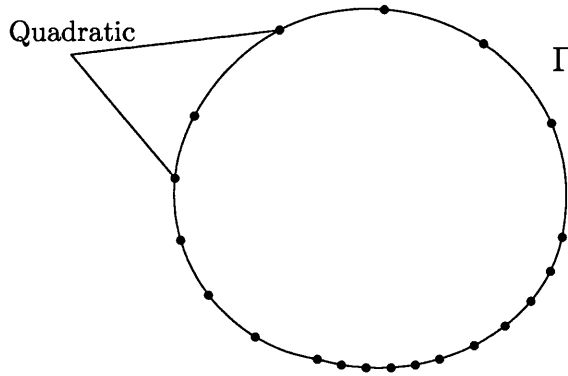


Figure 4.3: Boundary discretisation.

of three nodes (quadratic elements). The geometry of each element can be represented by interpolation between the nodal points. Thus the coordinates of the points are expressed in terms of nodal coordinates and the associated shape functions as follows:

$$\mathbf{x}(\xi) = \sum_{i=1}^n \mathbf{x}_i L_i(\xi), \quad (4.3)$$

where  $\mathbf{x}_i$  is the position of nodal points,  $L_i(\xi)$  are the shape functions with a local coordinate  $-1 \leq \xi \leq 1$  and  $n$  is the number of nodes on the element. The shape functions for the quadratic elements which were used in the present work are:

$$L_1 = \frac{1}{2}\xi(\xi - 1), \quad L_2 = (1 - \xi)(1 + \xi), \quad L_3 = \frac{1}{2}\xi(\xi + 1). \quad (4.4)$$

Figure 4.4 shows a quadratic element and the nodal coordinates on it.

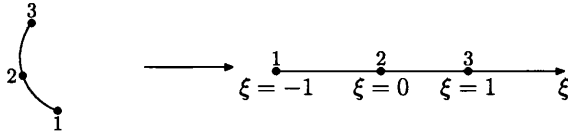


Figure 4.4: Quadratic element.

### 4.3 Integration

The integration of the terms in the boundary integral equation can be easily carried out if we relate the global coordinate system to the nodal (local) coordinate system. The nodal system is based on the three-noded linear surface element whose local components are  $\xi$  and  $\eta$ . The global Cartesian coordinates,  $\mathbf{x}$ , are related to the nodal global coordinates,  $\mathbf{x}_i$ , using equation 4.1 in three dimensions and equation 4.3 in two dimensions.

At first we interpolate the global coordinates, using equation 4.1 and then we use the same set of shape functions to interpolate the surface variables  $\phi$  and  $\partial\phi/\partial n$ . Therefore on each element,  $S_j$ , as shown in Figure 4.5 we have:

$$\phi = \{L\}^T \{\phi\}, \tag{4.5}$$

$$\frac{\partial\phi}{\partial n} = \{L\}^T \left[ \frac{\partial\phi}{\partial n} \right], \tag{4.6}$$

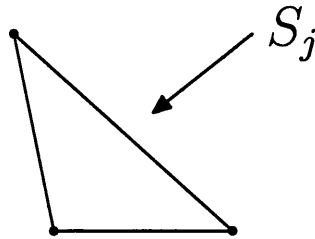


Figure 4.5: An element of the body grid.

where  $\{\phi\}$  and  $\{\frac{\partial\phi}{\partial n}\}$  contain the nodal values of  $\phi$  and  $\frac{\partial\phi}{\partial n}$  respectively. The superscript  $T$  denotes transpose, the symbol  $\{\cdot\}$  denotes vector and the symbol  $[\cdot]$  denotes matrix. To complete the integration procedure we have to interpolate and integrate the Green's function. Thus, we have:

$$[M] = \int_{S_j} \frac{\partial G}{\partial n} \{L\}^T dS, [N] = \int_{S_j} G \{L\}^T dS, \tag{4.7}$$

where  $[M]$  and  $[N]$  are two square global matrices and so according to the previous development, the Helmholtz integral equation is written as:

$$\{\phi\} = [N] \left\{ \frac{\partial\phi}{\partial n} \right\} - [M] \{\phi\}, \tag{4.8}$$



For a boundary value problem, there is only one unknown ( $\phi$ ) at each node of  $S$ . Rearranging equation 4.8 yields:

$$[A]\{\phi\} = \{b\}, \quad (4.9)$$

where  $[A]$  is a square matrix and  $b$  is the right-hand side vector.

## 4.4 Singularities

As previously mentioned the evaluation of the velocity potential on the surface is taking place on the nodes. This causes some numerical problems: when the collocation point is placed at a node the singularities occur. These singularities are logarithmic due to the Green's function formula in the steady state. More specifically, in the two dimensional case the Green's function is a Hankel function, for which we need the first derivative in order to find the velocity potential. This means that we automatically move to higher order singularities which are more difficult to deal with. The differentiation of the Green's function gives a logarithmic function which needs to be treated by using the appropriate quadrature. In three dimensions the Green's function has the form of  $1/R$  and the first derivative the form of  $1/R^2$  which in the integral equation are both improper integrals. We do the integration numerically over the surface and therefore the way to overcome all these problems is to use a generalised Gaussian quadrature [76] which integrates exactly the logarithmic singularities on any of the nodes of the elements using a single formula. More specifically, all the integral equations of the boundary element method are evaluated using one of two methods: either regular Gaussian quadrature or a combination of regular and logarithmic Gaussian quadrature. The regular Gaussian quadrature is used to evaluate most of the integrals along the boundary, and the combined scheme is employed for integrals that are singular. All the integrals containing non-singular functions are evaluated using a regular form of Gaussian quadrature. The advantage of this scheme is that the same set of quadrature points can be used for constant, linear or higher order elements. This is very convenient from a computational point of view as there is no need for selection when it comes to different types of singularities.

## 4.5 Sharp edges

Another important issue that arises in scattering bodies is when these bodies contain sharp edges. At a corner the normal derivative of the Helmholtz integral equation cannot be defined, since the normal vector itself is discontinuous at a such point. There are various ways to face this problem; one can duplicate the corner node with a small gap between two nodes or place the collocation points not on the node but in the middle of the current element. In the present case the trailing edge of the aerofoil is a sharp edge where the surface normal changes direction as shown in Figure 4.6.

The approach used to overcome this problem is to consider that at the sharp edge there exist two points each of which has its own normal vector [65]. Figure 4.7 presents the

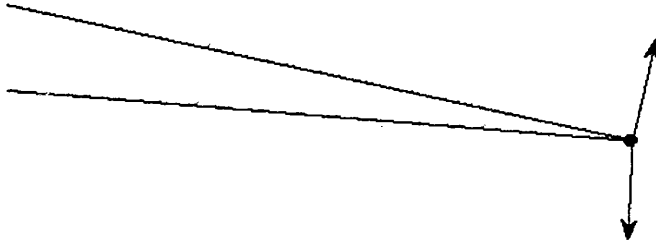


Figure 4.6: The normal vectors at the trailing edge .

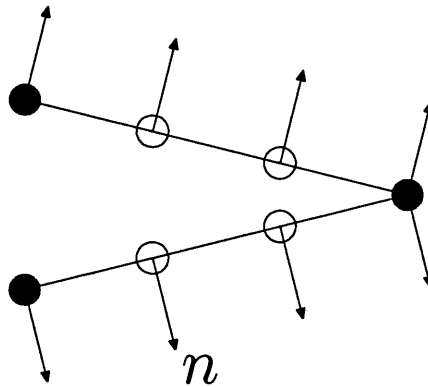


Figure 4.7: Double normal vectors at a sharp edge [2].

normals on a corner. With this technique we take into account both of the two different directions and introduce a smooth solution, avoiding the inaccuracy and unreliability of other techniques where we need to find the optimal gap between the two points or modify the mesh in order to move the collocation point away from the corner.

## 4.6 Validation examples

To demonstrate the accuracy and the efficiency of the boundary element method described above, selected cases of acoustic radiation and aerodynamic flow fields have been computed. The test cases include geometries for which there are analytical or numerical solutions to compare with. The first check for both three and two dimensional problems was to place an acoustic source inside the body and calculate the radiated field. This should be the same as the one computed using the integral method. The incident field which is simply the sound field generated by the source in the space is always known for the standard source types (monopoles, multipoles). The unknown scattered field satisfies the Helmholtz equation. In order to find the total pressure we have to add the incident and the

scattered field. Both the incident and the total field satisfy the same wave equation [14] for a given frequency. For three dimensional problems there are theoretical expressions for scattering around a sphere [56] and a pulsating sphere in uniform flow at low Mach number [19]. The aerodynamic part of the boundary integral method was checked against experimental results for a rectangular wing of aerofoil section NACA 0012 [3]. For the two dimensional calculations we compared aerodynamic part with analytical formulae for elliptical sections [29].

### Three dimensional validation problems

Let us start the validation procedure with a sphere in uniform flow and an acoustic source inside the body of the sphere. In the case of the sphere, a point source is placed inside the surface. According to the theory [77], the radiated pressure that is calculated by our method must be identical to the sound radiated directly from the source. We place a source inside the closed surface and calculate the sound it generates on the surface. Using the sound field on the surface, we can calculate the radiated sound. This should be identical to the sound radiated directly from the source. Figure 4.8 shows the velocity potential field for a sphere with an acoustic source in potential flow. The comparison between the computed values and the values given directly from the source show very good agreement. In the following figures  $a$  is the characteristic length which for a wing and an aerofoil is the chord, for a sphere the radius and for a duct the internal radius.

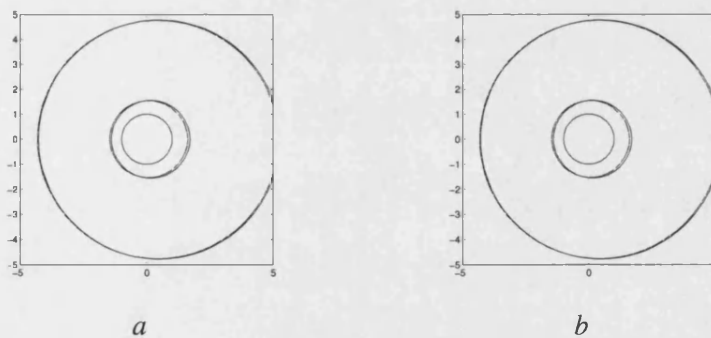


Figure 4.8: Velocity potential around a sphere in flow with  $M = 0.1$ ,  $a$ :  $ka = 1$ ;  $b$ :  $ka = 10$ . Solid line indicates analytical solution and dashed line indicates computed solution.

Looking at Figure 4.9 we can see how the agreement between theoretical ( $\phi_{thr}$ ) and computational ( $\phi_{com}$ ) values improves as the number of nodes ( $N$ ) on the sphere surface increases. Another way to validate our code is to calculate the scattered pressure of a plane wave. Figure 4.10 shows a sphere and an oncoming plane wave.

The analytical solution for the scattered pressure of a plane acoustic wave from a sphere of radius  $a$  at a distance  $R$  from the centre of the sphere and at an angle  $\theta$  from the

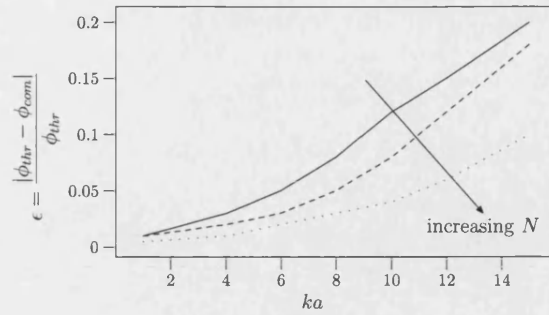


Figure 4.9: Error vs  $ka$  for  $N = 1080$ ,  $N = 2520$  and  $N = 4560$  for  $M = 0.6$ .

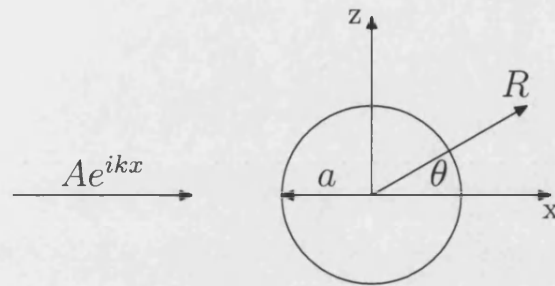


Figure 4.10: Plane wave on a sphere.

direction of the incoming wave is given by [56]:

$$P(R, \theta) = \sum_{n=0}^{\infty} (2n + 1) i^n P_n(\cos \theta) \frac{j'_n(ka)}{h'_n(ka)} h_n(kR), \quad (4.10)$$

where  $j_n$  is the spherical Bessel function of the first kind and  $h_n$  is the spherical Hankel function of the second kind.  $P_n$  denotes the Legendre polynomial of order  $n$ . The following figures confirm of the accuracy of the method and show the scattered pressure in the case of a plane wave for both analytical and computational methods. Moreover they show how accuracy improves as the number of nodes ( $N$ ) increases.

More specifically, a very satisfactory agreement of the two solutions is clearly illustrated in Figure 4.11 where a reasonable wave number ( $ka = 10$ ) is considered. A larger disagreement between the two solutions appears when we move to the far field,  $R/a = 8$ . Figure 4.12 which presents the error behaviour of pressure estimated according to the analytical formula of equation 4.10, for different wavenumbers and number of nodes, and shows that with a finer discretisation, the accuracy of the results improves.

To obtain a more realistic idea of how efficient the technique can be, it was checked against an analytical solution for a pulsating sphere in low Mach number flow. This analytical solution takes into consideration effects of non-uniform flow at low Mach number. A pulsating sphere is shown in Figure 4.13. The surface displacement corresponding to

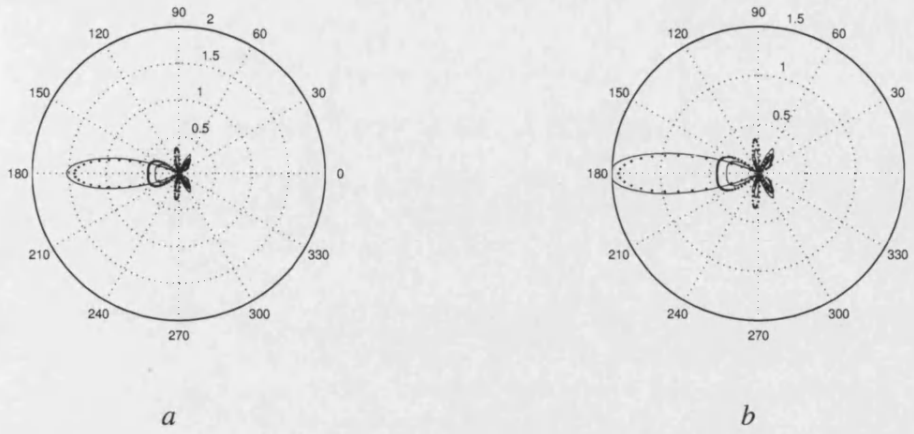


Figure 4.11: Scattered pressure field (real part),  $ka = 10$ ,  $a$ :  $R/a = 2$ ;  $b$ :  $R/a = 8$ . Solid line indicates analytical solution and dot line indicates computed solution.

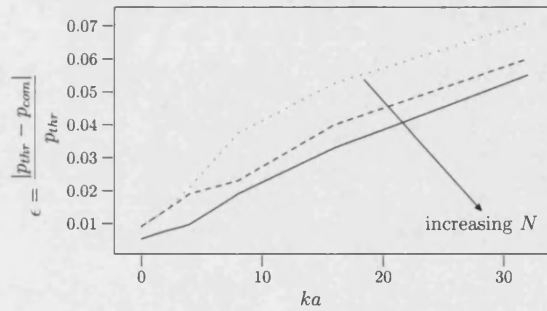


Figure 4.12: Error in scattered pressure from a plane wave on a sphere for  $N = 1080$ ,  $N = 2520$  and  $N = 4560$ .

the pulsating sphere is given by:

$$\eta(\mathbf{x}, t) = a\epsilon e^{-i\omega t}. \tag{4.11}$$

Considering the displacement, the boundary condition on the surface is [20]:

$$\frac{\partial \phi}{\partial r} = \epsilon c(ika + 3M \cos \theta)e^{-i\omega t}, \tag{4.12}$$

where  $\theta$  is the spherical polar angle as indicated in Figure 4.13. The resulting solution for the velocity potential of a pulsating sphere is [20]:

$$\phi = \epsilon \frac{c}{k} e^{-ikM(r+a^3/2r^2) \cos \theta} \left[ \frac{ika \frac{h_0^{(2)}(kr)}{h_0^{(2)'}(ka)} + \frac{3M}{2}(2 - k^2a^2) \frac{h_1^{(2)}(kr)}{h_1^{(2)'}(ka)} \cos \theta \right] e^{-i\omega t}, \tag{4.13}$$

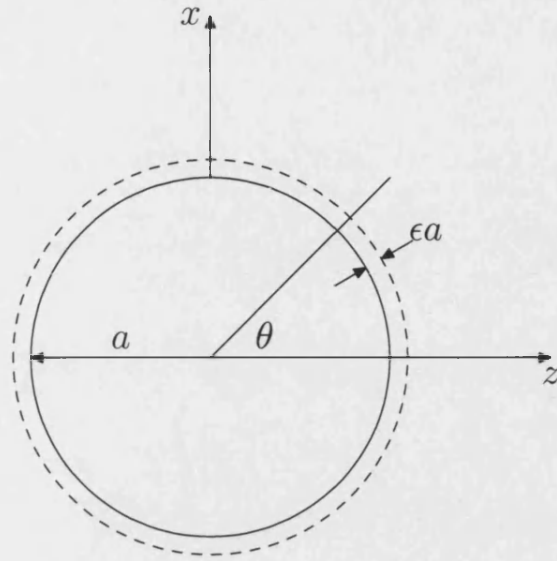


Figure 4.13: Pulsating sphere.

where  $h_n^{(m)}$  is the spherical Hankel function of the  $m$ th kind and  $n$ th order. Applying the boundary conditions given by equation 4.12 we solve the problem of a pulsating sphere. Figure 4.14 shows the error in acoustic velocity potential based on the analytical and the computational methods for two different Mach numbers. Observing the results we can see that we obtain a very good agreement between the two solutions. This is a very promising and positive result as it certifies that the method is working for the prediction of sound in non-uniform flows at low Mach numbers. The Mach numbers were chosen carefully as the analytical formula is valid for low speed flow and breaks down after a certain point.

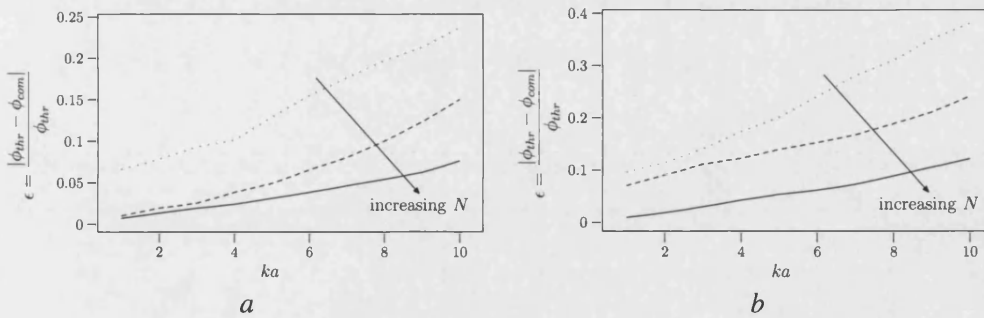


Figure 4.14: Velocity potential error ( $\epsilon$ ) vs  $ka$  for a pulsating sphere for  $N = 1080$ ,  $N = 2520$  and  $N = 4560$ .  $a: M = 0.1$ ;  $b: M = 0.3$ .

## 4.7 Aerodynamic validation

In order to assess the accuracy of the steady aerodynamic part of our calculations, it was checked against experimental results [3] for an unswept wing in uniform flow at high Reynolds number ( $4.5 \times 10^6$ ). The cross section of the wing is a NACA 0012 and the geometry is shown in Figure 4.15. The measurements were performed at  $M = 0.3$  and at

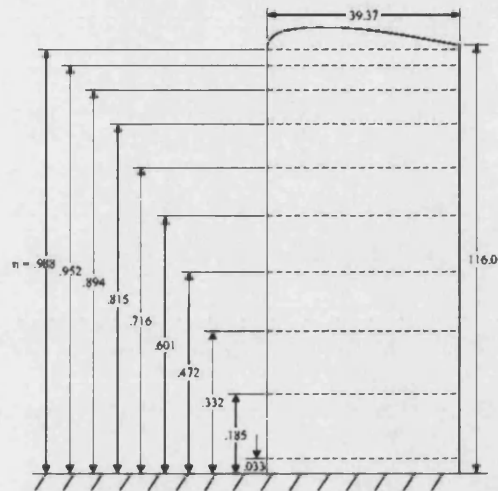


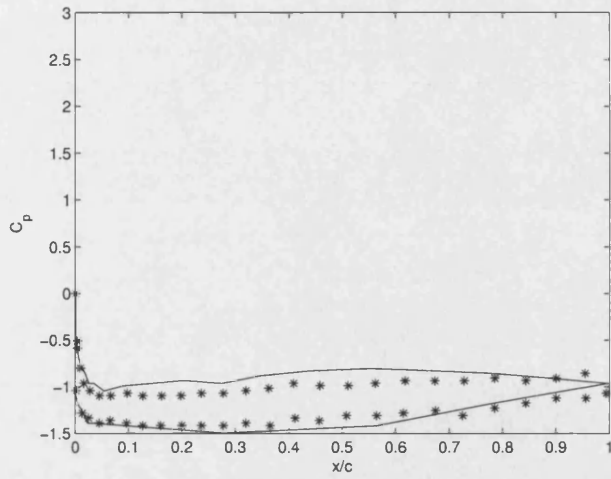
Figure 4.15: Plan view of semispan wing indicating pressure tap stations in inches [3].

certain range of angles of attack. Figures 4.20 – 4.18 show the pressure coefficient ( $C_p$ ) versus the dimensionless chord length ( $\eta$ ). The solid line indicates the computed pressure coefficient and the star symbols the corresponding experimental. To cover a wide range of cases we selected three positions (root, middle and tip) along the span of the wing for three different angles of attack. Moreover, we chose most of the comparisons to be made when the high lift devices are extended to thoroughly examine the validity of our results in more demanding conditions.

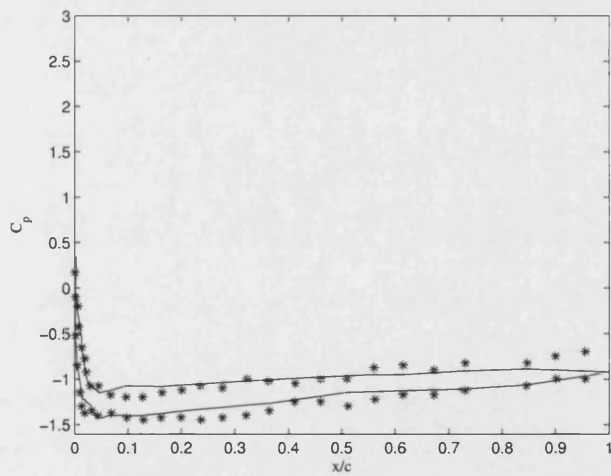
The results show a good and quite satisfactory agreement with the corresponding experimental data. Though, we have to keep in mind that it is not always feasible to simulate the exact flow conditions during the experimental procedure and consider all the factors that may affect it. Furthermore, our analysis simulates potential conditions and the experiments took place at high Reynolds number.

### Two dimensional validation

In order to validate our method for the two dimensional calculations we did the ordinary check where an acoustic source is placed inside the boundary so as to obtain the surface pressure and the sound radiated from the surface should be identical to the sound radiated directly from the source. Figure 4.22 shows the computed and the analytical unsteady



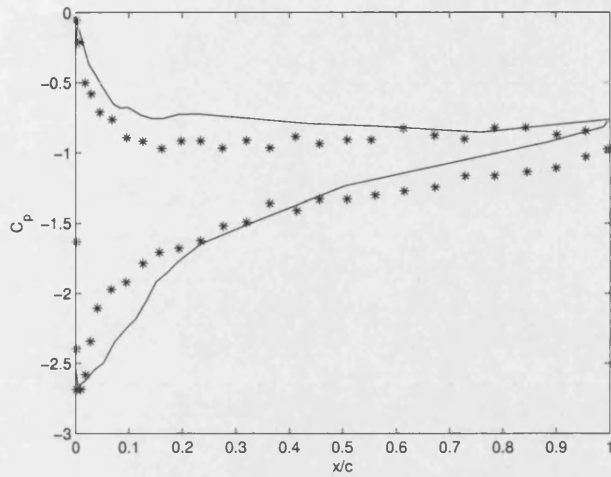
*a*:  $\eta = 0.033$ ;



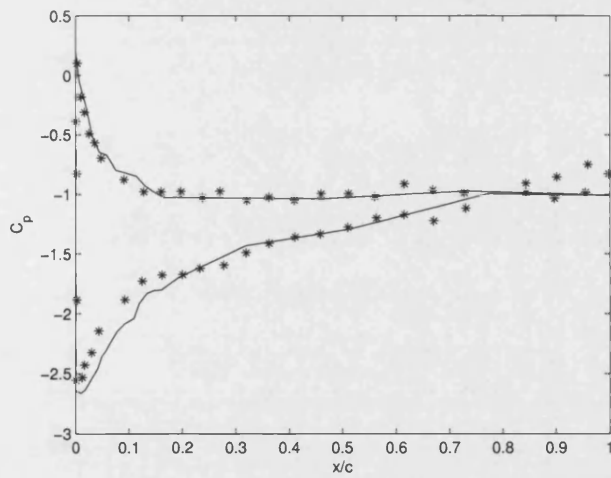
*c*:  $\eta = 0.472$ .

Figure 4.16: Pressure coefficient at  $M = 0.3$  and  $\alpha = 0^\circ$ . Solid line indicates computed and star symbols experimental results respectively.



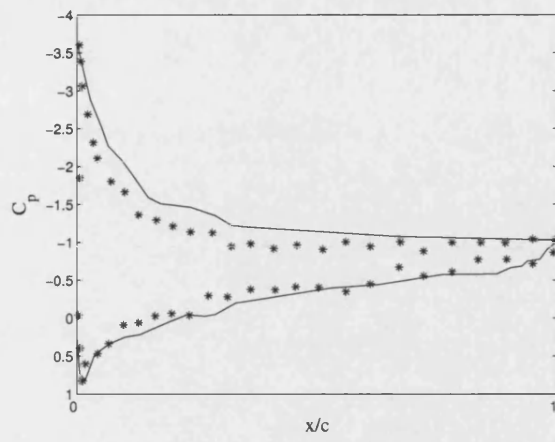


*a*:  $\eta = 0.033$ ;

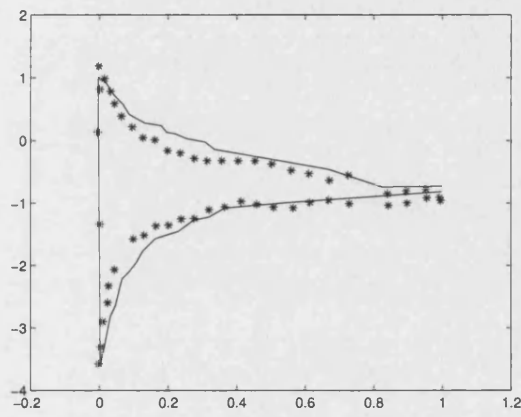


*c*:  $\eta = 0.472$ .

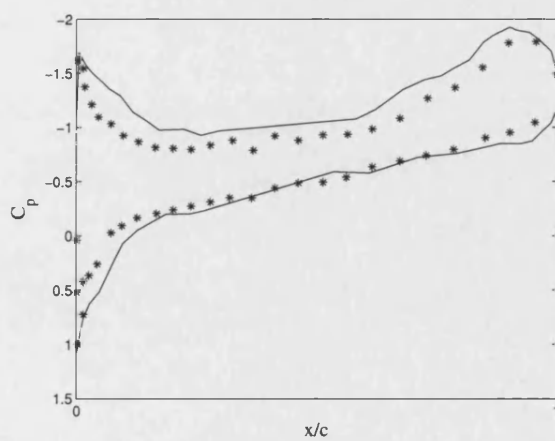
Figure 4.17: Pressure coefficient at  $M = 0.3$  and  $\alpha = 6^\circ$ . Solid line indicates computed and star symbols experimental results respectively.



*a*:  $\eta = 0.033$ ;

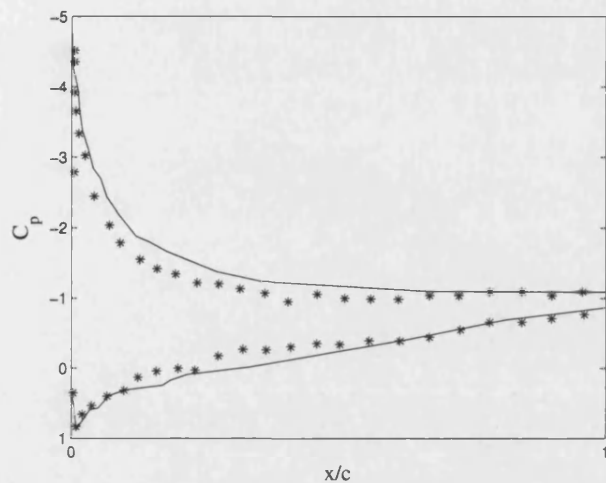


*b*:  $\eta = 0.472$ ;

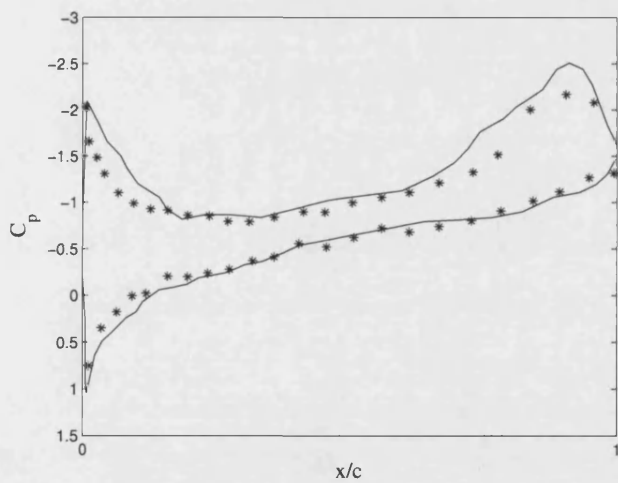


*c*:  $\eta = 0.988$ .

Figure 4.18: Pressure coefficient at  $M = 0.3$  and  $\alpha = 10^\circ$ . Solid line indicates computed and star symbols experimental results respectively.

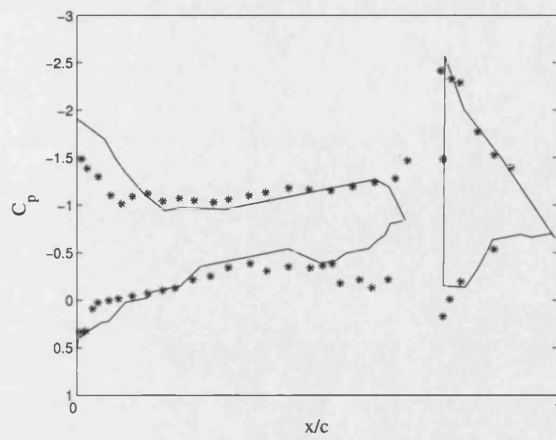


*a*:  $\eta = 0.033$ ;

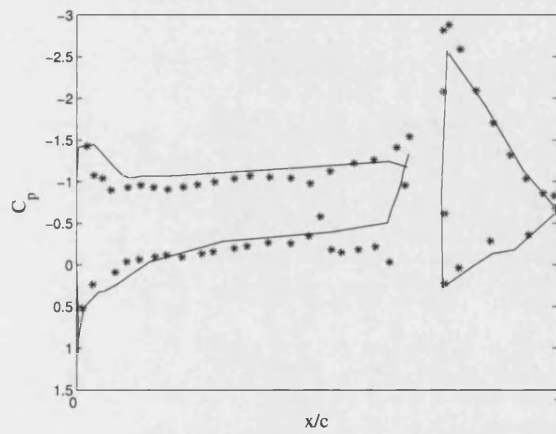


*c*:  $\eta = 0.988$ .

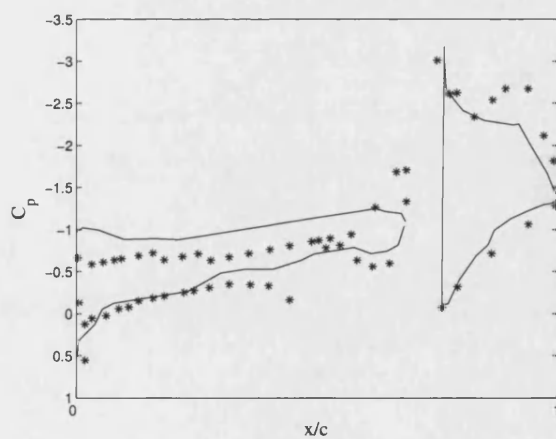
Figure 4.19: Pressure coefficient at  $M = 0.3$  and  $\alpha = 16^\circ$ . Solid line indicates computed and star symbols experimental results respectively.



a:  $\eta = 0.033$ ;

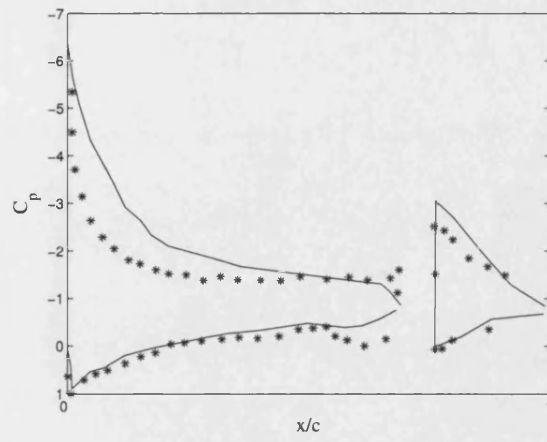


b:  $\eta = 0.472$ ;

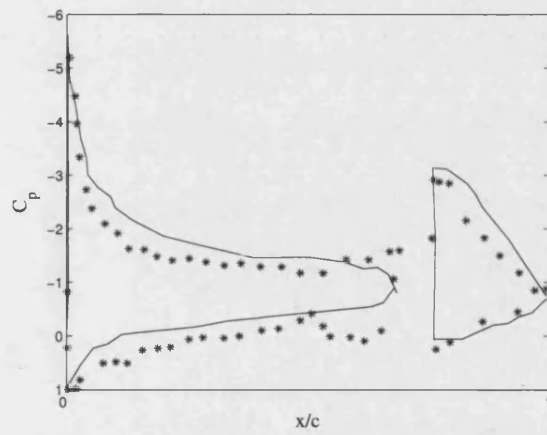


c:  $\eta = 0.988$ .

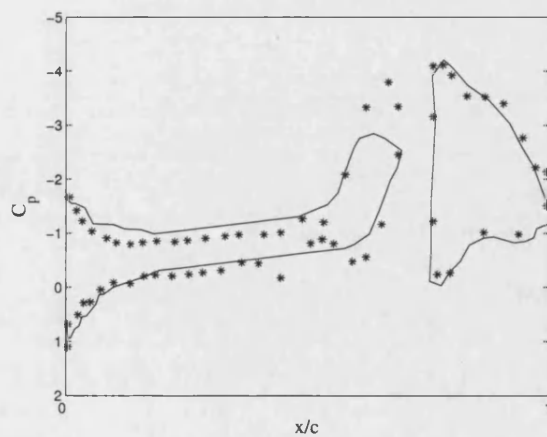
Figure 4.20: Pressure coefficient at  $M = 0.3$  and  $\alpha = 0^\circ$  with flap extended. Solid line indicates computed and star symbols experimental results respectively.



a:  $\eta = 0.033$ ;



b:  $\eta = 0.472$ ;



c:  $\eta = 0.988$ .

Figure 4.21: Pressure coefficient at  $M = 0.3$  and  $\alpha = 8^\circ$  with flap extended. Solid line indicates computed and star symbols experimental results respectively.

pressure field for two Mach numbers. It is clear that there is very good agreement between

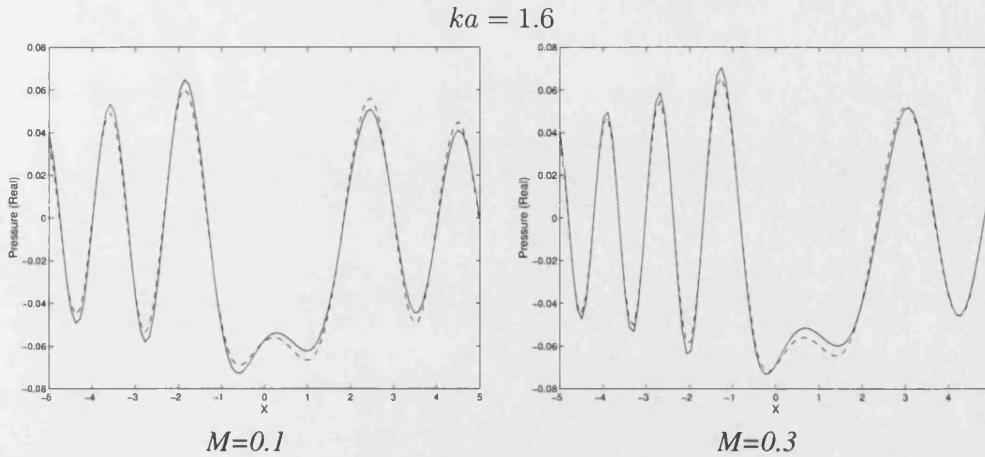


Figure 4.22: Unsteady pressure around a circle with a unit acoustic source; computed values shown solid, analytical values dashed.

computed and theoretical results. Figure 4.23 shows the error of the unsteady pressure for  $M = 0.3$  for different numbers of nodes on the circle.

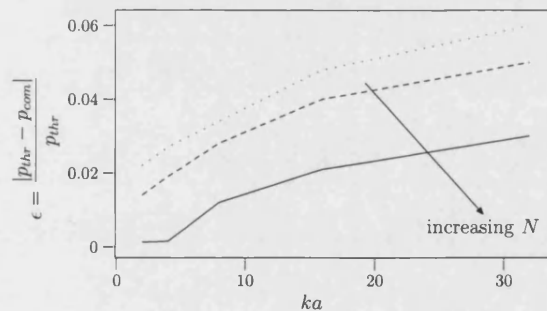


Figure 4.23: Error in unsteady pressure around a circle for  $N = 200$ ,  $N = 300$  and  $N = 400$ .

As a check for the range of Mach numbers for which the method is valid, another comparison was made using an analytical formula that describes potential flow around bodies. The Janzen-Rayleigh equation [29] gives the maximum velocity over elliptical sections in compressible flows:

$$v_{max} = 1 + \frac{e}{1 - \beta^2} + \frac{e^2 M^2 (1 - 0.4 M^2)}{2(1 - \beta^2)^4} + O(e^3), \tag{4.14}$$

where  $e$  is the thickness ratio. Figure 4.24 shows the geometry of an elliptical section. Figure 4.25 shows the error,  $\epsilon = (V_{max} - V_{com})/V_{max}$ , versus Mach number for 6 different

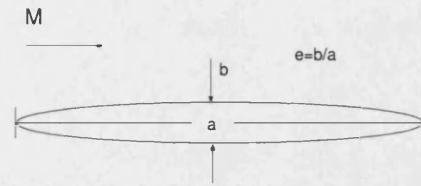


Figure 4.24: Geometrical characteristics of an elliptical section.

thickness ratios, where error is defined as the relative difference between the theoretical maximum ( $V_{max}$ ) and the computed maximum ( $V_{com}$ ) velocities. It can be seen from Figure 4.25 that the error increases with Mach number and with thickness ratio. Figure 4.26

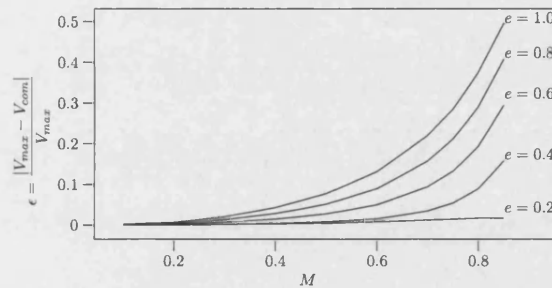


Figure 4.25: Error behaviour with Mach number for the maximum velocity over an elliptical section.

presents the range of Mach numbers and the corresponding thickness for a given error. As we observe, the higher the demands for a small error, the less the combinations between Mach numbers and thicknesses. This also implies that the method is more suitable and more efficient for slender bodies such as aerofoils.

To find out if the accuracy of the method improves as the number of nodes ( $N$ ) increases, we checked the error according to the analytical expression, for different numbers of elements. Figure 4.27 shows the error computed with the Janzen-Rayleigh formula versus the Mach number for four different numbers of elements. It is clearly illustrated that increasing the number of elements the accuracy increases as the error takes smaller values for higher  $N$ .

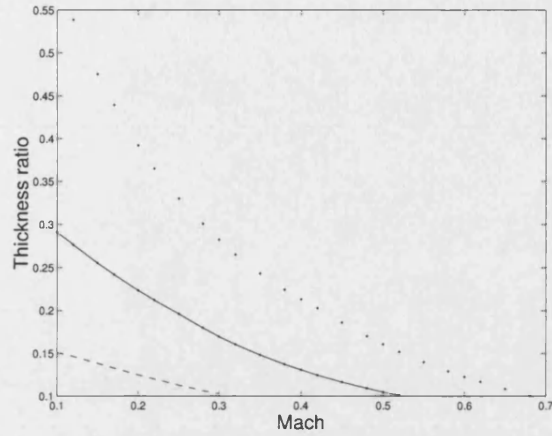


Figure 4.26: Thickness vs Mach number for a given error in the maximum velocity over an elliptical section; dashed line indicates error 0.01; dotted line, 0.1 and solid line, 0.05.

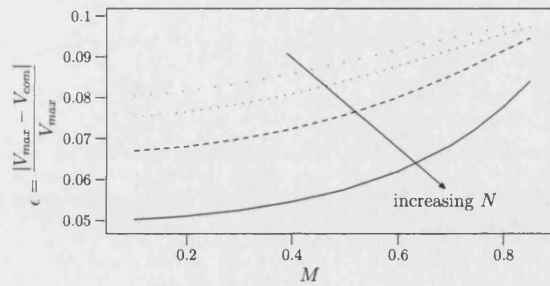


Figure 4.27: Error behaviour with Mach number for  $N = 100$ ,  $N = 200$ ,  $N = 300$  and  $N = 400$ .



# Chapter 5

## Parallelisation

Traditionally, programs have been written for serial computers which means that one instruction is executed at a time using one processor. There are several classes of problems that require a lot of calculations. These problems can be categorised as simulation and modelling problems and problems dependent on computation or manipulation of large amounts of data. A strategy for performing large, complex tasks faster and more efficiently led to the idea of parallelism. A large task can either be performed serially, one step following another, or can be decomposed into smaller tasks to be performed simultaneously, i.e., in parallel. Parallelism is performed by breaking up the task into smaller tasks assigning the smaller tasks to multiple workers to work on simultaneously and finally coordinating the workers. More specifically this is implemented by decomposing the algorithm or data into parts, distributing the parts as tasks which are worked on by multiple processors simultaneously and coordinating work and communications of those processors.

There are different ways of implementing parallelism based on shared or distributed memory type. Figures 5.1 and 5.2 show the configuration of each type.

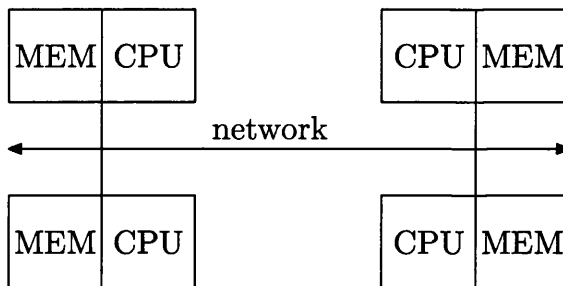


Figure 5.1: Distributed memory model.

The distributed memory system was adopted in the present work using a standard portable message-passing library definition called Message Passing Interface [4] (MPI). There are many advantages and disadvantages of using MPI. With MPI multiple processors operate independently but each has its own private memory and data are shared

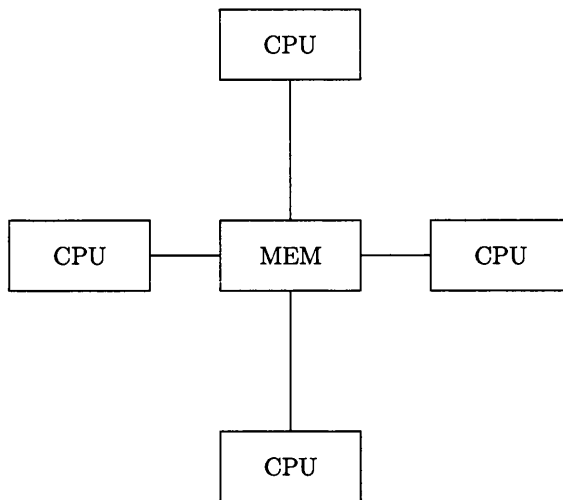


Figure 5.2: Shared memory model.

across a communications network using message passing, while at the same time a synchronisation option among the processors is available. Each processor can rapidly access its own memory without interference and without overhead. Consequently, increasing the number of processors, the size of memory increases proportionally. Programs using MPI run on any platform which has an MPI implementation without any need to modify the codes. The programs are independent of machine architecture and type of network employed to transfer data from one processor to another. Finally, many scientific libraries such as PETSc [78] and ScaLAPACK [79] employ MPI for message-passing communication supporting the easy computational implementation of this tool. This does not mean that there are no drawbacks in using MPI. The programmer is responsible for many of the details associated with data communication between processors and therefore is prone to errors. It may be difficult to map existing data structures, based on global memory, to this memory constitution. The shared memory model system is called OpenMP and is shown in Figure 5.2. It describes a computer architecture where all processors have direct access to common physical memory. In a programming sense, it describes a model where parallel tasks all have the same “picture” of memory and can directly address and access the same logical memory locations regardless of where the physical memory actually exists. We will not expand on this topic because it is beyond the scope of this work.

In acoustics problems the assembly procedure results in a matrix which is usually large as it contains information for both the real and the imaginary part of the left hand side of the boundary integral equation. This applies in particular in three dimensional applications where the number of elements used is high. This results in a large system with a square matrix which is time consuming to solve because of the size. The solution procedure was implemented using an iterative solver where a matrix multiplication is needed for every iteration to reach the solution. With an iterative solver matrix multiplication operations take place until the solution converges. The assembled matrix is split into parts

so each of the processors reads a part and does the corresponding multiplication. Eventually, after all the communication actions, one processor gathers the information from the others and carries out the rest of the work to achieve the solution.

### 5.1 Performance analysis

In parallel programming there are various criteria to measure the performance of the parallel program. The communication operations among the processors usually cost quite a lot of time depending on the type of the operation and the nature of the problem. This implies that there is the possibility that a parallel program can be less efficient than a serial program. Moreover, most of the time there are many different MPI commands that can lead to the same result. It is up to the programmer’s ability to choose the least expensive memory and time wise. There are many factors that we have to take into account before we assess a parallel program’s efficiency. Figure 5.3 shows what actually happens during the execution of a parallel program. As we can see there is a part of the serial program that cannot be parallelised and is executed by every processor in the parallel version.

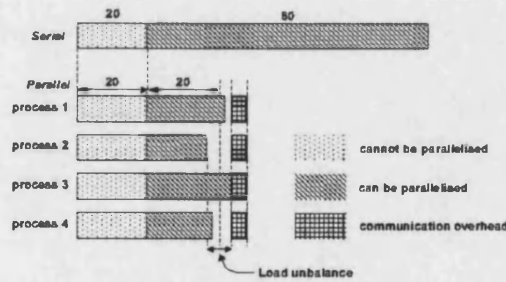


Figure 5.3: Balancing and overhead in a parallel program [4].

During parallel execution there are various phenomena that occur and affect the overall efficiency. Looking at the figure we can see the load imbalance and the communication overhead. Parallel tasks typically need to exchange data. There are several ways this can be accomplished, such as through a network, however the actual event of data exchange is commonly referred to as communication regardless of the method employed. So, we can see that the data transfer over the network is time consuming, and this is an additional overhead. Load balancing refers to the practice of distributing work among tasks so that all processors are kept busy all of the time. Load balancing is important to parallel programs for performance reasons. For example, if all tasks are subject to a barrier synchronisation point, the slowest task will determine the overall performance. To check the performance of a parallelisation we need an index to compare computation times. The following index is often used:

$$S(p) = \frac{T_1}{T_p}, \tag{5.1}$$

where  $T_p$  is the elapsed time for the program to execute with  $p$  processors. Note that in the above formula the elapsed time is not the elapsed time of the parallel program run on one processor. Even executed with one process, parallel programs have an overhead for initialising the environment, such as calculating the range for loop variables. In the ideal case,  $S(p) = p$ , but because the parallelised program has communication overhead and part of the program is not parallelised the speed-up is usually less than  $p$ . Another factor that should be taken into account is the specification of the hardware. For instance, consider two machines that have the same CPU but the network speed of one has half the speed. In such a case, the speed-up ratio also varies, even if you run the same serial and parallel programs. An additional way to measure the parallel performance is efficiency which is given by:

$$\eta(p) = \frac{S(p)}{p}. \quad (5.2)$$

Efficiency is actually a stricter criterion to check the parallel performance. There is an economic analogy, it is the speed-up over the number of processors. It is measuring the percentage of the beneficial work done by taking into account the the resources used or even better the processors used. The efficiency reveals the actual work produced in a more general way to evaluate the parallel performance.

## 5.2 Parallel calculations

The parallel implementation was applied to the resulting matrix system of the 3-D code for an aeroplane wing. The number of nodes on the surface of the wing is  $n$ , so the final matrix after the assemble procedure will be of size  $2n \times 2n$ .

The linear system to be solved is of form  $Ax = b$  where  $A$  is the square matrix,  $x$  the unknown vector and  $b$  the known vector. The matrix  $A$  is split into a number of parts depending on the number of the processors. More specifically, if the number of elements of matrix  $A$  is  $n_{elems}$  and the number of processors used is  $p$  then each processor allocates memory for a matrix of size  $n_{rows} \times n_{elems}$  where  $n_{rows}$  is the number of rows selected. Furthermore, each processor allocates memory for vector  $b$  in order to be able to do the multiplication between its part of  $A$  and  $b$ . There is a synchronisation command which stops the next task starting before all the processors have done the multiplication. Then each processor sends the part of  $b$  to the others and from that point a single processor takes over the rest of the work to be done. The parallel code was developed in the University of Bath and it is in a extended to include a wide range of iterative methods.

We run the parallel code for a scattering problem for three different geometries on an IBM Linux cluster [80]. Figures 5.4, 5.5 and 5.6 show the speed up and efficiency for a duct, a wing and a sphere respectively. The first comment we could make observing the figures is that the smallest in size problem shows a rapid and satisfactory speed-up but its efficiency drops very quickly and to very low values. Larger problems seem to behave better as they show a steadier speed-up which keeps the efficiency at higher levels. A very good explanation for this behaviour would be that in problems with smaller size the parallel run time becomes much smaller compared to the overall time. Especially when

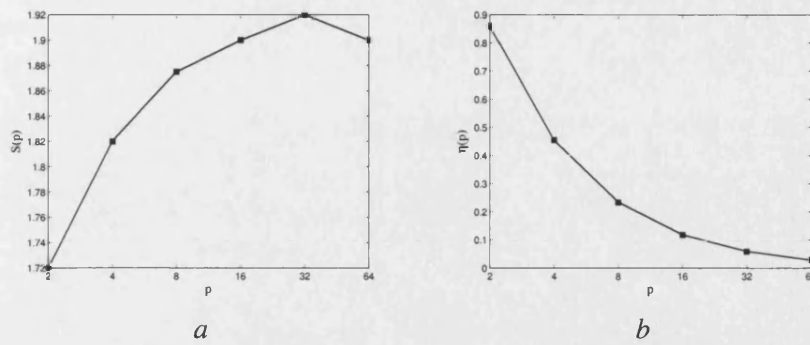


Figure 5.4: Performance graphs for a sphere with an acoustic source of:  $M = 0.1$ ,  $ka = 1$ ,  $N = 4560$ :  $a$ : speed up;  $b$ : efficiency.

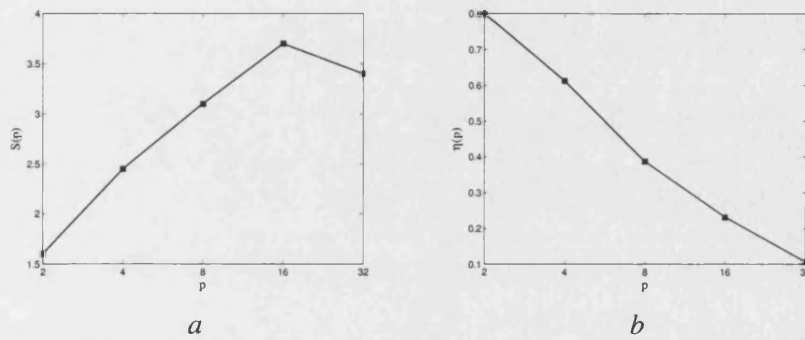


Figure 5.5: Performance graphs for a duct with an acoustic source of  $ka = 1$ ,  $N = 8200$  nearby,  $a$ : speed up;  $b$ : efficiency.

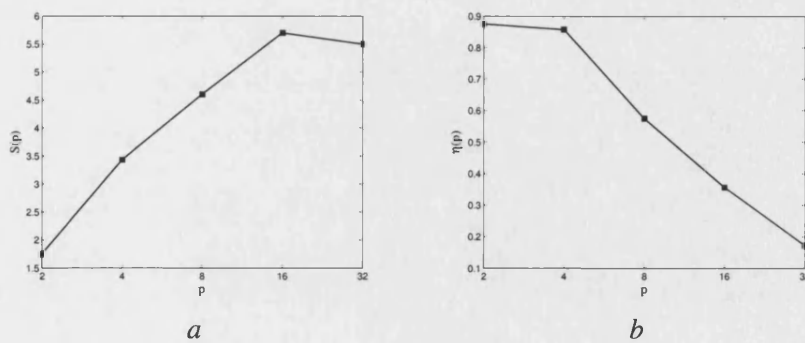


Figure 5.6: Performance graphs for a wing with an acoustic source of  $M = 0.1$ ,  $ka = 1$ ,  $N = 11016$  nearby,  $a$ : speed up;  $b$ : efficiency.

many processors are used to solve a small system the communication overhead is getting bigger and comparable to the run time. Furthermore, it looks as if the performance for bigger problems remains at higher numbers before it drops, compared to smaller problems where it falls even lower. In general looking at the performance figures we see the typical and usual features of such kind of plots. The speed-up graph rises up to a certain number of processors and then it breaks down. These characteristics are easily explained if we think that a certain percentage of the code is parallelised and the communication overhead and the load imbalance cannot be avoided. In spite of the fact that we tried to eliminate the load imbalance as much as we could using an even distribution of the data among the processors, the communication delays and technical difficulties will always limit the performance.

# Chapter 6

## Results

In this chapter we present the results from the application of the numerical method developed in the previous chapters. The results include two and three dimensional problems of an aerofoil and a wing respectively. Moreover, we examine the case of a wing with high lift devices in flow and at incidence. The results are contour plots of the sound field. A large number of figures are displayed in the Appendix presenting the sound pressure around a wing and an aerofoil for different flow Mach numbers and angles of attack. Here are shown some representative pictures that summarise the basic features that appear in the acoustic radiation. Apart from the lifting body scattering results we present some sound pressure directivities for a scarfed and a non scarfed duct without mean flow. We show the acoustic pressure for a duct with a fan, where the fan is simulated with a series of sources in a ring shape.

### 6.1 Sound field around a duct

Figure 6.1 shows the coordinate system that is used, centered on the centre of the duct. The ring is located in the middle of the duct horizontal axis. The ring source has radius

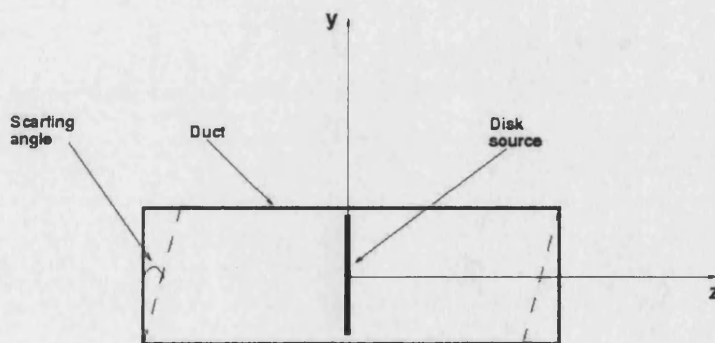


Figure 6.1: Duct and scarfed duct geometry.

$a = 0.5m$ , while the inner duct radius  $r = 0.7m$ . The duct generator is an ellipse with horizontal dimension of  $4a$  as shown in Figure 6.2.

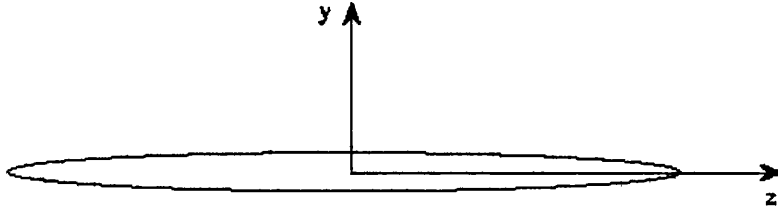


Figure 6.2: Elliptical section of the duct generator.

Figure 6.3 illustrates the pressure contour plots around the duct for three different scarfing angles. Having a look at the figure we can see how the sound is scattered from inside the duct to the field and notice the difference between scarfed and unscarfed ducts. As we can observe the radiation symmetry is destroyed when a scarfing configuration is considered and at the same time the pressure magnitude changes depending on the angle.

The sound pressure directivities that are presented in the following figures are plotted according to the coordinate system shown in Figure 6.1. The azimuthal order  $m = 6$  and the scarfing angle is indicated in Figure 6.1 with the dashed line. Three tip Mach numbers were chosen, 0.9, 0.95 and 1.1, and three scarfing angles  $\pi/9$ ,  $\pi/12$  and  $\pi/18$ . The resulting acoustic directivities are shown in Figures 6.4–6.6. In each case, the magnitude of the radiated pressure is plotted against  $\phi$  at fixed  $R$ . In each polar plot, the red line is for  $R = 64$ , while the blue line is for  $R = 8$ . The pressures have been scaled on their maximum value at each value of  $R$  and the maximum value of the pressure is shown with the corresponding colour. We move the disk source towards one end of the duct to calculate the sound pressure field when the fan is close to the inlet of the engine. The noise directivity figures are all drawn under these geometrical conditions.

Figure 6.4 shows the directivities of the noise for  $M_t = 0.95$  for the three different scarfing angles. In this case, one radial mode (modes were explained in section 3.5) is cut on and the second one is just cut off. It can be seen from Figure 6.4a that there is some radiation ( $R = 8$ ) with a strong lobe at the intake and a weaker lobe at the exhaust. This happens because the mode propagates (cut on), so it reaches the exhaust and radiates. The intake lobe is strongest because the ring is located at the inlet. In Figure 6.4b with a scarfing angle of  $\pi/18$ , there seems to be a single strong lobe with scaled value almost three times greater than that of the case of the unscarfed duct. As we can see here, the whole image has completely changed in both the near field and the far field. The scarfing angle has forced the lobe to move in only one direction. The pressure is three times greater and the lobe looks to be wider. In Figures 6.4c and 6.4d the scarfing angles are  $\pi/12$  and  $\pi/9$  respectively. As we can observe, as the scarfing angle becomes larger, the radiation field becomes wider, while the acoustic pressure finds more ways to exhaust.



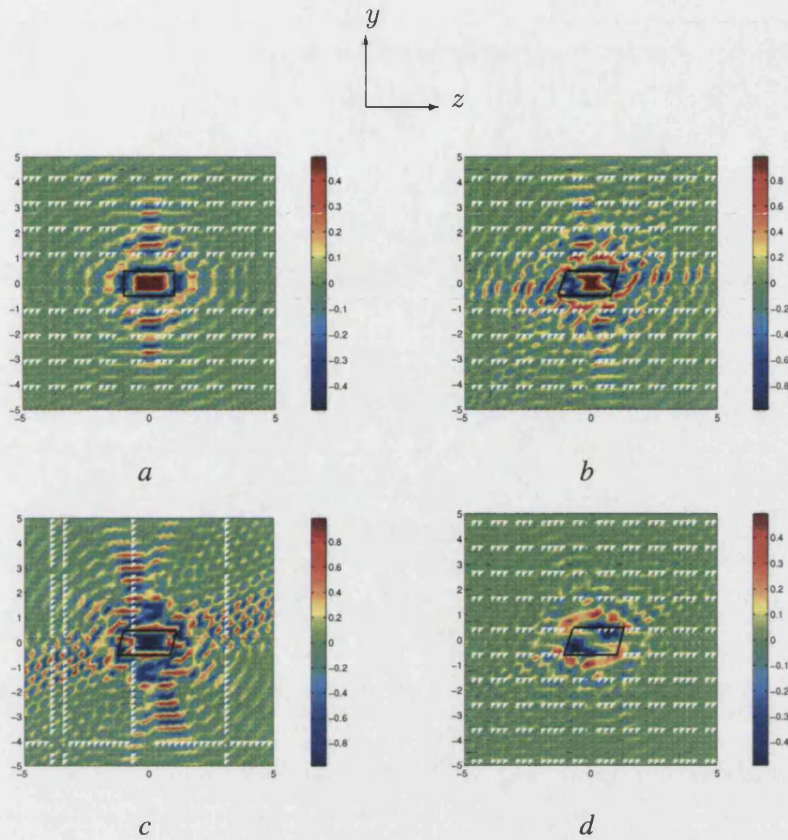


Figure 6.3: Color contour pressure plots around the duct, *a*: scarfing angle = 0 ; *b*: scarfing angle =  $\pi/18$  ; *c*: scarfing angle =  $\pi/12$  ; *d*: scarfing angle =  $\pi/6$ .

In Figure 6.5 where the Mach number is 1.1, two modes are propagating in the duct. It can be seen from Figure 6.5 that in the case of a simple duct the pressure field remains symmetric and the acoustic pressure forms a strong lobe because the modes are well cut on. In the far field ( $R = 64$ ) we have an identical image of the acoustic pressure, as the only thing that changes is the magnitude of the pressure, which is small compared to the near field radiation. Furthermore, it is important to note that scarfing, in this case, is not very effective. Figure 6.5 demonstrates that scarfing ‘scatters’ the pressure field around the duct in different directions and creates a non-uniform image.

Finally, in Figure 6.6 we focus our attention on the effect of scarfing below the horizontal. The Mach number is 0.9 and one mode is just cut on. As one mode propagates, we have exactly the same features appear as in Figure 6.5. Taking a careful look at these figures we can observe that unlike in Figure 6.5 where two modes propagate, in Figure 6.6 the scarfing does not cause a non-uniform field. The reason for this behaviour is that there are no other modes to propagate so as to interact with each other.

In Figures 6.4 and 6.6 we can see that for higher Mach numbers the acoustic pressure is much larger compared to that of smaller Mach numbers. This happens because the

modes that are to propagate depend on the azimuthal order  $m$ , which is associated with the number of blades, and the duct radius. An interesting point comparing Figure 6.5d with Figure 6.6d, is that for well propagating modes, scarfing is more effective as the scarfing angle gets larger. When increasing the scarfing angle, there seems to be formed a wider but weaker single lobe in comparison with the lobes at smaller scarfing angles. Finally, a scarfing angle of  $\pi/18$  to  $\pi/12$  causes an unusual radiated field where there is just one dominant lobe which is formed below the horizontal (Figure 6.4).

To conclude, it is worth drawing some basic ideas and observations on the effect of scarfing. Considering a duct, the radiated pressure is intensified below the horizontal, but at the same time it is strongly attenuated above the horizontal. As can be seen, we have chosen three very crucial Mach numbers for the fan tip velocity. Two of them are below supersonic and the other is above. All of them are feasible and exist when a fan operates. Looking carefully at the figures we can see that as the Mach number increases the acoustic pressure is larger. We can observe in the figures that in an unscarfed duct the acoustic pressure is getting larger and larger as the Mach number increases. On the other hand, the effect of scarfing does not reduce the acoustic pressure levels but it effectively change its direction. Scarfing breaks the symmetry of the sound radiation and can be effective when certain modes propagate. We have to point out that the last statement is of great importance if we think that in realistic conditions and especially during take-off, the fan blades speed reach supersonic speed.

## 6.2 Radiation field around a wing

In the following pages are displayed a number of three dimensional results. We plot the real part of the acoustic pressure around a NACA 2412 wing and a wing with high lift devices extended. This wing is a spanwise extension of 4 chords length of an aerofoil geometry provided by Trinity College Dublin as part of the European project ROSAS. A unit acoustic source is placed above the wing and it is indicated with a black circle in the pressure plots. We examine the field spanwise plotting the field on the  $x$ - $y$  plane at different  $z$  locations. Figure 6.7 shows the axis system and the planes. We chose low, mid and high Mach numbers and moderate and high frequencies to cover take off and cruise conditions. The source was placed at a specific point because there was interest in the role of flow in acoustic radiation and its shielding effect when the engine is located above the wing. This particular area of investigation arises from the ROSAS project. Figure 6.8 presents an overall image of the sound radiation around the three dimensional body. We can see the sound waves and their direction propagating from the source. The  $x$ - $z$ ,  $z$ - $y$  and  $x$ - $y$  planes show the sound pressure in front of, above and underneath the wing with high lift devices. The same features are shown in Figure 6.9 for a simple wing. Observing the contours we can see the less uniform field due to the presence of the flaps and slats. The upper ( $y = 0.5m$ ) and the lower ( $y = -0.5m$ ) planes of the wing show that the field above the wing is much stronger compared to that underneath. This is because the source is located above the wing. Another interesting feature rises looking at the front plane  $y$ - $z$  results where we can see the symmetrical radiation (even though the plot is not

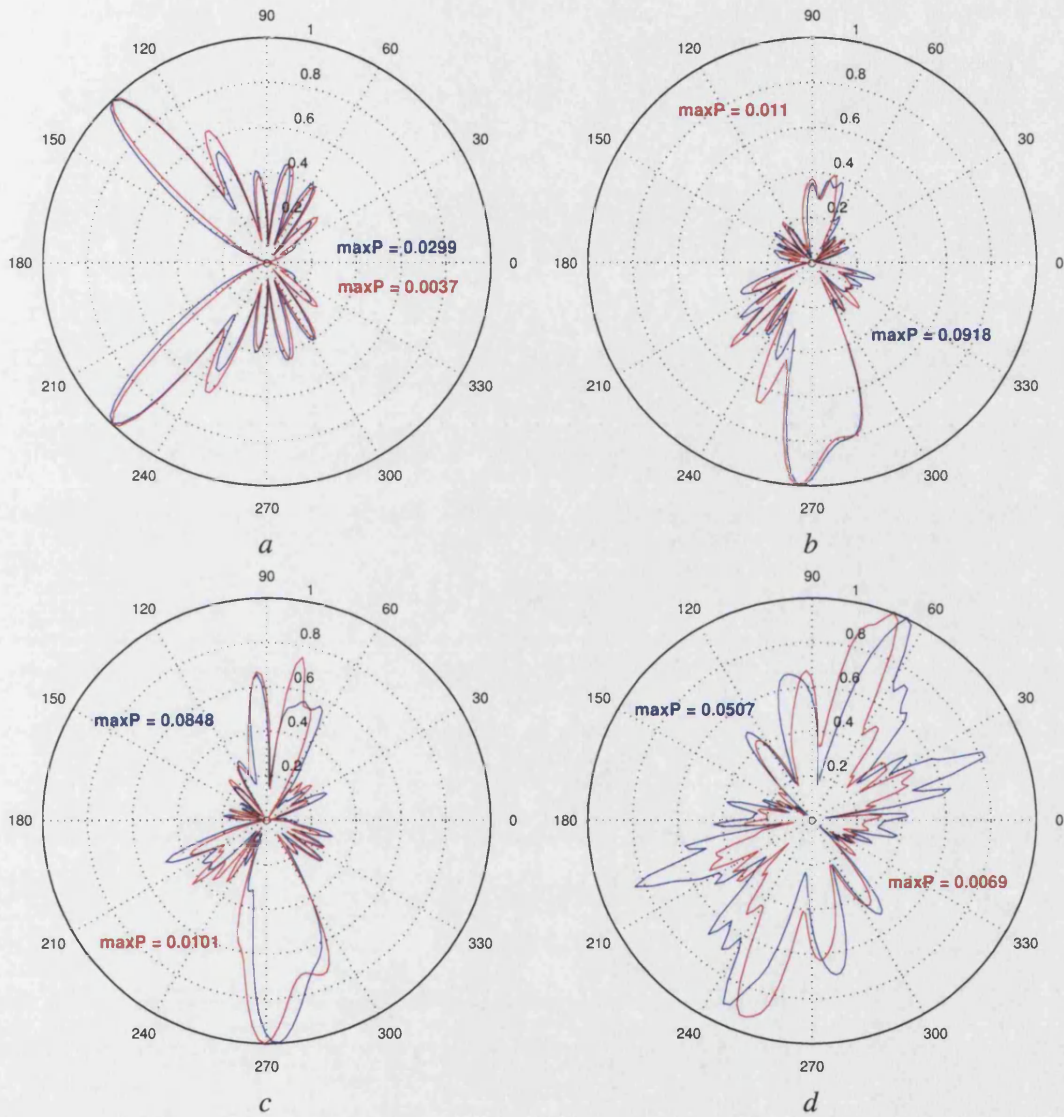


Figure 6.4: Ducted fan noise directivities,  $M_t = 0.95$ , *a*: scarving angle =  $0$  ; *b*: scarving angle =  $\pi/18$  ; *c*: scarving angle =  $\pi/12$  ; *d*: scarving angle =  $\pi/9$ .

Blue line indicates  $R = 8$  and red line indicates  $R = 64$ .



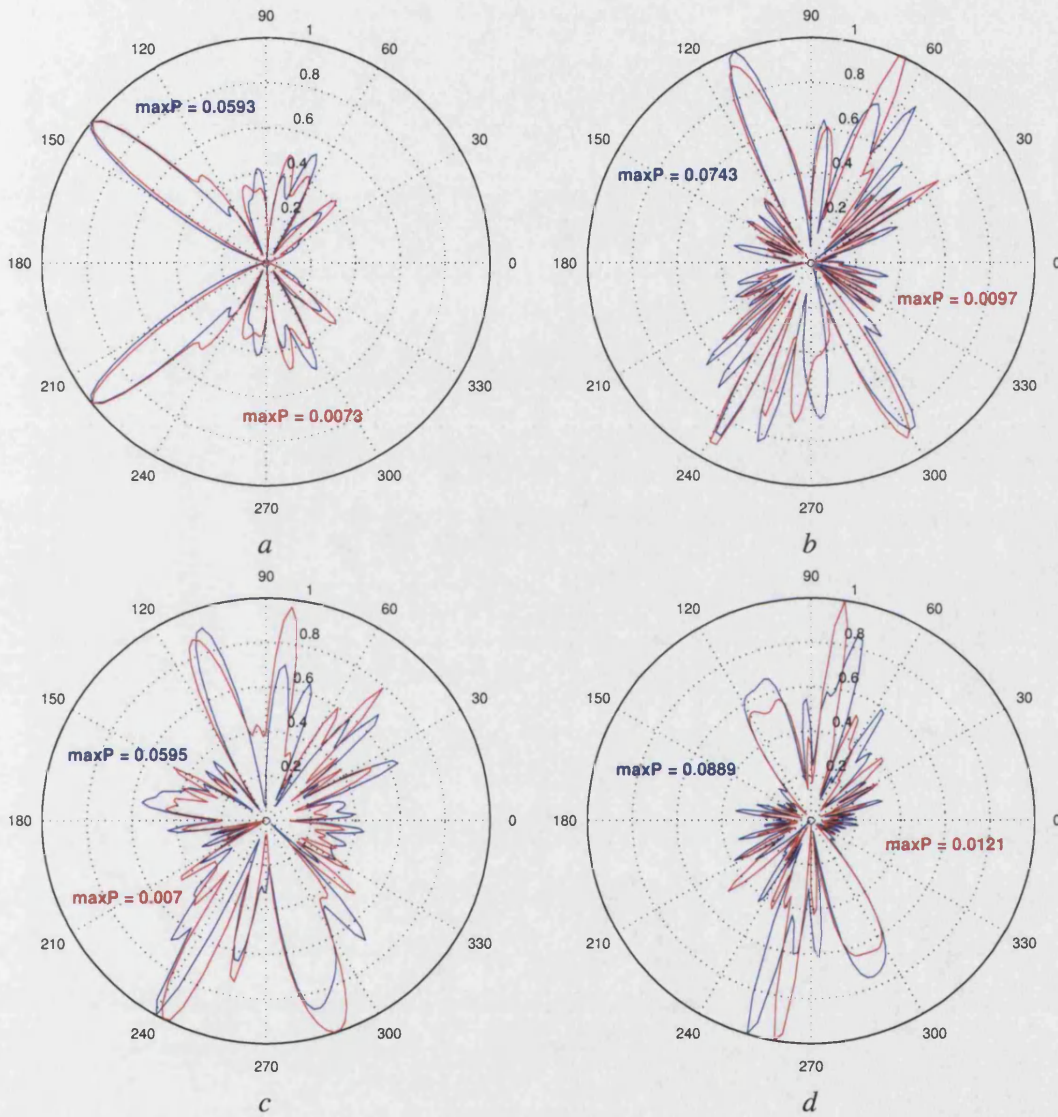


Figure 6.5: Ducted fan noise directivities,  $M_t = 1.1$ , *a*: scarfig angle =  $0$  ; *b*: scarfig angle =  $\pi/18$  ; *c*: scarfig angle =  $\pi/12$  ; *d*: scarfig angle =  $\pi/9$ .

Blue line indicates  $R = 8$  and red line indicates  $R = 64$ .

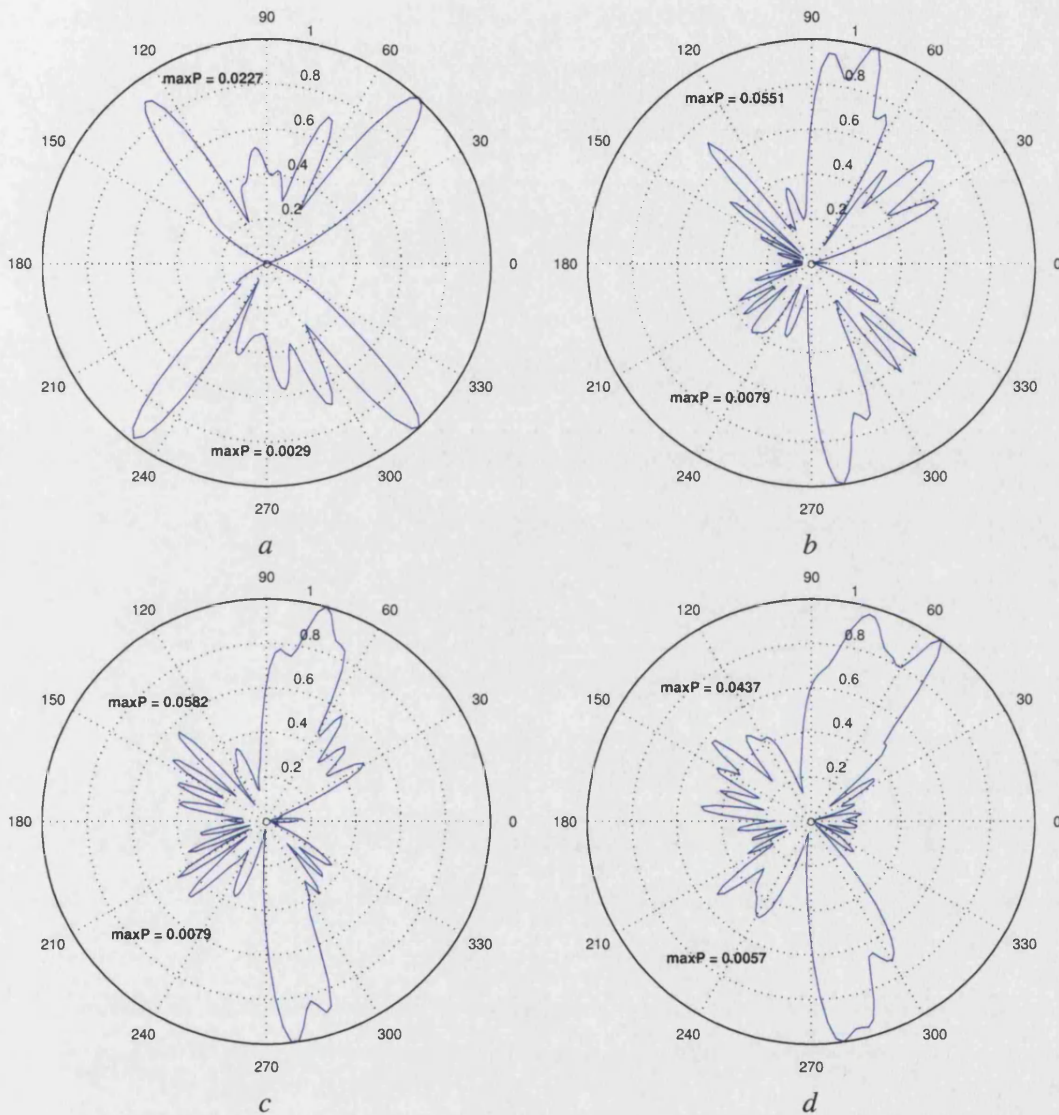


Figure 6.6: Ducted fan noise directivities,  $M_t = 0.9$ ,  $a$ : scarfing angle = 0 ;  $b$ : scarfing angle =  $\pi/18$  ;  $c$ : scarfing angle =  $\pi/12$  ;  $d$ : scarfing angle =  $\pi/9$ .

Upper plot indicates  $R = 8$  and lower plot indicates  $R = 64$ .

symmetric) on both sides of the wing as the source is in the middle of the wing.

Observing figures A.4, A.7 and A.10 for low Mach numbers ( $M = 0.1$ ) we can see that the sound around the wing is stronger above the wing and at the same side of the source and less intense underneath. This is easily explained as the wing body acts as a protective layer that prevents the sound from travelling further down. Still though we can see sound pressure underneath the wing which is mostly due to the incident field. Having a look at figures A.3, A.6 and A.9 for mid Mach numbers ( $M = 0.3$ ) we see no great surprise on the sound radiation pattern. It follows the same pattern as at low Mach number but especially at higher frequencies we can notice a slight effect of flow “stretching” the field in the streamwise direction. Moving to the high Mach numbers we can observe some very interesting results as there is a strong impact of the flow velocity on the sound waves.

The field takes a bizarre form where the acoustic pressure is very strong at the front of the wing. This phenomenon is called Doppler shifting and means that the sound radiated in the forward direction ahead of the source is amplified by the motion whereas the sound propagating at the rear is attenuated. This involves a streamwise directional change of the wavelength, where the new wavelength is multiplied by a factor. The Doppler shifting is more noticeable at higher Mach numbers and this is because its strength depends on the Mach number. Furthermore looking spanwise we can see that the field is much stronger in the middle of the wing ( $z/b = 0.5$ ) compared to the tip ( $z/b = 0.1$ ). This is easily explained if we think that source is located in the middle of the wing. Another characteristic that should be noted is the wake effect. It seems that for low Mach numbers the wake does not play a very important role in the sound radiation. When the Mach number increases, the picture at the area near the trailing edge changes, taking a radiation pattern that distracts the uniform and homogenous existing one for a lower Mach number. Commenting on the plots with an angle of attack we can say that there is a diversion of the sound field in the direction of the angle of attack. There is a rotation that follows the rotation of the wing.

Looking at figures A.5, A.6 and A.7, when the high lift devices are extended, we notice a few more features that occur because of the flaps and slats. The pressure field shows a less uniformly distributed image especially at higher frequencies compared to the corresponding one with the wing. This is due to the fact that this case contains sharp edges and slots. The high lift devices contain corners which cause the sound waves to change their direction and follow alternative routes. Moreover the gaps between the flap and the slat with the wing body allow sound to get through and strengthen the field underneath the wing. That is the reason why we can notice a stronger radiation field underneath the wing compared to the one without the high lift devices. An additional point that should be mentioned is that the high lift devices change the direction of noise distribution and this explains why the pressure field is rotated when the wing is at a certain incidence. Another feature that is dominant when the high lift devices are extended is the wake behaviour. As we have already mentioned, the wake is treated as a line extending from the trailing edge to approximately three chord lengths downstream. Because the flap is at an angle of attack this makes the role of the wake more noticeable in the radiation field.



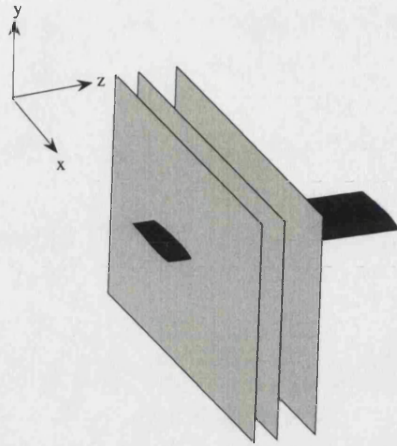


Figure 6.7: The wing and the positions of the result planes.

### 6.3 Radiation field around an aerofoil

The following figures show the noise field for a point source radiating into a mean flow in the presence of an aerofoil and an aerofoil with high-lift devices fitted. The geometry of the aerofoil with the high lift devices was provided by Trinity College Dublin as part of the European project ROSAS and it is shown in Figure 6.10.

The characteristic length  $a$  is the aerofoil chord and in this case,  $a = 0.4\text{m}$ . From Figure 6.11 we can observe the shielding effect of flow on the sound radiation especially at higher Mach numbers. We can also see the effect of flow which stretches the radiation field in its direction and shows how important flow can be. In compressible flow the effect is much more obvious as the Prandtl-Glauert factor  $\beta = (1 - M^2)^{1/2}$  which is involved in the pressure expression, decreases with Mach number. This results in a change of the streamwise component of the wave number and causes the sound field to be stronger for an observer standing in the front of the aerofoil than for another standing at the rear. The figures show that the high lift devices act like a protective layer where sound waves are reflected and change direction. Another important feature that becomes apparent is the trailing edge scattering effect which becomes more important if we think the trailing edge of the studied aerofoil is a sharp wedge. A sharp edge is a scatterer itself and influences the radiation field at the rear of the aerofoil.

Furthermore we can easily notice scattering behaviour of the sharp edge as well as the resulting pressure when two sharp edges are involved. This last fact applies to the aerofoil with high lift devices where the flap and the aerofoil end in a corner. Checking the results for higher Mach numbers and with high lift devices extended, it becomes clear that the wake has an impact on the sound scattering, as it seems that the latter is not uniformly distributed across the wake. The discontinuity of pressure as well as the

$$M = 0.3, ka = 65, \alpha = 10^\circ$$

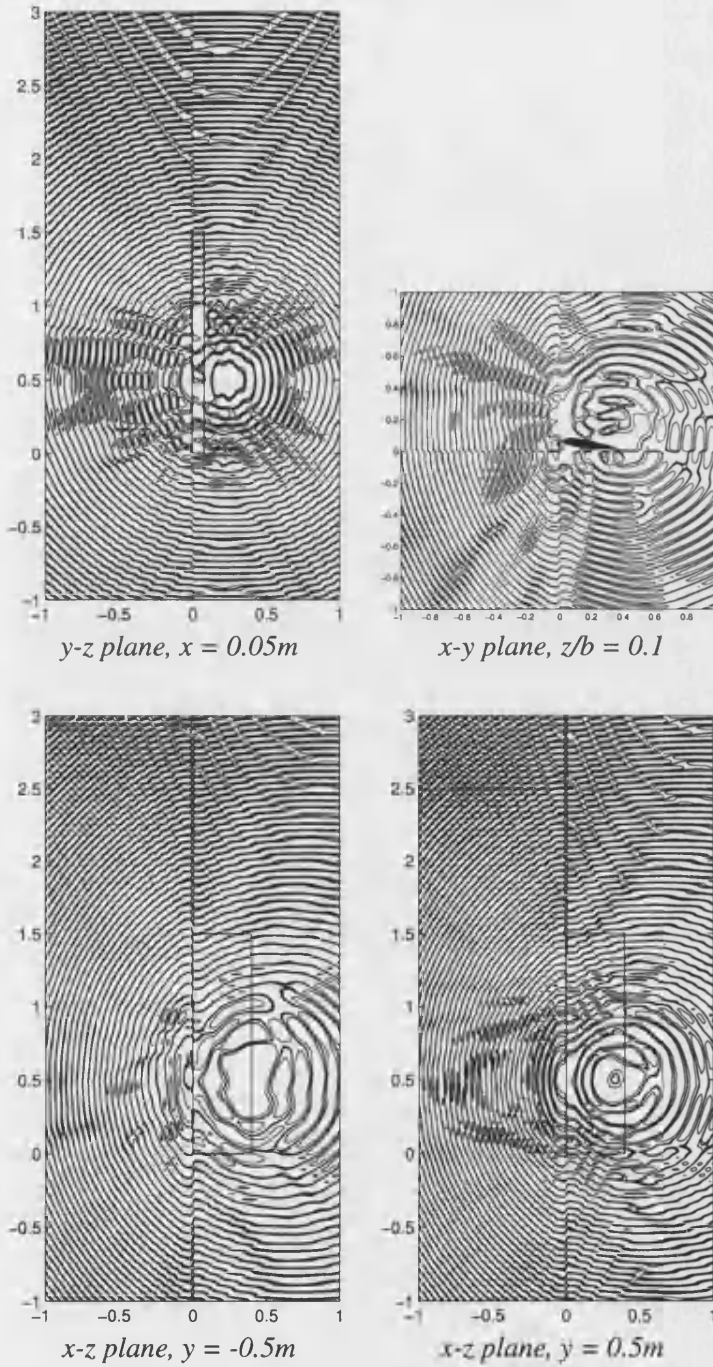


Figure 6.8: Total acoustic pressure (real part) around a wing with high lift devices and a unit acoustic source; contour levels  $\pm 10^{-1}$ ,  $\pm 10^{-2}$ ,  $\pm 10^{-3}$ ; positive values shown solid, negative values dashed.



$$M = 0.3, ka = 65, \alpha = 10^\circ$$

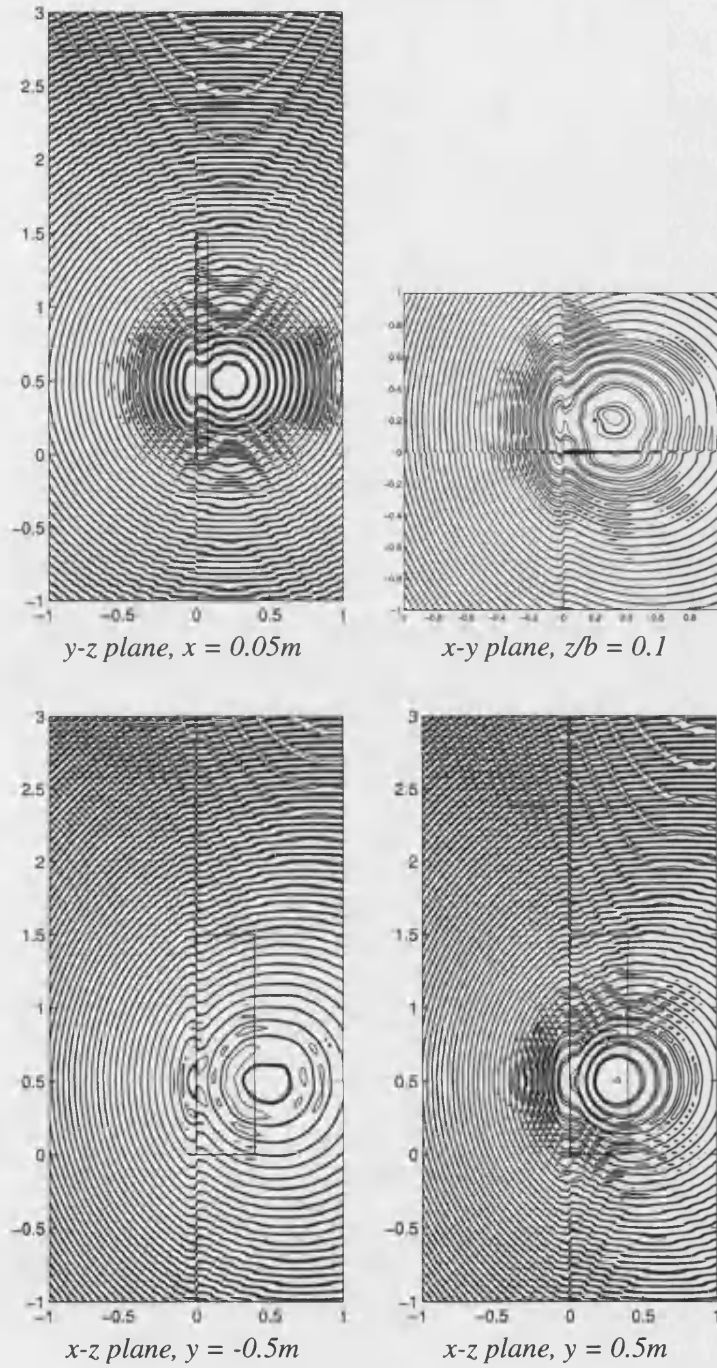


Figure 6.9: Total acoustic pressure (real part) around a NACA2412 and a unit acoustic source; contour levels  $\pm 10^{-1}, \pm 10^{-2}, \pm 10^{-3}$ ; positive values shown solid, negative values dashed.



Figure 6.10: Aerofoil geometry with the high lift devices extended.

unsettled radiation pattern at the back of the trailing edge are two of the characteristics of how the wake influences the noise field. This happens especially in the case where the high lift devices are fitted and the wake strength increases due to the incidence of the flap.

In general, we could say that the wake effect increases with Mach number and it seems to have a noticeable effect on the scattered acoustic pressure. Observing figures for high frequencies, we can form an idea of what is happening at very high frequencies and at mid angles of attack. The effect of the flow is dominating and the incidence causes a proportional re-direction of the radiated field. Even though the wake strength is quite large, the wake does not seem to have much impact on the radiated sound field. Figure 6.11 is a very representative figure of what happens at high frequencies and mid angles of attack. The field appears to be separated into two domains with a difference between the wavelengths. The flow Mach number wipes the acoustics waves and moves them towards its direction so, eventually, they counteract with each other.

### Note on discontinuities

The discontinuity, (for example see Fig 6.11), which appears as a vertical and horizontal line through the origin, does not represent any physical phenomenon. Instead, it is an effect caused by the post processing software (Matlab) when the point  $(0, 0)$  is included in the calculations. The problem can be alleviated by increasing the resolution of the mesh where the properties are calculated.

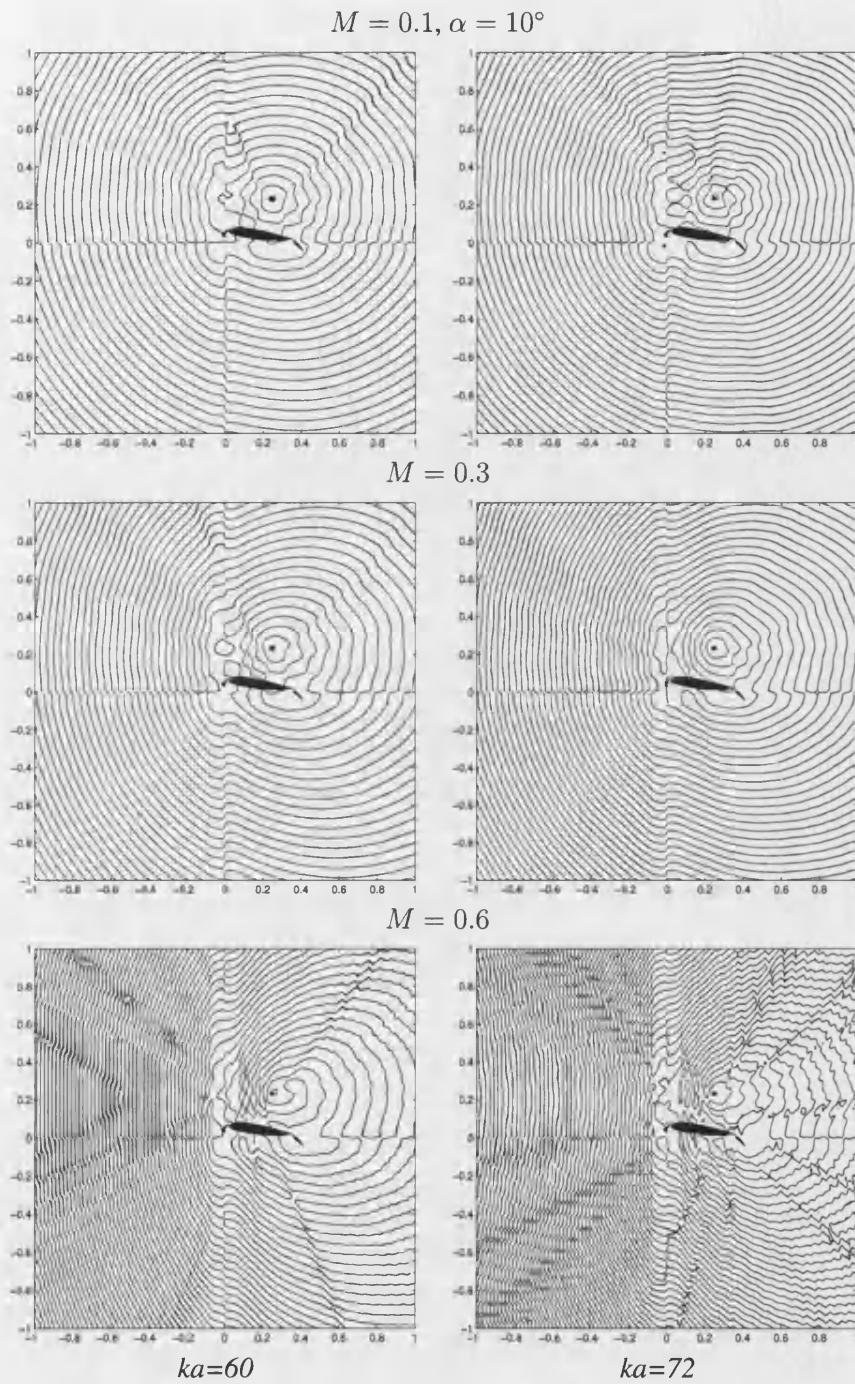


Figure 6.11: Total acoustic pressure (real part) around the aerofoil with high lift devices and a unit acoustic source; contour levels  $\pm 10^{-1}, \pm 10^{-2}, \pm 10^{-3}$ ; positive values shown solid, negative values dashed.

# Chapter 7

## Conclusions

Aeroacoustics is a growing area and has received significant emphasis due to advances in air, ground and space transport. More specifically, it has become increasingly important to address all the noise issues that are associated with aspects of civil and military aircraft and high speed train aeroacoustics, and the impact of acoustics on structures. The increased use of fluid machines and engines has led to an increasing level of noise generation, and hence to an increasing interest in this area of research. Noise generated by aeronautic systems or their components, sonic-boom created by high-speed flight, blade-vortex interaction (helicopters), turbulence-related noise in inlet flows (fans, compressors), noise from turbulent wakes and shear flows, noise from internal combustion engines are some of the most important areas to be investigated. All these phenomena are part of the aeroacoustics subject which is developing more and more to reduce community and cabin noise from subsonic aircraft and to minimize the noise impact of advances in transportation.

It has become increasingly important to address all of the above noise issues and new research needs to be conducted and effectively applied, in order to meet higher levels of noise certification and to make our world more environmentally healthy.

A lot of scientific research has been done in the area of aeroacoustics which includes both experimental and computational approaches. Our contribution to this wide field is restricted to the sound radiation from moving sources in non-uniform compressible and incompressible flow. We have investigated the unsteady phenomena that appear during the noise propagation especially from lifting bodies. We followed a particular BIEM already established and primarily used for aerodynamic purposes [12] and recently used for aeroacoustics of rotors [10]. The idea is to solve a noise scattering problem in non-uniform flows with an integrated aerodynamic/aeroacoustic approach. The basic concept is to calculate the aerodynamic and the aeroacoustic velocity potential and then apply the Bernoulli's equation in potential flow. This is a coupled approach which provides the convenience of calculating separately the aerodynamic and the acoustic field and then combining them.

The problems we dealt with were scattering around wings and aerofoils. Placing the acoustic source above the lifting body and for different frequencies and flow Mach numbers we monitor the acoustic field pattern. The Doppler shifting dominates and is

quite noticeable because of the flow. It becomes much more apparent at higher Mach number where the Doppler factor is amplified. A very interesting feature is the shielding effect of both the flow and the lifting surface. The flow plays a stretching role which pushes the acoustic waves backwards following the mean flow direction. At the same time the protective character of the wing is very clear when compared to the upper and lower areas of the lifting body. In three dimensions this feature is more noticeable than in two dimensions. Observing both the two and three dimensional sound pressure distributions it seems that the wake does not have a strong effect on the sound scattering.

A future plan would be to apply the method to large scale geometries (aeroplane) which it would handle relatively easily as the parallelization would speed up such a big problem. Uniform and non-uniform flow in a duct is another expansion of the method that has great potential to be completed. Moreover, duct acoustic treatment (liners) is also a very interesting application that could be implemented in the future. Expansion of the method to viscous flows to simulate the aerodynamic field is an idea that needs further development in the near future.

Concluding, we believe that we have added a very small stone to the pyramid of knowledge and that this will become the initiative or the starting point for another researcher to expand and to improve the current work in the future.

# Bibliography

- [1] <http://www.dfrc.nasa.gov/Gallery/Photo/>. accessed on December 2005.
- [2] M. Carley. The sound field of a rotor in a stationary duct. *Journal of Sound and Vibration*, 259(5):1067–1079, 2002.
- [3] Zachary T. Applin. Pressure distributions from subsonic tests of a NACA 0012 semispan wing model. Technical report, NASA, Langley Research Center, Hampton, Virginia, 1995.
- [4] Yukiya Aoyama and Jun Nakano. Practical MPI Programming. International Technical Support Organization, 2000.
- [5] <http://www.parliament.uk/post>. Aircraft noise. accessed on November 2005.
- [6] V. M. Kuznetsov. Noise control problems of passenger airplanes. *Acoustical Physics*, 49(3):241–262, May 2002.
- [7] Antonio Filippone. Data and performances of selected aircraft and rotorcraft. *Progress in Aerospace Sciences*, 36:629–654, 2000.
- [8] H. H. Hubbard. Aeroacoustics of flight vehicles. *Acoustical Society of America*, 1st, 1995.
- [9] M. J. Lighthill. On sound generated aerodynamically. Part I. General theory. *Proceedings of the Royal Society of London A*, 440:564–587, 1952.
- [10] M. Gennaretti, L. Luceri, and L. Morino. A unified boundary integral methodology for aerodynamics and aeroacoustics of rotors. *Journal of Sound and Vibration*, 200(4):467–489, March 1997.
- [11] Luigi Morino. Is there a difference between aeroacoustics and aerodynamics? an aeroelastician’s viewpoint. *AIAA Journal*, 41(7):1209–1223, July 2003.
- [12] L. Morino, editor. *Computational methods in potential aerodynamics*. Springer-Verlag, 1985.
- [13] F. Farassat and M. K. Myers. Extension of Kirchoff’s formula to radiation from moving surfaces. *Journal of Sound and Vibration*, 123(3):451–460, 1988.

- [14] O. von Estorff, J. P. Coyette, and J. L. Migeot. *Boundary elements in acoustics*, chapter 1. 2002.
- [15] M. K. Myers and J. S. Hausmann. Computation of acoustic scattering from moving rigid surface. *Journal of the Acoustical Society of America*, 91(5):2594–2605, May 1992.
- [16] L. Morino. Boundary integral equations in aerodynamics. *Applied Mechanics Reviews*, 46(8):445–466, 1993.
- [17] P. Zhang, T. W. Wu, and L. Lee. A coupled FEM/BEM formulation for acoustic radiation in a subsonic non-uniform flow. *Journal of Sound and Vibration*, 192(2):333–347, 1996.
- [18] T. W. Wu and L. Lee. A direct boundary integral formulation for acoustic radiation in subsonic uniform flow. *Journal of Sound and Vibration*, 175(1):51–63, August 1994.
- [19] K. Taylor. Acoustic generation by vibrating bodies in homentropic potential flow at low Mach number. *Journal of Sound and Vibration*, 65(1):125–136, 1979.
- [20] R. J. Astley and J. G. Bain. A three-dimensional boundary element scheme for acoustic radiation and scattering. *Journal of Sound and Vibration*, 109(3):445–465, 1986.
- [21] H. Glauert. *The elements of aerofoil and airscrew theory*. Cambridge University Press, 1930.
- [22] J. L. Hess and A. M. O. Smith. Calculation of potential flow about arbitrary bodies. *Progress in Aeronautical Sciences*, 8:1–137, 1967.
- [23] John D. Anderson Jr. *Fundamentals of aerodynamics*. McGraw Hill, 3rd edition, 2001.
- [24] John L. Hess. Review of integral equation techniques for solving potential flow problems with emphasis on the surface-source method. *Computer Methods in Applied Mechanics and Engineering*, 5:145–196, 1975.
- [25] Luigi Morino and Ching-Chiang Kuo. Subsonic potential aerodynamics for complex configurations: A general theory. *AIAA Journal*, 12(2):191–197, February 1974.
- [26] Brian Maskew. Prediction of subsonic aerodynamic characteristics: A case for low-order panel methods. *Journal of Aircraft*, 19(2):157–163, February 1982.
- [27] Milton Van Dyke. Computer extended series. *Annual Review of Fluid Mechanics*, 16:287–309, 1984.
- [28] Milton Van Dyke. Long series in mechanics: Janzen-Rayleigh expansion for a circle. *Meccanica*, 33:517–522, 1998.

- [29] M. J. Lighthill. *Higher Approximations in Aerodynamic Theory*, chapter 3. Princeton University Press, 1960.
- [30] Joseph Katz and Allen Plotkin. *Low-speed Aerodynamics*. McGraw Hill, 1991.
- [31] B. C. Basu and G. J. Hancock. The unsteady motion of a two-dimensional aerofoil in incompressible inviscid flow. *Journal of Fluid Mechanics*, 87:159–178, 1978.
- [32] Luigi Morino and Renzo Piva. *Boundary integral methods, theory and applications*. Springer-Verlag, 1990.
- [33] L. G. Tham and C. K. Chu. Some experiences on programming of time domain boundary element in parallel processing environment. *Journal of Sound and Vibration*, 233(1):1–17, 2000.
- [34] Jesus Alberto Lopez, Fernando Obelleiro, and H. J. Rice. Application of an accelerated generalized minimum residual iteration method in 2D and 3D acoustic scattering problems. Number 3118. AIAA, 2003.
- [35] N. Nishimura. Fast multipole accelerated boundary integral equation methods. *Applied Mechanics Reviews*, 55(4):299–324, July 2002.
- [36] Eric Darrigrand. Coupling of fast multipole method and microlocal discretization for 3-D helmholtz equation. *Journal of Computational Physics*, 181:126–154, 2002.
- [37] Otto von Estorff. Efforts to reduce computation time in numerical acoustics-an overview. *Acta Acustica*, 89:1–13, 2003.
- [38] J. M. Tyler and T. G. Sofrin. Axial flow compressor noise studies. Technical report, Pratt and Whitney Aircraft Div., United Aircraft Corp., 1961.
- [39] Harold Levine and Julian Schwinger. On the radiation of sound from an unflanged circular pipe. *Physical Review*, 1973(4):383–406, February 1948.
- [40] J. W. Posey, M. H. Dunn, and F. Farassat. Quantification of inlet impedance concept and a study of the Rayleigh formula for noise radiation from ducted fan engines. In *4th AIAA/CEAS Aeroacoustics Conference*, June 1998.
- [41] M. H. Dunn. TBIEM3D-A computer program for predicting ducted fan engine noise. Technical Report CR-97-206232, NASA, September 1997.
- [42] M. H. Dunn, J. Tweed, and F. Farassat. The prediction of ducted fan engine noise via a boundary integral equation method. In *2nd AIAA/CEAS Aeroacoustics Conference*. AIAA, May 1996.
- [43] M. A. Hamdi and J. M. Ville. Development of a sound radiation model for a finite-length duct of arbitrary shape. *AIAA Journal*, 20(12):1687–1692, December 1982.



- [44] M. A. Hamdi and J. M. Ville. Sound radiation from ducts: Theory and application. *Journal of Sound and Vibration*, 107(2):231–242, 1986.
- [45] W. S. Hwang. A boundary integral method for acoustic radiation and scattering. *Journal of the Acoustical Society of America*, 101(6):3330–3335, June 1997.
- [46] Edward J. Rice. Multimodal far-field acoustic radiation pattern using mode cutoff ratio. *AIAA Journal*, 16:906–911, April 1978.
- [47] K. S. Wang and T. C. Tszeng. Propagation and radiation of sound in a finite length duct. *Journal of Sound and Vibration*, 93(1):57–79, 1984.
- [48] G. F. Homicz and J. A. Lordi. A note on the radiative directivity patterns of duct acoustic modes. *Journal of Sound and Vibration*, 41(3):283–290, 1975.
- [49] Yusuf Ozyoruk, Vineet Ahuja, and Lyle N. Long. Time domain simulations of radiation from ducted fans with liners. In *7th AIAA/CEAS Aeroacoustics Conference*, May 2001.
- [50] C. J. Chapman. Sound radiation from a cylindrical duct. Part 1. Ray structure of the duct modes and of the external field. *Journal of Fluid Mechanics*, 281:293–311, July 1994.
- [51] S. T. Hocter. Exact and approximate directivity patterns of the sound radiated from a cylindrical duct. *Journal of Sound and Vibration*, 227(2):397–407, April 1999.
- [52] N. Peake. On the radiation properties of an asymmetric cylinder. *Wave Motion*, 22:371–385, 1995.
- [53] G. M. Keith and N. Peake. High-wavenumber acoustic radiation from a thin-walled axisymmetric cylinder. *Journal of Sound and Vibration*, 255(1):129–146, 2002.
- [54] G. M. Keith and N. Peake. High-wavenumber acoustic radiation from a thin-walled scarfed cylinder. *Journal of Sound and Vibration*, 255(1):147–160, 2002.
- [55] T. W. Wu. *Boundary Elements in Acoustics: Fundamentals and Computer Codes*, chapter 3, pages 29–48. WIT, Southampton, 2000.
- [56] Miguel C. Junger and David Feit. *Sound, Structures and their Interaction*. Acoustical Society of America, 1993.
- [57] H. A. Schenck. Improved integral formulation for acoustic radiation problems. *Journal of the Acoustical Society of America*, 44:41–58, 1968.
- [58] A. J. Burton and G. F. Miller. The application of integral equation methods to the numerical solution of some exterior boundary-value problems. *Proceedings of the Royal Society of London. A.*, 323:201–210, 1971.

- [59] T. W. Wu and A. F. Seybert. A weighted residual formulation for the CHIEF method formulation in acoustics. *Journal of the Acoustical Society of America*, 90(3):1608–1614, September 1991.
- [60] D. J. Segalman and D. W. Lobitz. A method to overcome computational difficulties in the exterior acoustics problem. *Journal of the Acoustical Society of America*, 91(4):1855–1861, April 1991.
- [61] R. Martinez. A boundary integral formulation for thin-walled shapes of revolution. *Journal of the Acoustical Society of America*, 87(2):523–532, February 1989.
- [62] Zai You Yan, Kin Chew Hung, and Hui Zheng. Solving the hypersingular boundary integral equation in three-dimensional acoustics using a regularization relationship. *Journal of the Acoustical Society of America*, 113(5):2674–2683, May 2003.
- [63] H. S. Kim, J. S. Kim, and H. J. Kang. Acoustic wave scattering from axisymmetric bodies. *Journal of Sound and Vibration*, 163(3):385–396, January 1992.
- [64] T. W. Wu. On computational aspects of the boundary element method for acoustic radiation and scattering in a perfect waveguide. *Journal of the Acoustical Society of America*, 96(6):3733–3743, December 1994.
- [65] Weiping Wang, Noureddine Atalla, and Jean Nicolas. A boundary integral approach for acoustic radiation of axisymmetric bodies with arbitrary boundary conditions valid for all wave numbers. *Journal of the Acoustical Society of America*, 101(3):1468–1478, March 1997.
- [66] M. S. Howe. *Acoustics of Fluid-Structure Interactions*. Cambridge University Press, 2nd edition, 1998.
- [67] I. E. Garrick and C. E. Watkins. A theoretical study of the effect of forward speed on the free-space sound pressure field around propellers. Technical report, NACA, 1953.
- [68] Banerjee P. K. and Morino L., editors. *Boundary element methods in non-linear fluid dynamics*, volume 6. Elsevier, 1994.
- [69] I.S. Gradshteyn and I.M. Ryzhik. *Table of Integrals, Series, and Products*. 6th edition, July 2000.
- [70] Herbert S. Ribner. Reflection, transmission, and amplification of sound by a moving medium. *Journal of the Acoustical Society of America*, 29(4):435–441, April 1957.
- [71] Douglas M. Nark, F. Farassat, D. Stuart Pope, and V. Vatsa. A model for shear layer effects on engine noise radiation. In *10th AIAA/CEAS Aeroacoustics Conference*, number 2004-2992. AIAA, May 2004.

- [72] F. Farassat and M. H. Dunn. A simple derivation of the acoustic boundary condition in the presence of flow. *Journal of Sound and Vibration*, 224(2):384–386, 1999.
- [73] Forman S. Acton. *Numerical methods that usually work*. The Mathematical Association of America, 4th edition, 1990.
- [74] G. N. Watson. *A treatise on the theory of Bessel functions*. Cambridge University Press, second edition, 1995.
- [75] <http://www.gts.sourceforge.net>. accessed on December 2005.
- [76] R. N. L. Smith. Direct Gauss quadrature formulae for logarithmic singularities on isoparametric elements. *Engineering Analysis with Boundary Elements*, 24:161–167, 2000.
- [77] Allan D. Pierce. *Acoustics: An Introduction to Its Physical Principles and Applications*. Acoustical Society of America, 1989.
- [78] <http://www-unix.mcs.anl.gov/petsc/petsc2/>. accessed on February 2006.
- [79] <http://www.netlib.org/scalapack/>. accessed on February 2006.
- [80] <http://www.cineca.it/pagine/ibmlinuxclust.htm>. accessed on February 2006.

# Appendix A

## Appendix

### A.1 Three dimensional results for wings

Here are displayed the three dimensional results for a NACA2412 and supercritical section wing with and without high lift devices. The figures show the acoustic pressure contours around the lifting body for three different Mach numbers (low, medium and high) and for various frequencies. Also, the angle of attack effect is examined and the high lift devices are added. The contour levels are,  $\pm 10^{-1}$ ,  $\pm 10^{-2}$ ,  $\pm 10^{-3}$ .

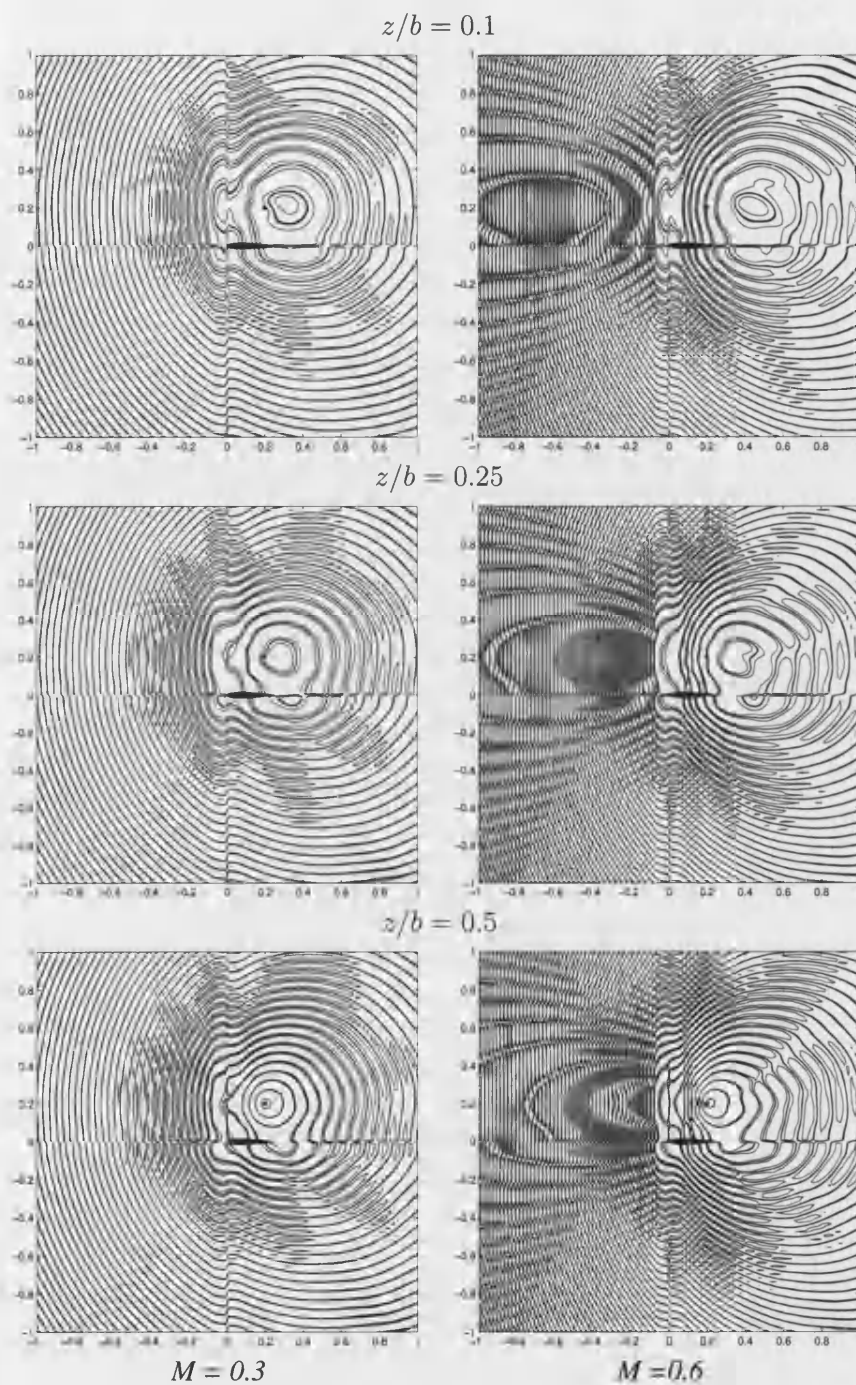


Figure A.1: Total acoustic pressure (real part) around a NACA 2412 wing; positive values shown solid, negative values dashed.  $M = 0.3, 0.6$ ;  $ka = 65$ ;  $z/b = 0.1, 0.25, 0.5$ .

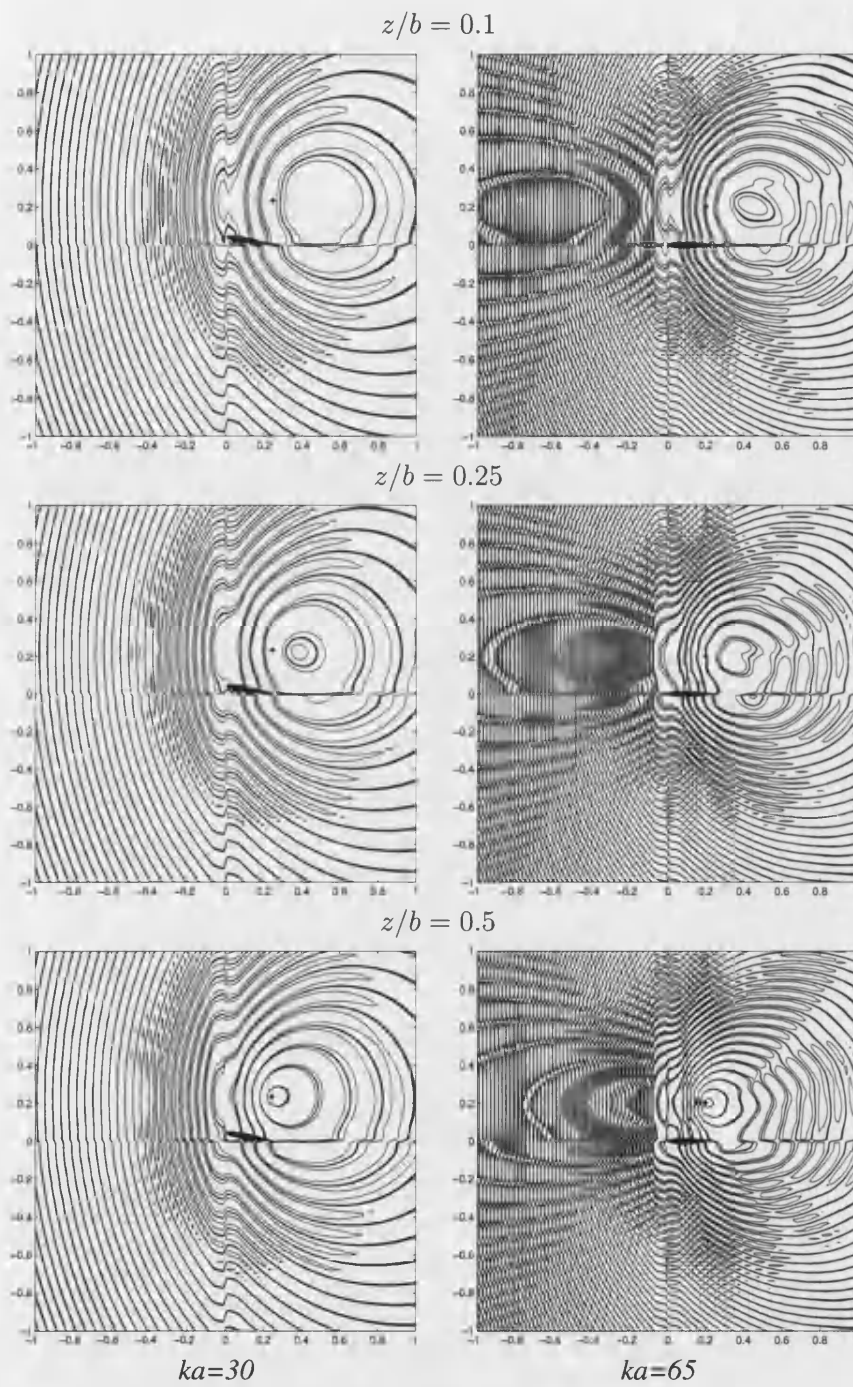


Figure A.2: Total acoustic pressure (real part) around a NACA 2412 wing; positive values shown solid, negative values dashed.  $M = 0.6$ ;  $ka = 30, 65$ ;  $z/b = 0.1, 0.25, 0.5$ ;  $\alpha = 10^\circ$ .

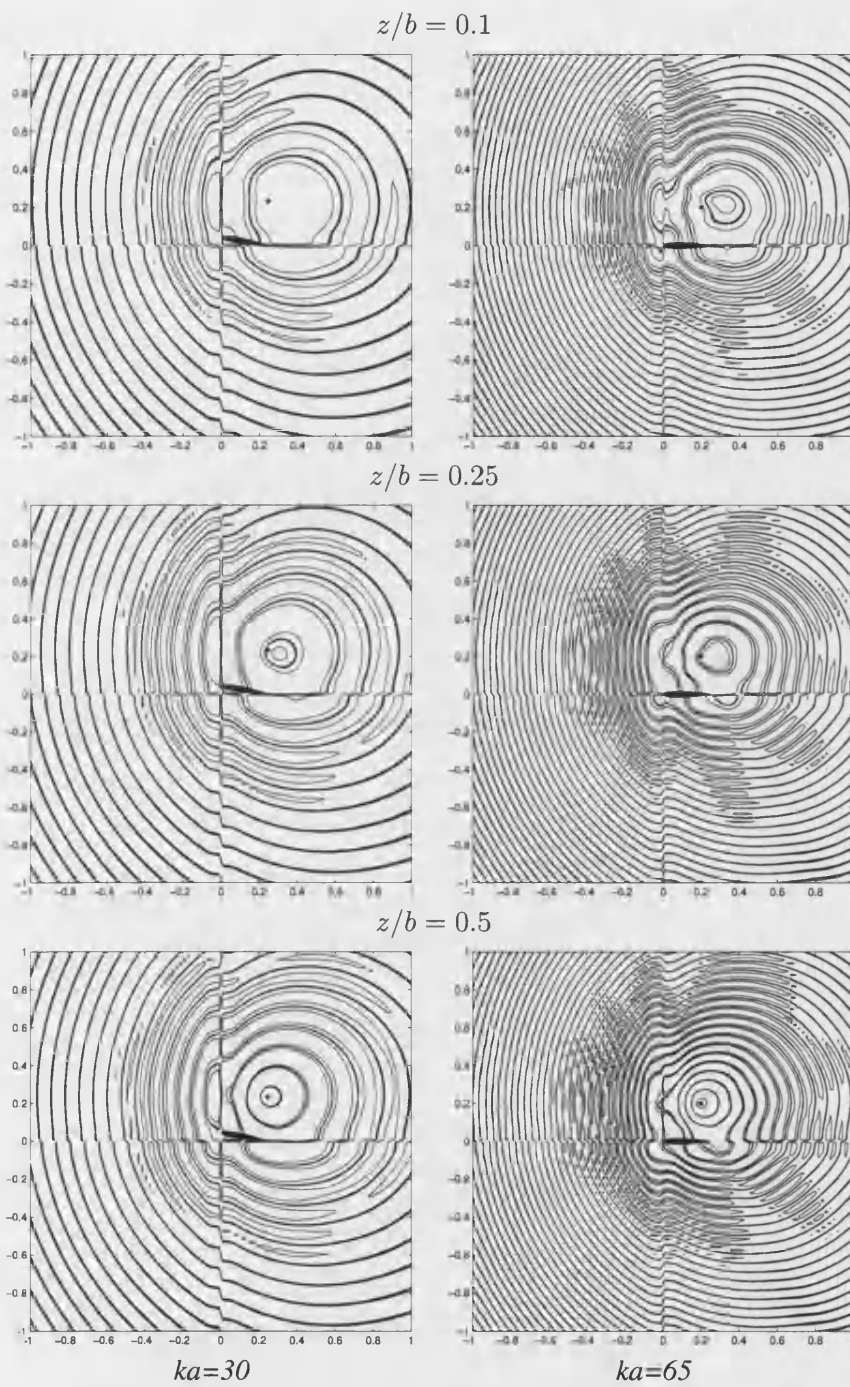


Figure A.3: Total acoustic pressure (real part) around a NACA 2412 wing; positive values shown solid, negative values dashed.  $M = 0.3$ ;  $ka = 30, 65$ ;  $z/b = 0.1, 0.25, 0.5$ ;  $\alpha = 10^\circ$ .

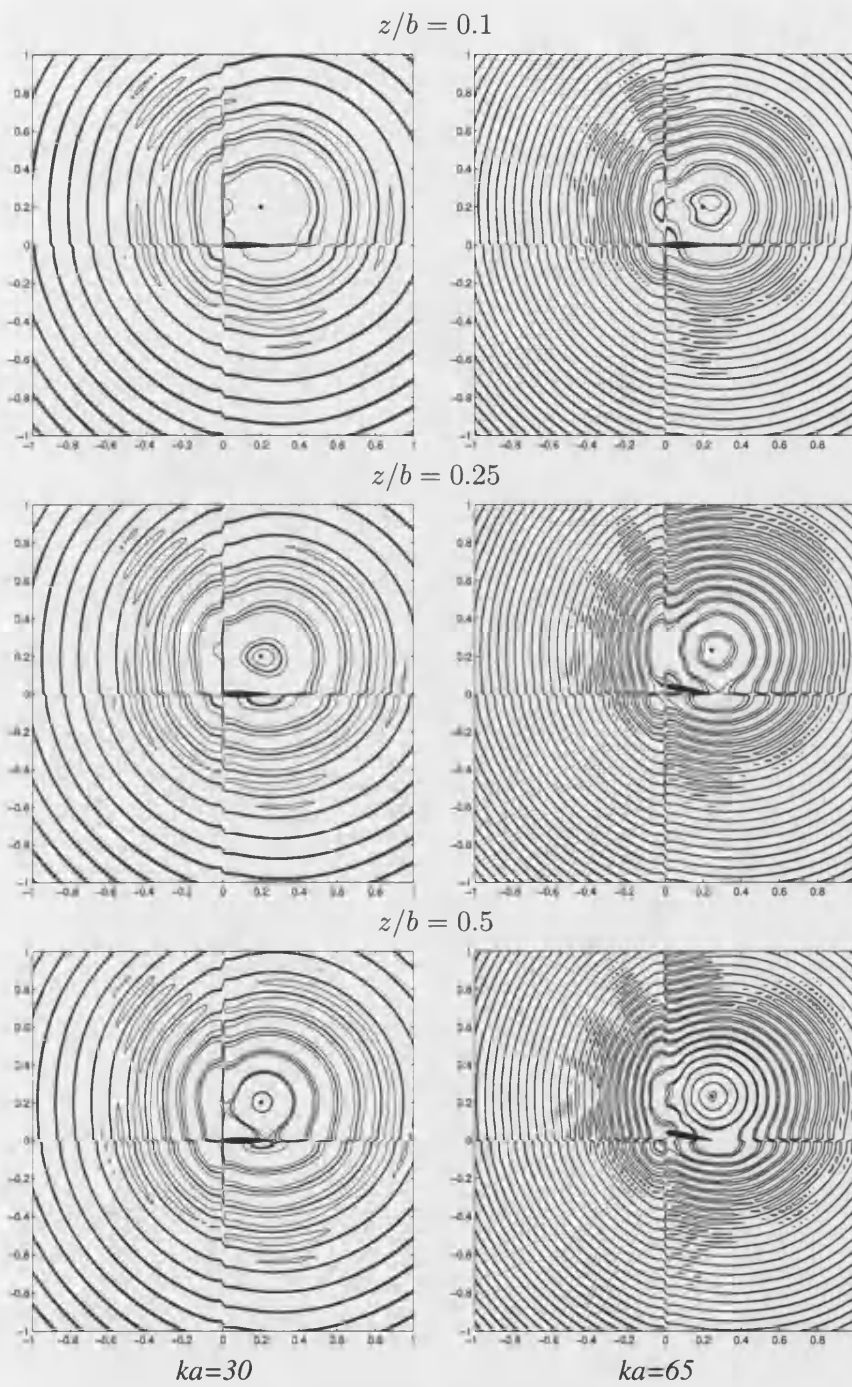


Figure A.4: Total acoustic pressure (real part) around a NACA 2412 wing; positive values shown solid, negative values dashed.  $M = 0.1$ ;  $ka = 30, 65$ ;  $z/b = 0.1, 0.25, 0.5$ ;  $\alpha = 10^\circ$ .



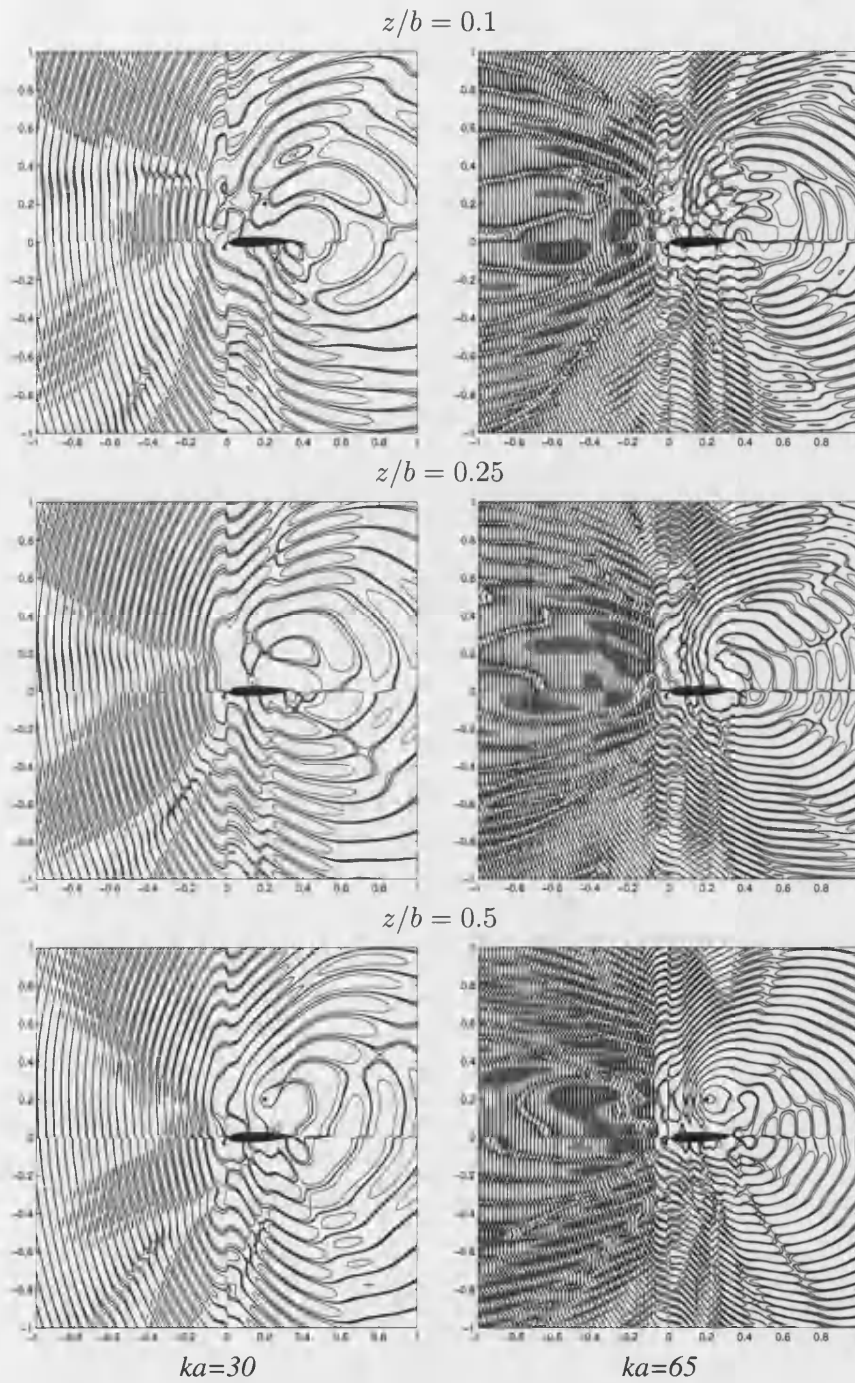


Figure A.5: Total acoustic pressure (real part) around a NACA 2412 wing; positive values shown solid, negative values dashed.  $M = 0.6$ ;  $ka = 30, 65$ ;  $z/b = 0.1, 0.25, 0.5$ .

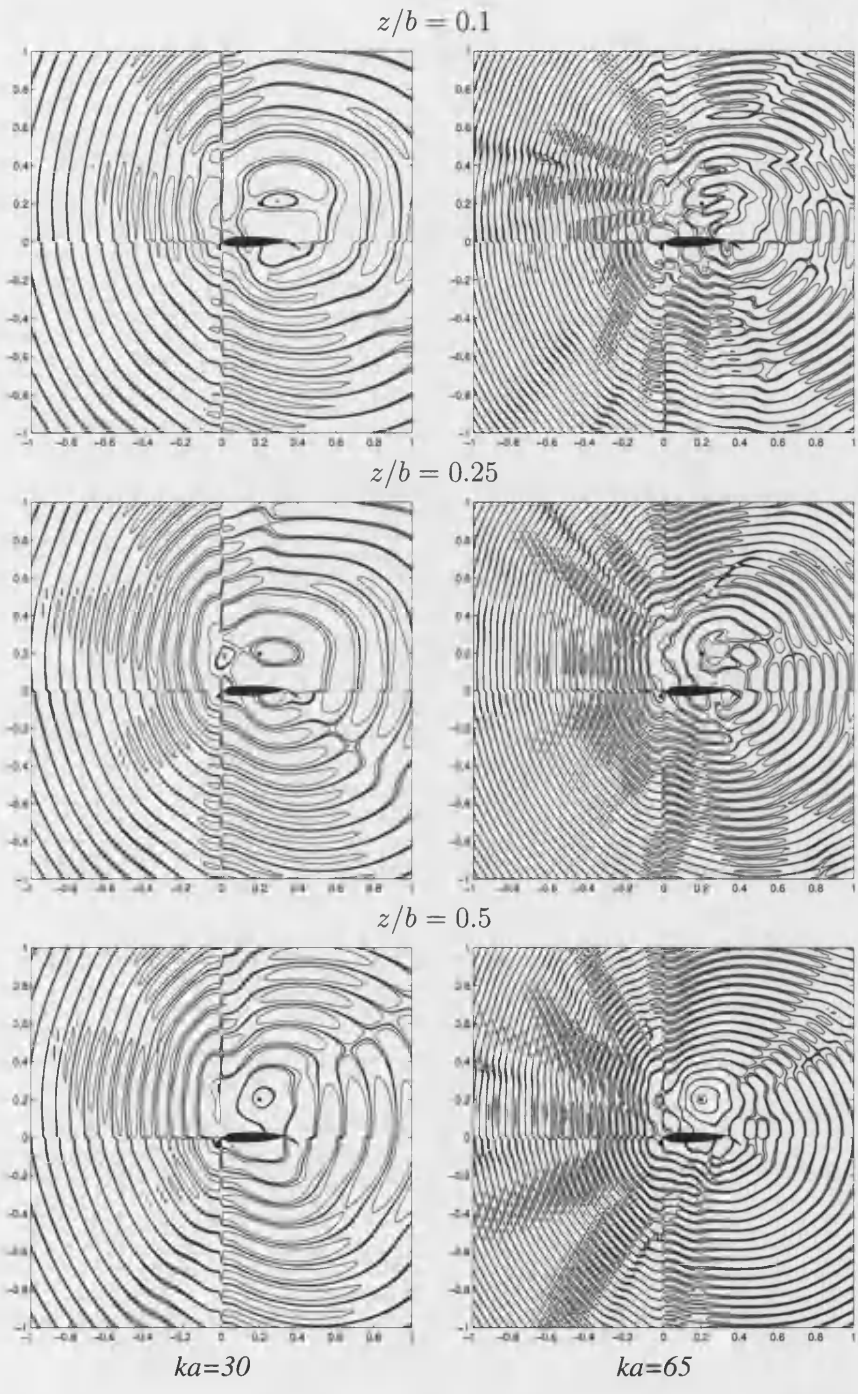


Figure A.6: Total acoustic pressure (real part) around a NACA 2412 wing; positive values shown solid, negative values dashed.  $M = 0.3$ ;  $ka = 30, 65$ ;  $z/b = 0.1, 0.25, 0.5$ .

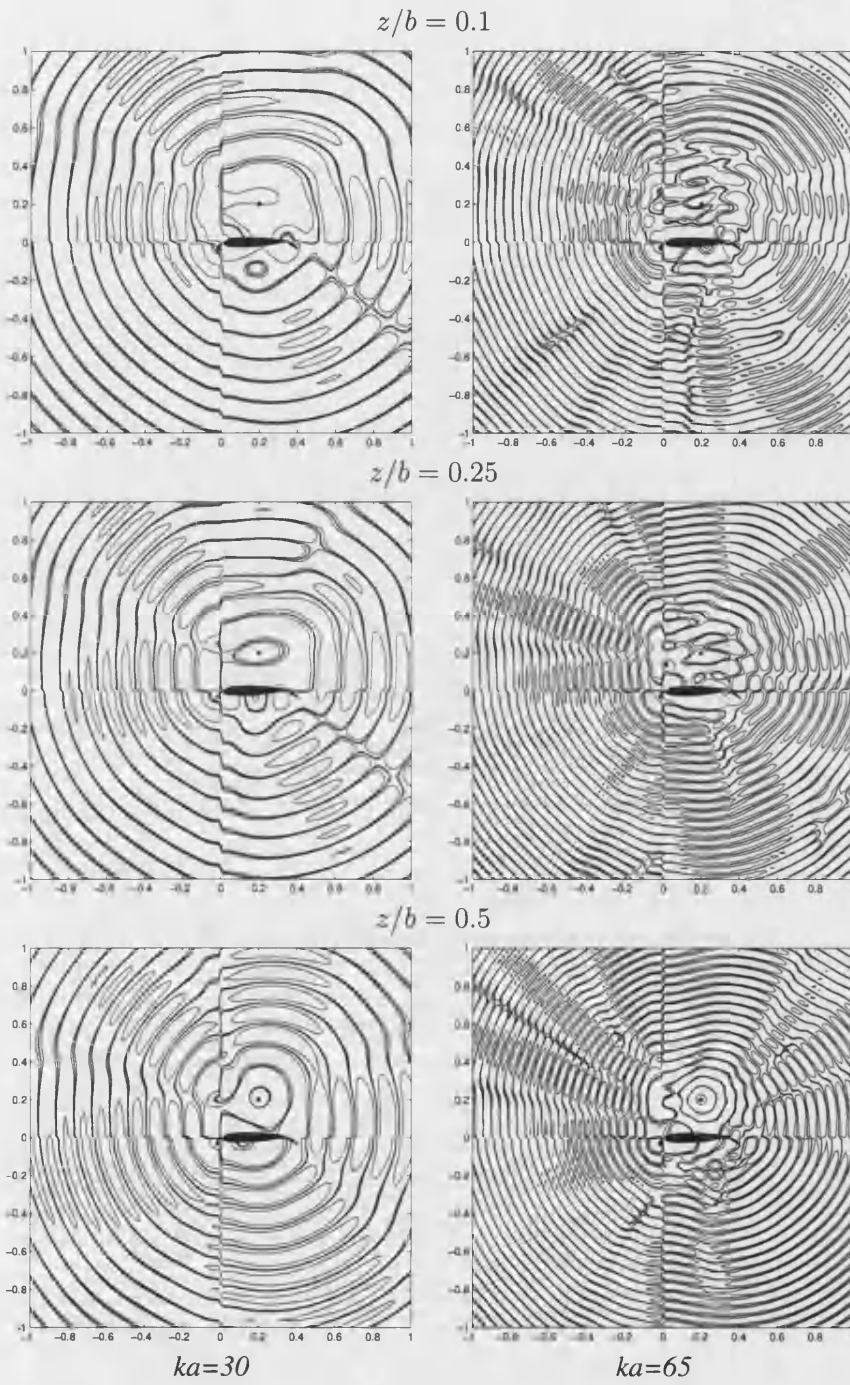


Figure A.7: Total acoustic pressure (real part) around a NACA 2412 wing; positive values shown solid, negative values dashed.  $M = 0.1$ ;  $ka = 30, 65$ ;  $z/b = 0.1, 0.25, 0.5$ .

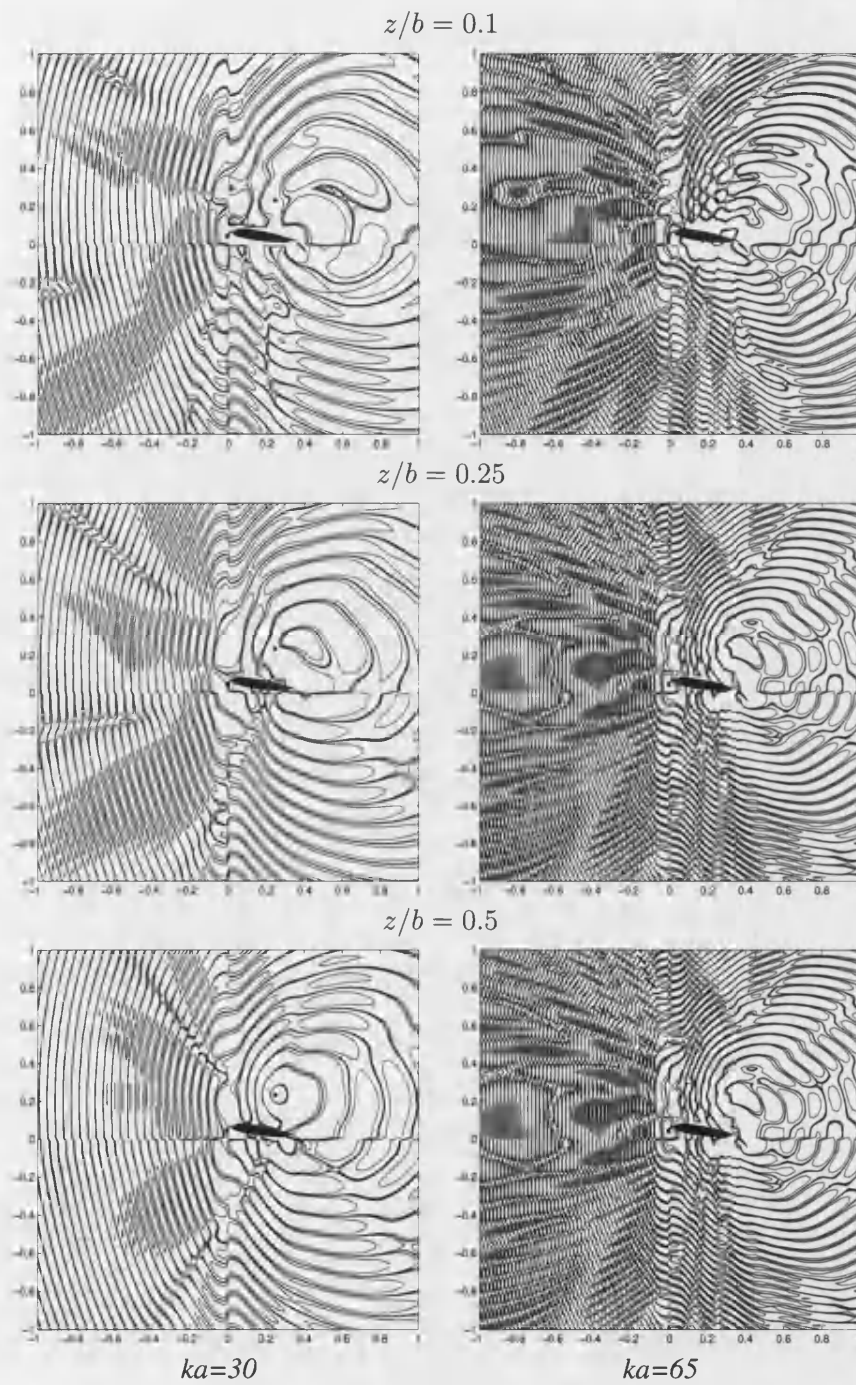


Figure A.8: Total acoustic pressure (real part) around a NACA 2412 wing; positive values shown solid, negative values dashed.  $M = 0.6$ ;  $ka = 30, 65$ ;  $z/b = 0.1, 0.25, 0.5$ ;  $\alpha = 10^\circ$ .

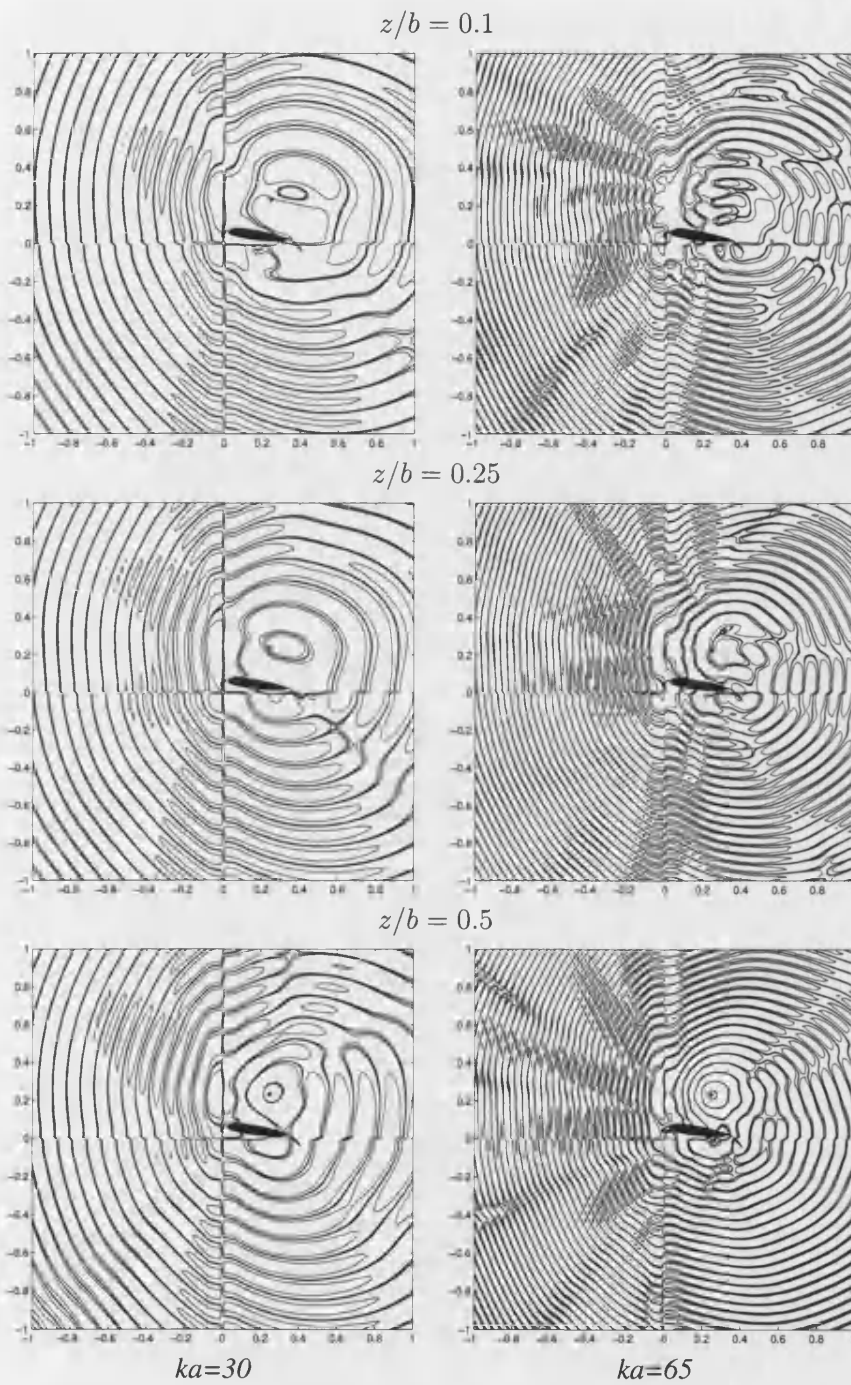


Figure A.9: Total acoustic pressure (real part) around a NACA 2412 wing; positive values shown solid, negative values dashed.  $M = 0.3$ ;  $ka = 30, 65$ ;  $z/b = 0.1, 0.25, 0.5$ ;  $\alpha = 10^\circ$ .



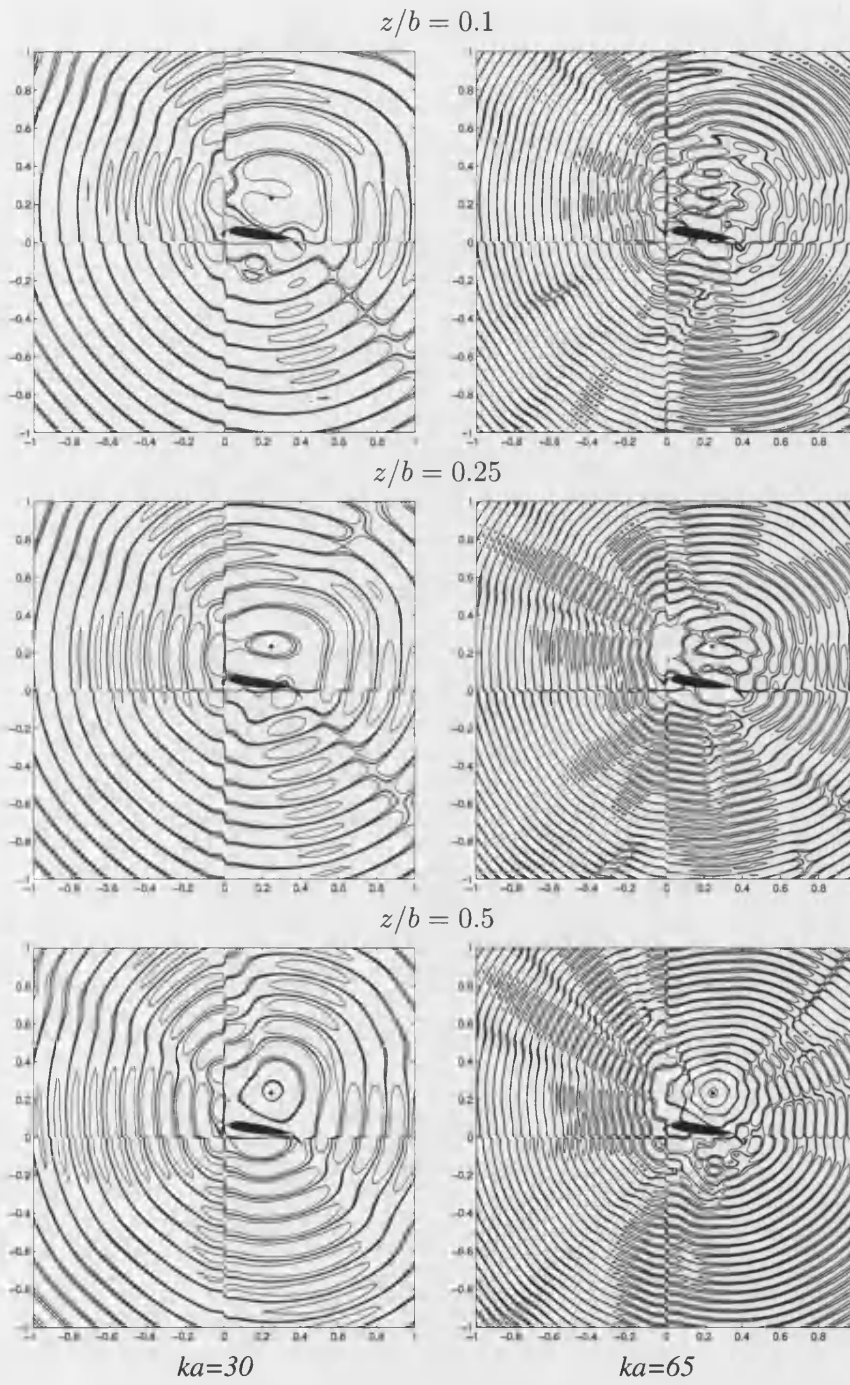


Figure A.10: Total acoustic pressure (real part) around a NACA 2412 wing; positive values shown solid, negative values dashed.  $M = 0.1$ ;  $ka = 30, 65$ ;  $z/b = 0.1, 0.25, 0.5$ ;  $\alpha = 10^\circ$ .

## A.2 Two dimensional results

Here are displayed the two dimensional results for a NACA2412 and supercritical type aerofoil with and without high lift devices. The figures show the acoustic pressure contours around the lifting body for three different Mach numbers (low, medium and high) and for various frequencies. Also, the angle of attack effect is examined and the high lift devices are added. The contour levels are,  $\pm 10^{-1}$ ,  $\pm 10^{-2}$ ,  $\pm 10^{-3}$ .

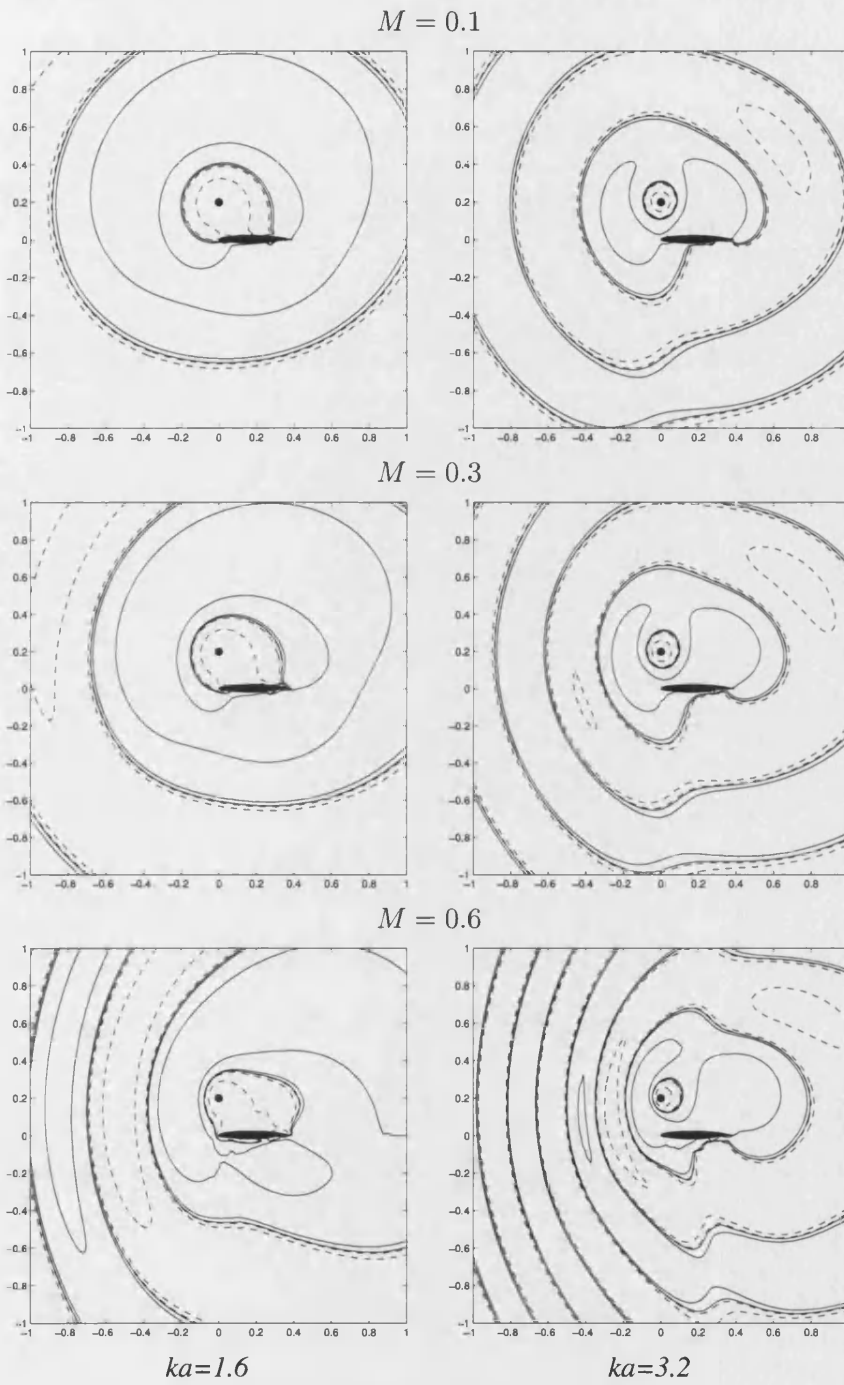


Figure A.11: Total acoustic pressure (real part) around the aerofoil; positive values shown solid, negative values dashed.  $M = 0.1, 0.3, 0.6$ ;  $ka = 1.6, 3.2$ .



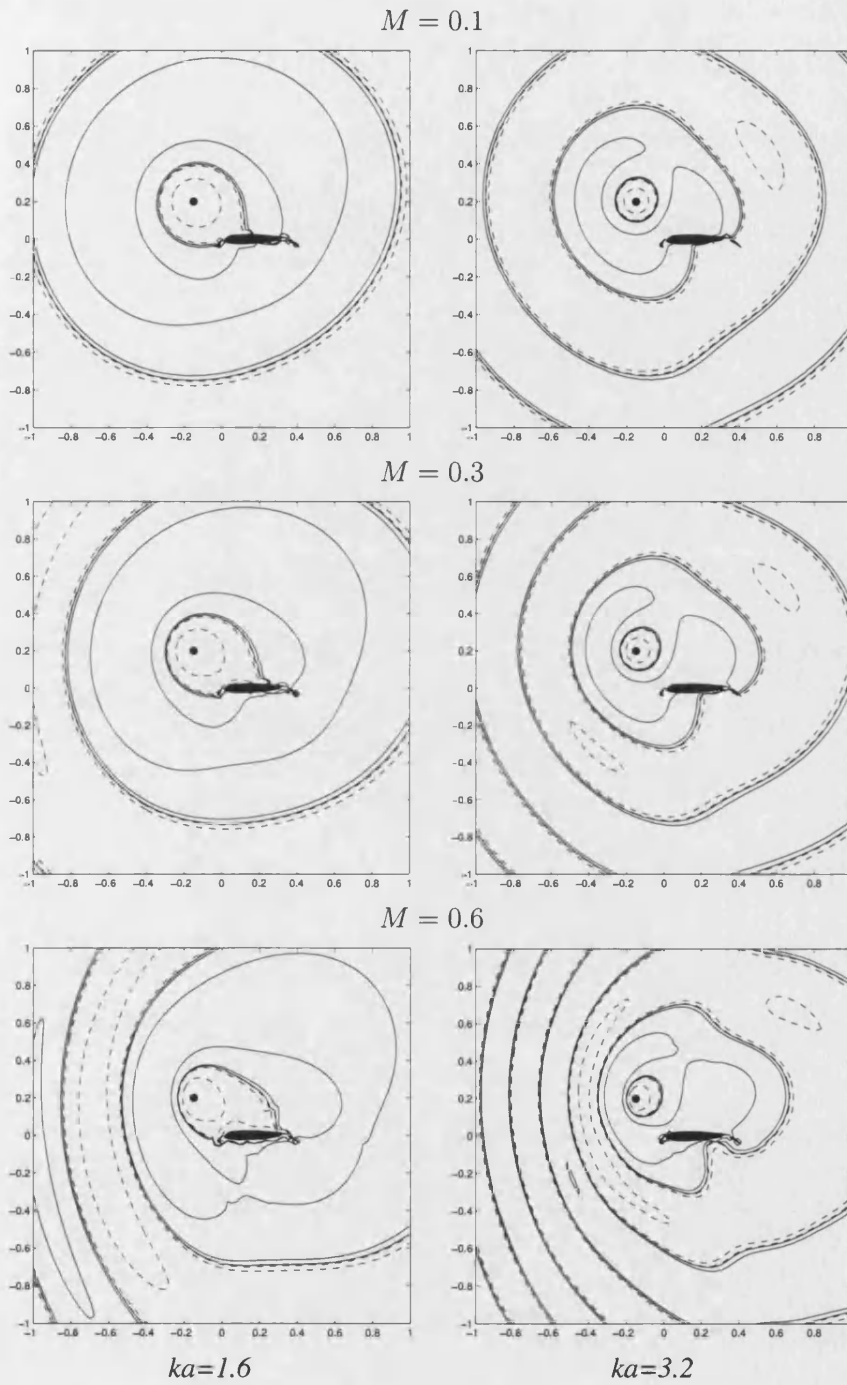


Figure A.12: Total acoustic pressure (real part) around the aerofoil with high lift devices; positive values shown solid, negative values dashed.  $M = 0.1, 0.3, 0.6$ ;  $ka = 1.6, 3.2$ .

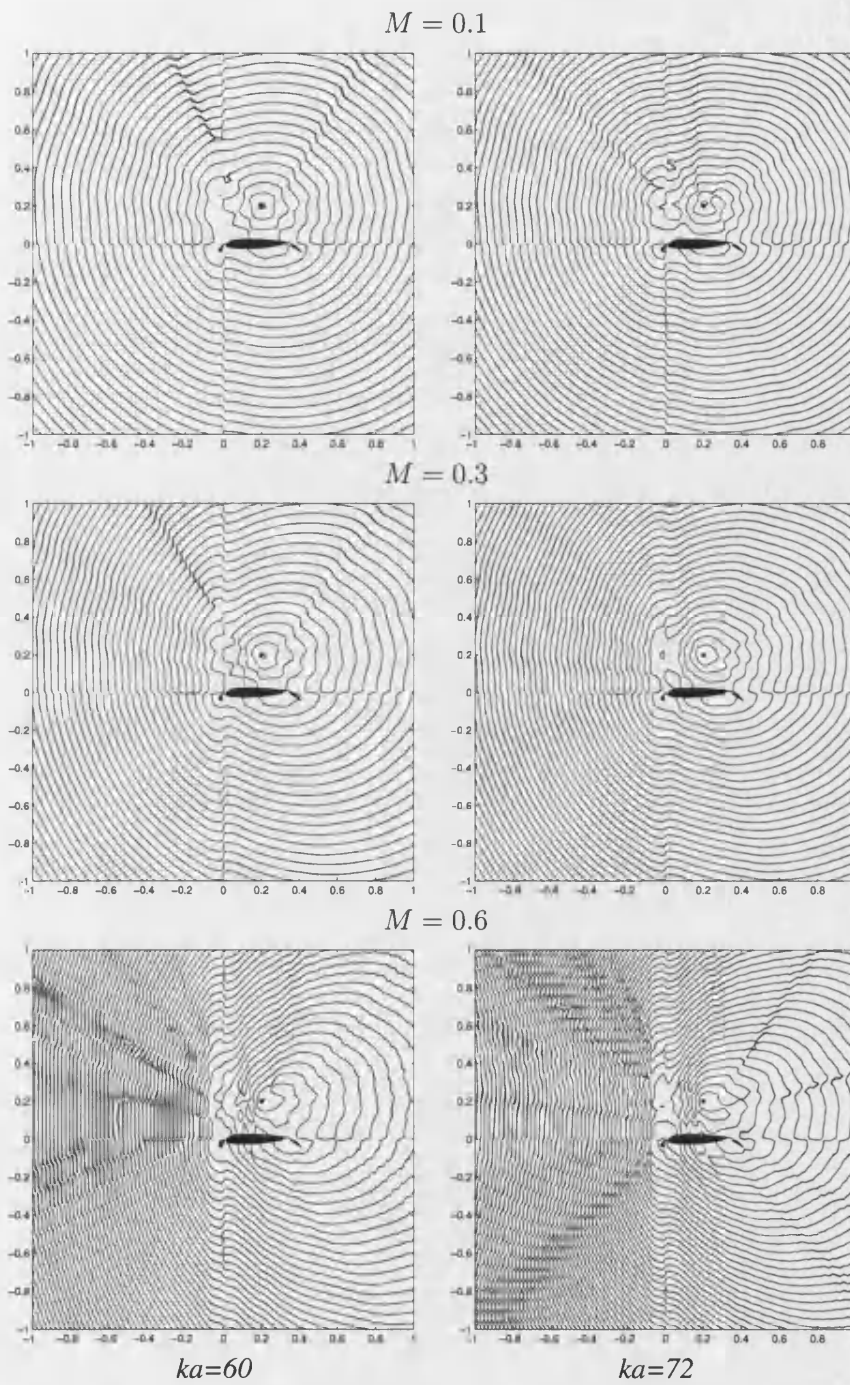


Figure A.13: Total acoustic pressure (real part) around the aerofoil with high lift devices; positive values shown solid, negative values dashed.  $M = 0.1, 0.3, 0.6$ ;  $ka = 60, 72$ .

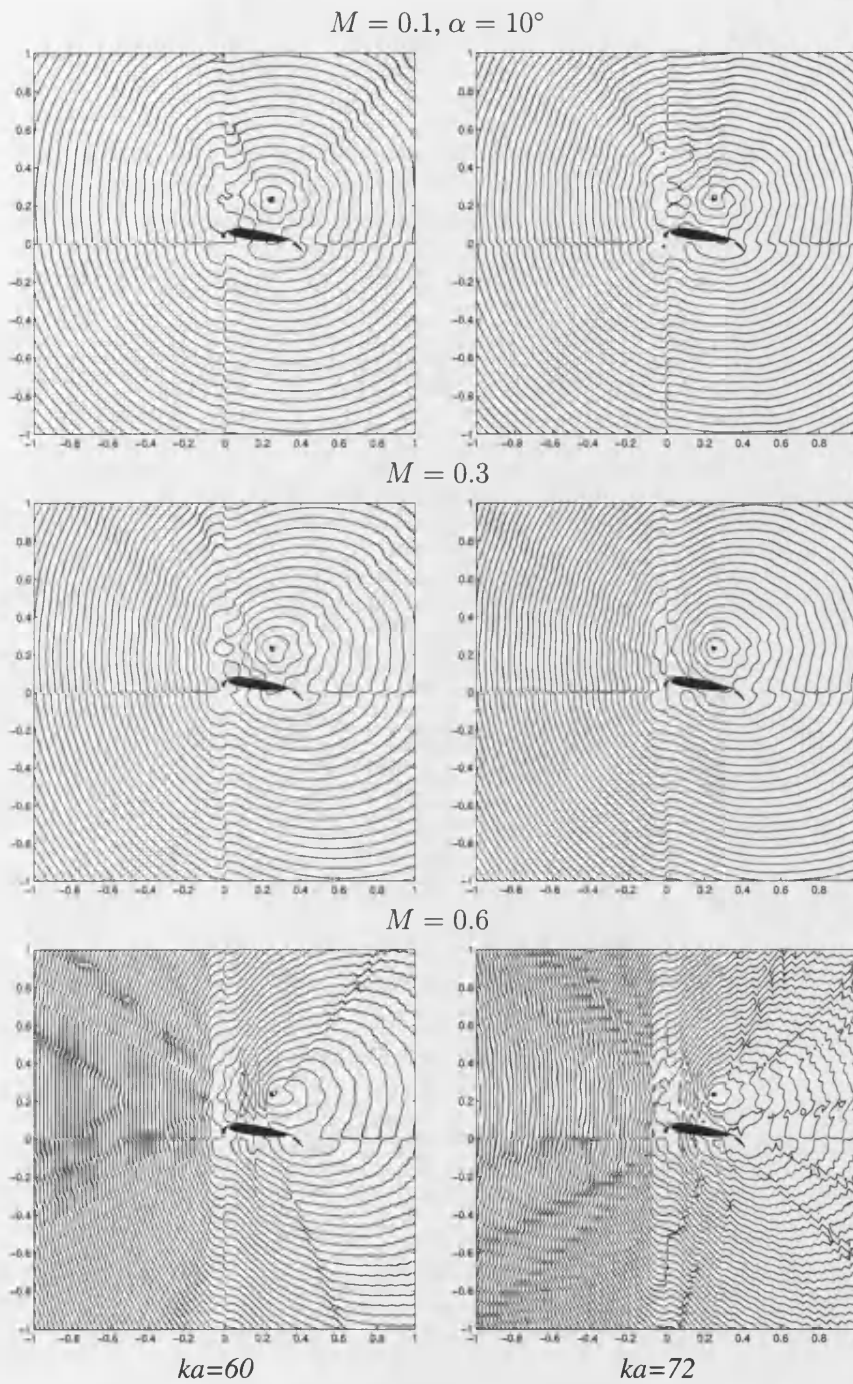


Figure A.14: Total acoustic pressure (real part) around the aerofoil with high lift devices; positive values shown solid, negative values dashed.  $M = 0.1, 0.3, 0.6$ ;  $ka = 60, 72$ ;  $\alpha = 10^\circ$ .